

**AN INVESTIGATION INTO THE ACOUSTIC RESPONSE
OF THE ARTERIES**

By

Essa El-Aklouk

**Thesis submitted in fulfilment of the requirement for the degree of Master of
Philosophy**



**Auckland University of Technology (AUT)
Auckland**

**This thesis contains confidential material. The thesis shall not be given to anyone
who is not directly involved in the examination of the thesis.**

May, 2007

Acknowledgments

I would like to express my true and sincere gratitude to my primary supervisor Prof. Ahmed Al-Jumaily for his invaluable guidance and continued support throughout this research. I would also like to thank my secondary supervisor Dr Andrew Lowe for his continued support, guidance and the fruitful discussions we had. I greatly appreciate the guidance of Dr Khee Hiang Lim and his assistance in proof reading this thesis. I would also like to thank Pulsecor Ltd for supporting this research.

Many thanks go to David, Max, Ashis, Bhupendra, Gijs, Fred, Vivian, Prasika, Alex, and Robert and the whole team at the Biomedical Engineering Centre (BioMEC) for their support, friendship and coping with my frustration at stressful times.

I would also like to thank my best friends Ashraf, Laith, Rami, Mazen, Khaled and Wisam for cheering me up when I was down and giving me the support I needed.

Finally I would like to dedicate this thesis to God and my loving family. Mohmaed, Aida, Ehab, Dia, Raga, Neven, Lana and Mariam. Without them I would not have accomplished anything in life including this thesis. They had faith in my abilities when I had doubts. Special thanks goes to my mum for keeping me well fed and nourished and praying for me.

Abstract

In hypertension, aging and certain types of arterial disease, central elastic arteries become stiffer and hence the central pulse pressure is augmented due to the increase in pulse wave velocity (PWV) and the early return of reflected waves to the heart from the periphery. Valuable information on arterial properties such as stiffness can be obtained from both central (aortic) and peripheral (e.g. radial) pressure waveforms. A feasibility study for the non-invasive estimation of arterial stiffness using pressure waves detected by a pneumatic cuff wrapped around the upper arm is presented. The propagation and reflection of arterial pressure waves (generated by the heart) in the central elastic arteries are simulated using a simplified propagative acoustic model. Furthermore, a lumped parameter model is used to describe the transmission of the pressure waves from the brachial artery to the cuff external wall. By combining the two models, the brachial artery pressure contours under the pneumatic cuff were simulated. Also, the combined model was able to illustrate how these pressures transmit through the arm to the cuff's external wall and produce a strain contour. The effects of aortic stiffness, aortic geometrical variations, heart rate and cuff pressure were investigated by simulating the model at different parameters and observing the pressure and strain augmentation and the timing of the return of the reflected wave. This work was done as part of the development of a non-invasive diagnostic device by Pulsecor Ltd. The model results obtained in this work are in agreement with published experimental results and the strain contours obtained using the device and hence can be used to develop the device's stiffness estimation algorithm.

Table of Contents

Acknowledgments	I
Abstract	II
List of Figures	V
Statement of Originality	VIII
Chapter 1 Introduction	1
<i>1.1 Background</i>	<i>1</i>
1.1.1 Overview of the Cardiovascular System	3
<i>1.2 Literature Review</i>	<i>5</i>
1.2.1 Non invasive stiffness detection methods	5
1.2.2 Cardiovascular Models	9
<i>1.3 Objectives</i>	<i>11</i>
Chapter 2 Theoretical Formulation	13
<i>2.1 Introduction</i>	<i>13</i>
<i>2.2 Acoustic Model</i>	<i>13</i>
<i>2.3 Cuff - Soft Tissue -Brachial Artery Model</i>	<i>21</i>
2.3.1 Cuff and Soft Tissue Model	22
2.3.2 Brachial Artery Model	31
<i>2.4 Closure</i>	<i>34</i>
Chapter 3 Model Development and Simulation	35
<i>3.1 Introduction</i>	<i>35</i>
<i>3.2 Acoustic Model</i>	<i>35</i>
3.2.1 Geometric Consideration	35
3.2.2 Input Wave to the System	38
3.2.3 Wave Reflection Locations	41
3.2.4 Simulation of Acoustic Model	42
<i>3.3 Cuff - Soft Tissue -Brachial Artery Model</i>	<i>43</i>
3.3.1 Lumped Models Parameters	44
<i>3.4 Combined Model</i>	<i>49</i>
<i>3.5 Closure</i>	<i>50</i>

Chapter 4 Simulation Results	51
4.1 Introduction	51
4.2 Simulation and Feature Extraction	51
4.3 Effect of Artery Stiffness Variations	53
4.3.1 Brachial Artery Pressure	54
4.3.2 Cuff Strain	55
4.4 Effect of Artery Radius Variations	56
4.4.1 Brachial Artery Pressure	56
4.4.2 Cuff Strain	58
4.5 Effect of Aortic Thickness Variations	59
4.5.1 Brachial Artery Pressure	59
4.5.2 Cuff Strain	59
4.6 Effect of Heart Rate	61
4.6.1 Brachial Artery Pressure	61
4.6.2 Cuff Strain	62
4.7 Effect of Cuff Pressure	63
4.7.1 Brachial Artery Pressure	64
4.7.2 Cuff Strain	65
4.8 Closure	67
Chapter 5 Discussion and Conclusions	68
5.1 Introduction	68
5.2 Discussion of Results	68
5.2.1 Brachial Artery Contours	68
5.2.2 Effect of Aortic Stiffness Variations	72
5.2.3 Effect of Aortic Radius Variations	74
5.2.4 Effect of Aortic Thickness Variations	76
5.2.5 Effect of Heart Rate	77
5.2.6 Effect of Cuff Pressure	78
5.3 General Discussion	79
5.4 Conclusions	82
5.5 Future Work	84
Appendix A MATLAB Program	85
References	100

List of Figures

Figure 1.1: A schematic of the human heart [8].....	4
Figure 1.2: A schematic of the structure of the major systemic arteries [8].....	4
Figure 1.3: A schematic diagram showing the change in area of the artery with blood pressure.	6
Figure 1.4: Top: central pressure waveform showing wave reflection from the lower body. Bottom: radial artery waveform showing wave reflection from the lower body. [20].....	8
Figure 2.1: Arterial segment free body diagram showing mass and momentum conservation.	15
Figure 2.2: Arterial segment free body diagram showing balancing of forces.....	16
Figure 2.3: A schematic figure showing conditions at a bifurcation.	17
Figure 2.4: A schematic showing reflection from a small side branch.....	21
Figure 2.5: A schematic of the upper arm with a pneumatic cuff wrapped around it.....	22
Figure 2.6: a transverse section of the upper arm with a pneumatic cuff wrapped around it showing pressures and the volumes.....	24
Figure 2.7: A schematic of the brachial artery compressed by a pneumatic cuff. p , v and A are the blood pressure, blood velocity and artery area at different sections of the artery.	31
Figure 3.1: The arteries are divided into elements with different properties.	36
Figure 3.2: Power Function describing the human aorta thickness variation and a linear function describing the thickness variations along the subclavian and brachial arteries.	36
Figure 3.3: Power Function describing the human aorta radius variations and a linear function describing the human subclavian and brachial artery radius variations.	37
Figure 3.4: Pressure wave travelling time vs. number of lumps.....	38
Figure 3.5: Tracings of pressure, flow and ECG during the cardiac cycle of a normal adult. [4].....	39
Figure 3.6: The periodic pressure wave transmitted from the left ventricular to the ascending aorta.....	40

Figure 3.7: One supra-diastolic pressure pulse divided into 38 equally spaced intervals (N).	40
Figure 3.8: A schematic diagram showing the propagation and reflection of pressure waves in the system.....	42
Figure 3.9: Pressure waves determined at the brachial artery: a) Heart wave, b) First reflected wave from the subclavian artery, c) Second reflected wave from the iliac bifurcation, d) Combined wave.....	43
Figure 3.10: Flow chart describing the chain of events in simulating the Cuff-Soft Tissue-Brachial Artery Model.....	47
Figure 4.1: Simulated brachial artery pressure waveform for a healthy young adult. Arrows indicate the four feature points extracted (P1, P2, t1, t2).....	52
Figure 4.2: Simulated strain waveform on the pneumatic cuff outer wall for a healthy young adult. Arrows indicate the four feature points extracted (S1, S2, t1, t2).....	52
Figure 4.3: Brachial artery pressure waveforms at different aortic stiffness values ranging from healthy (75%) to diseased (400%).	54
Figure 4.4: Strain on the pneumatic cuff outer wall contours at different aortic stiffness values ranging from healthy (75%) to diseased (400%).	55
Figure 4.5: Brachial artery pressure waveforms at different aortic radius values ranging from normal (100%) to elevated (200%).	57
Figure 4.6: Strain on the pneumatic cuff outer wall contours at different aortic radii ranging from healthy (75%) to diseased (200%).	58
Figure 4.7: Brachial artery pressure waveforms at different aortic thicknesses ranging from healthy (100%) to diseased (200%).....	59
Figure 4.8: Pneumatic cuff outer wall strain contours at different aortic thicknesses ranging from healthy (100%) to diseased (200%).	60
Figure 4.9: Brachial artery pressure simulation at different heart rates ranging from 75 b/m to 120 b/m.	62
Figure 4.10: Strain contour on the pneumatic cuff outer wall at a number of heart rates ranging from 75 b/m to 120 b/m.	63
Figure 4.11: Brachial artery pressure simulation at a number of cuff pressures ranging from 90 mmHg to 170 mmHg.....	64
Figure 4.12: Strain contours on the pneumatic cuff outer wall at a number of cuff pressures ranging from 90 mmHg to 170 mmHg.	66
Figure 5.1: Brachial artery pressure pulse for healthy young subject [48].	69
Figure 5.2: Pressure and strain contours simulated by the model for normal healthy adult input parameters.	69
Figure 5.3: The compliance of the brachial artery versus transmural pressure.	70

Figure 5.4: The compliance of the brachial artery versus the transmural pressure (Experimental). [49].....	71
Figure 5.5: Brachial artery cross-sectional area under a pressure cuff versus time for a healthy adult male [50].....	71
Figure 5.6: The effect of variations in aortic stiffness on the brachial Augmentation Index.....	73
Figure 5.7: The effect of variations in aortic stiffness on the time lag of the arrival of the reflected wave in both the pressure and strain contours.	74
Figure 5.8: The effect of aortic radius variations on the brachial pressure and cuff strain augmentation indices.....	75
Figure 5.9: The effect of aortic radius variations on the Time Lag of the reflected wave.	75
Figure 5.10: The effect of variations in aortic thickness on the brachial artery and the cuff strain augmentation indices.	76
Figure 5.11: The effect of variations in aortic thickness on the Time Lag between the upstroke of the incident wave and the arrival of the reflected wave to the brachial artery.	77
Figure 5.12: The effect of heart rate on the brachial artery pressure and cuff strain augmentation indices.....	78
Figure 5.13: The effect of cuff pressure on the brachial artery pressure and the cuff strain augmentation indices.....	79
Figure 5.14: Strain contours obtained from the Pulsecor device for three individuals. The legend shows a speculative artery stiffness state.	80
Figure 5.15: A comparison between experimental and model (PWV) vs. Aortic stiffness and patient's age [3].	81

Statement of Originality

'I hereby declare that this submission is my own work and that, to the best of my knowledge and belief, it contains no material previously published or written by another person nor material which to a substantial extent has been accepted for the qualification of any other degree or diploma of a university or other institution of higher learning, except where due acknowledgment is made'

(Signed)

.....

..... (Date)

Chapter 1 Introduction

1.1 Background

Cardiovascular disease is a major cause of death worldwide. Current statistics show that 42% of deaths in New Zealand are caused by cardiovascular disease [1]. Cardiovascular disease is the number one cause of death and disability in the USA in addition to the majority of the developed world. The total cost of cardiovascular disease in the USA was estimated at \$368 billion USD in 2004 [2].

Atherosclerosis (hardening of the arteries) is the major underlying cause of all deaths resulting from cardiovascular disease [3]. It usually results from the deposition of plaque and collagen inside the artery wall. This sometimes also leads to complete calcification of the artery wall which renders it extremely stiff [3].

Plaques can rupture causing severe arterial stenosis (narrowing) that leads to blood flow obstruction. These ruptures can also lead to the formation of blood clots that quickly obstruct or completely stop blood flow in the affected artery [3, 4]. Complete obstruction of blood flow will quickly lead to the death of the tissue supplied by the artery. This can happen to any bodily organ or limb and can cause sudden death in the case of coronary artery thrombosis which leads to a heart attack [3, 4].

Also, excessive artery enlargements caused by atherosclerosis can lead to aneurysms [3, 5]. An aneurysm is a localized, blood-filled dilation of a blood vessel caused by atherosclerosis or weakening of the vessel wall [3, 5]. These aneurysms usually affect the arteries of the brain and the aorta. Rupture of an aneurysm can happen at any time which may lead to the sudden death of the patient [3, 5].

The rhythmic action of the heart introduces pressure waves into the arterial tree. These waves are partially reflected when they experience a change in the medium of transmission. Liu et al and several other researchers [3, 6] observed that bifurcations give rise to backward travelling reflected waves. Interference between the forward travelling waves and the reflected waves is a major determinant of the pressure

waveform. In general, the speed of these waves is proportional to the stiffness of the arterial wall and any increase in this speed causes reflected waves to return back to the heart sooner while the heart is still contracting. This increases the after load of the heart (the force the heart has to pump blood against) which causes left ventricular hypertrophy and coronary artery disease related mortality [3].

The main problem lies in the fact that atherosclerosis usually goes unnoticed. For 65% of men and 47% of women in the USA, the first sign of atherosclerosis is a heart attack or cardiac death [7]. Atherosclerosis begins early in life and progresses with age. The lack of atherosclerosis diagnosis is caused by the small number of symptoms associated with the disease and the lack of regular monitoring.

Deaths from cardiovascular disease and specifically atherosclerosis can be greatly reduced with proper monitoring and treatment. There has been an increasing emphasis on the need to accurately diagnose arterial stiffness (atherosclerosis) in medical literature. Unfortunately conventional invasive methods to diagnose arterial stiffness are expensive, difficult, and involve great risks on the patient.

There has been an increasing demand for the development of accurate and non-invasive methods to diagnose arterial stiffness in recent years. This stress has resulted in the development of a number of non-invasive methods to assess arterial stiffness. These methods employ different principles and make use of hydraulic and/or elastic theories and can be divided into local methods, regional methods and waveform analysis methods (Discussed in section 1.2.1). All of these currently used methods have inherent limitations and there is definitely scope for improvement.

Pulsecor Ltd, a New Zealand based company is currently developing a Wideband External Pulse (WEP) monitor to diagnose arterial stiffness. This is the first device that intends to make use of the brachial artery pulse to non-invasively detect arterial stiffness. Hence, there is a need to develop a physiologically based mathematical model of the arterial system and the interactions between the blood pressure pneumatic cuff with the upper arm soft tissue and the brachial artery. The central aim of this model is to be able to replicate the brachial artery pressure pulse and describe the transmission of this pressure through the pneumatic cuff as in the WEP monitor. The developed model should be able to predict the effect of arterial stiffness on the shape of the obtained

waveforms and also simulate the effect of a number of other artery and cuff parameters on the waveforms. The results of this model can be used to develop the stiffness detection algorithm of the WEP monitor.

1.1.1 Overview of the Cardiovascular System

The cardiovascular system consists of the heart, vasculature and the cells and plasma that constitute blood. The heart pumps blood through approximately 100,000 km of blood vessels [8]. The cardiovascular system serves a number of functions. In general, it is responsible for:

- Transporting oxygen, water and nutrients to all cells of the body.
- Intracellular communication.
- Moving the cells of the immune system from one location to another.
- Moving hormones to the target cells
- Transporting all bodily waste to the specific organ that expels it from the body.
These include carbon dioxide, metabolic waste etc.

The heart acts as two pumps in series. It pumps deoxygenated blood returning from the veins of the body into the lungs. In the lung, the blood gets oxygenated and passes to the left side of the heart into the left ventricle where it gets pumped to the ascending aorta. The aorta branches into smaller arteries that ultimately feed the capillary beds in the tissue where the oxygen is exchanged for carbon dioxide and nutrients are exchanged with tissue waste. The blood returns through the veins to the right heart where the cycle is repeated. Figure 1.1 shows a schematic of the human heart illustrating its chambers.

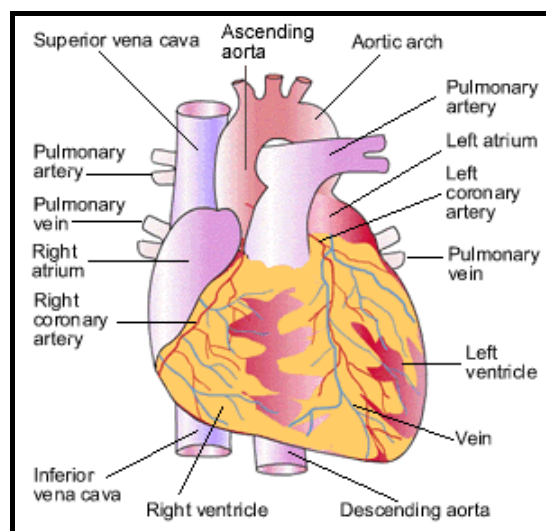


Figure 1.1: A schematic of the human heart [8]

The aorta is divided into four main parts which are the ascending aorta, arch of the aorta, thoracic aorta and abdominal aorta. All the systemic arteries branch from the aorta. Figure 1.2 illustrates the anatomy of all the major systemic arteries.

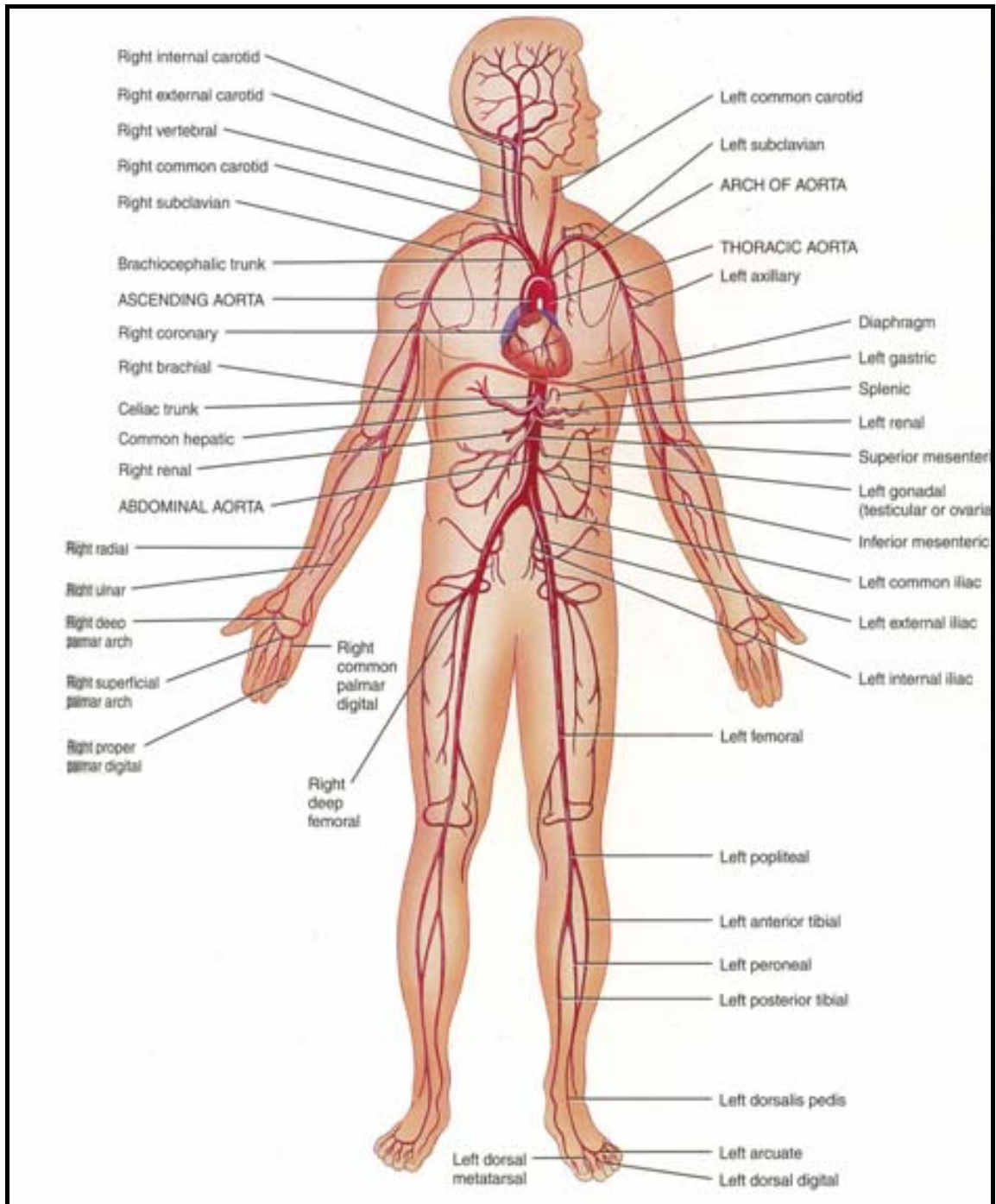


Figure 1.2: A schematic of the structure of the major systemic arteries [8]

1.2 Literature Review

Currently, there are a number of non-invasive methods to detect arterial stiffness. All these methods have inherent limitations and there is definitely a scope for improvement. Also, there have been a number of attempts to build mathematical models for the arterial system in the open literature.

This literature review will focus on two aspects. First a review of the current non-invasive diagnostic methods of detecting stiffness will be given where the advantages and limitations of these methods will be discussed. Secondly, a review of the various arterial and cuff models will be given. This will then be used to provide a justification for the approach this work will take to model the various components.

1.2.1 Non invasive stiffness detection methods

Non-invasive stiffness detection methods can be divided into three main methods. These are local methods that make use of the pressure-area analysis of a specific region of the central or peripheral arteries, regional methods that make use of the pulse wave velocity (PWV) in a segment of the arterial tree and waveform analysis methods that make use of the shape of the pressure pulse at central and peripheral locations.

Local methods are based on the principle that the distension of a region in the arteries to a given pressure is dependent on the stiffness/compliance at this specific location as shown in figure 1.3. The compliance of the artery can be described as [9]:

$$Compliance = \frac{\Delta A}{A.PP} \quad (1.1)$$

where ΔA is the change in the cross-sectional area between the diastolic and systolic pressure, A is the diastolic cross-sectional area and PP is the pulse pressure.

These methods do not require the development of models of the circulation and can be used non-invasively and directly to estimate the arterial stiffness at various sites along the arterial tree. The local arterial stiffness of most of the peripheral arteries can be measured directly by simultaneously measuring artery distension and blood pressure [9]. Ultrasonic devices are usually used to measure the diameter of the artery while

applanation tonometry is used to measure the local blood pressure. Recently, researchers were also able to measure the stiffness of central arteries such as the aorta using magnetic resonance imaging (MRI) [10].

The main advantage of this technique is that it does not require the development of circulatory models and that the local stiffness is directly measured. However, this method requires high levels of expertise and is expensive and time consuming to perform. Furthermore, the technique is limited to the accuracy of the arterial diameter measurement as a video or image analysis system is usually used. Also, the local blood pressure at the central arteries can not be measured directly and usually is obtained by calibrating the brachial to radial waveforms or by using an automatic transfer function that predicts the central pressure waveform from applanation tonometry measurements at the radial artery [6]. This is not very accurate and introduces a further limitation to this method [11].

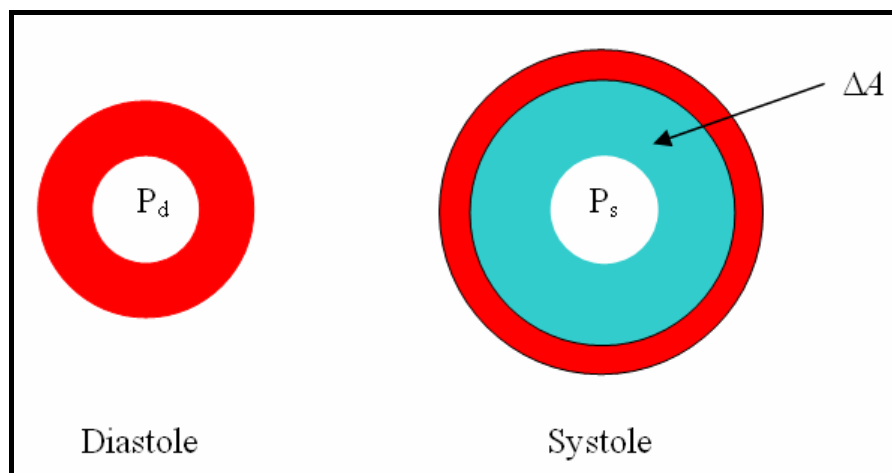


Figure 1.3: A schematic diagram showing the change in area of the artery with blood pressure.

Regional methods for arterial stiffness estimation are based on the principle that pulse wave velocity (PWV) is directly dependent on the stiffness of the artery where the wave is propagating. PWV based methods are simple, non-invasive, cheap and reasonably accurate in determining arterial stiffness [10]. The regional stiffness of the aorta is usually of major interest for a number of reasons. Firstly, the aorta is the biggest contributor to the arterial buffering function [12, 13]; also, aortic PWV is an independent predictor of cardiovascular disease in a number of populations as it has the largest effect on the left ventricular function [14, 15].

The aortic PWV is usually determined by measuring pressure, artery destination or Doppler waveforms at the carotid artery and the femoral artery. The distance travelled by the waves is usually estimated by measuring the body surface distance between the two measuring sites. The PWV can be estimated as:

$$PWV = \frac{\text{Distance}}{\text{Time Lag}} \quad (1.2)$$

The foot to foot method is commonly used to estimate the transient time which is defined as the time it takes the foot (end of diastole) of the wave to travel over a defined distance. Even though the PWV technique is based on an accepted propagative model of the arterial system, there are inaccuracies introduced by the difficulty in estimating the actual distance travelled by the wave and the difficulty in accurately locating the wave's foot [16]. Furthermore, the femoral artery pressure wave can be difficult to accurately measure in individuals suffering from obesity, diabetes and femoral artery disease [16].

Waveform analysis methods are based on the fact that arterial pressure waveforms are a composite of forward travelling waves produced by the contraction of the left ventricle and backward travelling reflected waves from peripheral sites of impedance mismatch [17, 18]. The timing of the arrival of the reflected wave to the ascending aorta depends on both the reflection site and the PWV. In elastic arteries, PWV is relatively low and hence the reflected wave arrives to the ascending aorta during diastole [17, 18]. As the stiffness of the central arteries increase, the PWV increases and reflected waves arrive to the ascending aorta earlier, where it augments and adds to the systolic pressure [17, 18]. This phenomenon is used as an indicator of arterial stiffness where the Augmentation Index (AI) is used to quantify its magnitude as shown in figure 1.4. In the central arteries, the AI is defined as [17, 18, and 19]:

$$AI = \frac{P_s - P_i}{P_s - P_d} \quad (1.3)$$

where P_i is the pressure at the inflection point corresponding to the arrival of the reflected wave, P_s is the systolic pressure and P_d is the diastolic pressure.

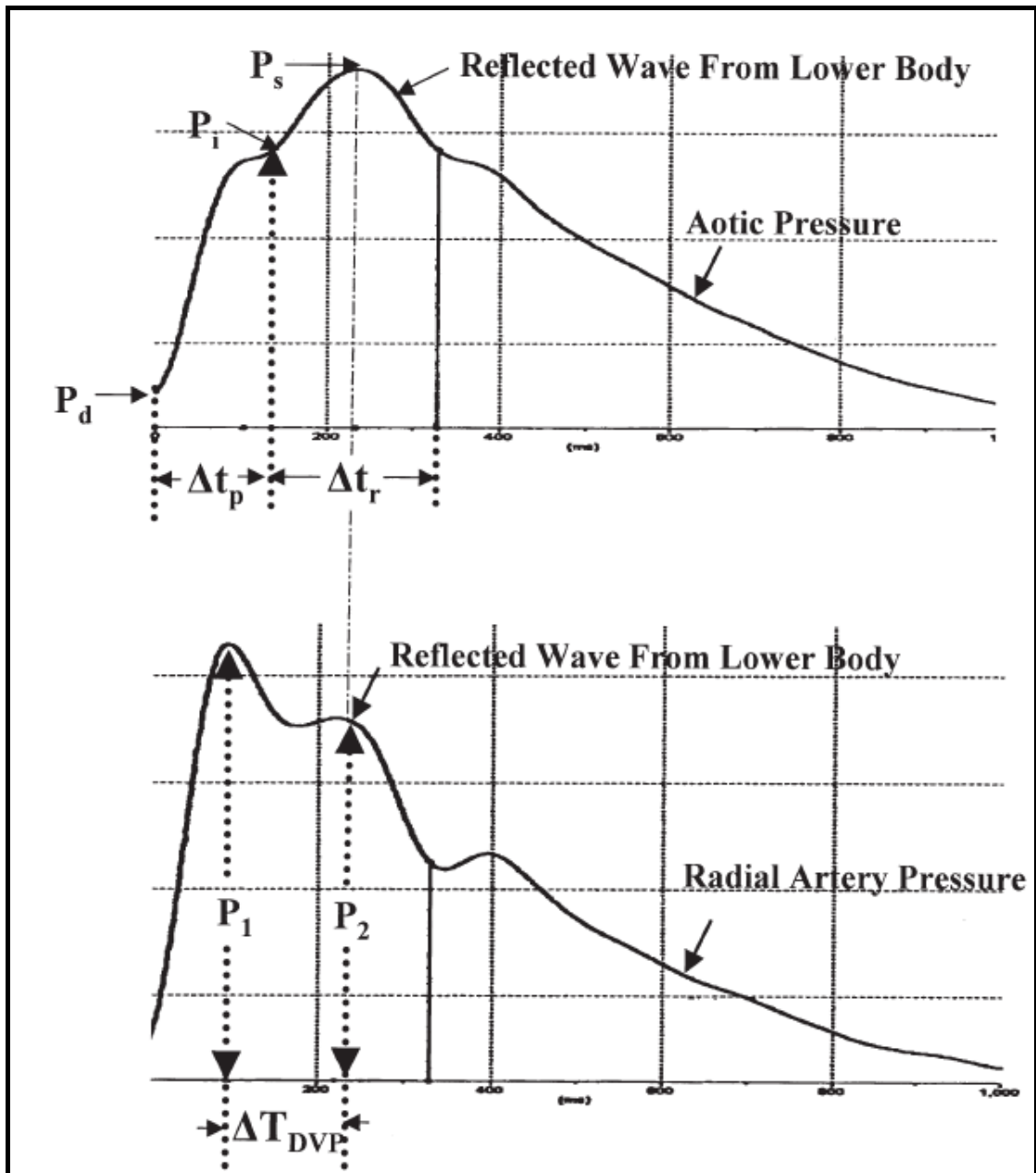


Figure 1.4: Top: central pressure waveform showing wave reflection from the lower body. Bottom: radial artery waveform showing wave reflection from the lower body. [20]

The ascending aorta pressure waves reveal the real load that the left ventricle has to pump against therefore the ascending aorta pressure waveforms should be analysed. Direct non-invasive measurement of ascending aortic pressure is impossible. Hence ascending aortic pressure is either estimated using the common carotid pressure waveform or a transfer function is used to estimate the aortic pressure from the radial artery pressure [21, 22]. These pressures are usually obtained using applanation tonometry. The transfer functions used to estimate aortic waveforms can be either individualised or general [21, 22]. The accuracy of these transfer functions has been the topic of much debate lately and its application, especially at high frequencies, is largely

disputed [22]. Even though the common carotid artery tonometry does not require the use of a transfer function, it requires a high degree of technical expertise and can not be applied in obese patients and patients with an advanced degree of atherosclerosis.

Recently, pressure augmentation in the radial artery and finger waveforms has been identified as an indicator of arterial stiffness [20, 23, and 24]. As the stiffness of the elastic arteries increase, PWV increases and the reflected waves from the lower body arrive at the radial artery and the finger faster which increases the pressure augmentation [20, 24]. A different method is used to calculate the radial artery and the finger AI. This is due to the fact that the site of measurement is further away from the reflection site and the reflected wave usually comes in diastole as shown in figure 1.4. The radial AI is defined as [20]:

$$AI_r = \frac{P_2}{P_1} \quad (1.4)$$

This index has been shown to be related to arterial stiffness and is easily obtainable [20].

1.2.2 Cardiovascular Models

Numerous attempts have been made to mathematically model the human arterial tree including lumped [25-27], one-dimensional [25, 28-30] and multidimensional models [31]. Lumped models and one-dimensional models are frequently used to simulate pressure wave propagations in the arteries and they do provide a good understanding of wave behaviour at reasonable computational costs.

Multi-dimensional models are able to simulate the complete system and are mainly used to give a better insight into the complex flow patterns that are noticed in the blood vessels [31]. However, they result in complex equations which require relatively high computational costs and are unnecessary to study pressure wave propagation in the system.

Lumped models are often used to describe blood pressure and blood flow in the arterial system [25-27]. The lumped models are based on an electrical circuit analogy where

voltage represents blood pressure, current represents flow, resistance represents arterial resistance, capacitors represent the compliance of the vessels and inductors represent the inertia of the blood [25-27]. The Windkessel model is based on the analogy of a fire-hose system. This analogy resulted in the development of the electrical version of the Windkessel model. The Windkessel model is widely used to model blood flow and blood pressure waveforms in the arterial system. It has the advantage of being easy to solve as it results in simple ordinary differential equations.

However, the Windkessel model has some limitation, firstly it is not clear how to estimate the model parameters such as the resistances and other elements from measured blood pressure and blood flow [27]. Furthermore, the model assumes that the system is made of separate conduits and cushioning functions which is not the case as the major arteries have both features. The model also assumes that the PWV is infinite throughout the system. This is clearly not true as PWV is finite and has been measured to be different in different parts of the arterial system [3]. For these reasons, the Windkessel model is only appropriate in modelling the small arterioles [25].

One-dimensional distributed propagative models are more suited to describe pressure and flow in the major arteries [28, 30]. The arterial system can be described as a network of simple distensible tubes where the tubes distributed elastic properties allow for the finite speed propagation of pressure waves [30].

Wave reflections arise from discontinuity in the impedance in the arterial tree. There has been a lot of debate on the origin of wave reflections in the cardiovascular system. Branching points in the major arteries and the high resistance arterioles have been considered to be the major sites of reflection in the cardiovascular system [3, 32-35]. However, substantial evidence suggests that the iliac bifurcation (or aortic bifurcation) is the main source of wave reflection [33-35].

Even in other studies where the high resistance arterioles are considered to be the major reflection site, the effective reflection site is measured to be in the region of the iliac bifurcation [3]. Hence, in this work, the iliac bifurcation is assumed to be the site of wave reflection from the lower body.

Over the past couple of decades, there have been a number of models developed to describe the mechanics and dynamics of blood pressure, pneumatic cuff, arm soft tissue, and brachial artery hemodynamics. All of these models are mainly one dimensional or lumped. These models were developed to study the oscillometric technique of blood pressure measurement. Mauck et al [36] developed a simple one-dimensional model of the artery-soft tissue-cuff system. A more complete one-dimensional model was then developed by Forster and Turney where the collapse of the brachial artery caused by the occlusive cuff was described in more detail [37].

Drzewiecki et al [38] further improved the accuracy of the models by using a more correct model for the pneumatic cuff and the brachial artery collapse. Finally, Ursino and co-workers developed a more accurate model of the oscillometric technique where they developed separate lumped models for the pneumatic cuff, arm soft tissue, and brachial artery [39-41]. These models are based on the previous works in the field with some improvements in aspects of the physical and the mathematical description [38-40]. The Cuff-Soft Tissue- Brachial Artery model developed in this thesis is based on these models.

This work aims to ultimately develop a method that makes use of the brachial artery pressure waveform to accurately detect arterial stiffness. This method will be accurate, easy to perform, and cheap. Also, unlike other conventional wave analysis methods, this method will be physiologically based and therefore will provide a more quantitative measure of arterial stiffness.

1.3 Objectives

This thesis has the following research objectives:

1. Develop and simulate a physiologically based mathematical model of the human systemic arteries. The model should be able to simulate pressure wave propagation and reflection in the system and adequately reproduce the brachial artery pressure contour.
2. Develop and simulate a Cuff-Soft Tissue- Brachial Artery model that is able to describe the interactions between them and simulate the transmission of brachial

artery pressure waves through the arm soft tissue and pneumatic cuff to allow for the estimation of cuff outer wall strain contours from the brachial artery pressure contours.

3. Combine the arterial and the Cuff-Soft Tissue- Brachial Artery models to obtain a complete model that is able to simulate the effect of applying a pneumatic cuff on a subject's arm on the arterial model and to simulate the strain contour on the cuff outer wall.
4. Investigate the effect of variations in arterial geometry, material properties, heart rate and any other significant parameters on the brachial artery pressure contours and pneumatic cuff strain contours.
5. Assess the feasibility of using the model for the development of the Pulsecor WEP monitor stiffness detection algorithm.

Chapter 2 Theoretical Formulation

2.1 Introduction

This chapter is divided into two sections. The first section deals with the acoustic model where the pressure wave propagation in the large systemic arteries is considered and developed. A number of assumptions were made to produce a practical model for wave propagation in the arteries so that it can be solved analytically. The final equations will relate the pressure wave propagating velocity (c) to arterial geometry and material properties. This section also discusses the wave reflection behaviour as these propagating waves reach a bifurcation or an area of large impedance mismatch. The resulting equations will relate the reflection coefficient (R) and the transmission coefficient (T) to the impedance mismatch resulting from artery bifurcation or an abrupt change in geometry or material properties.

The second section is a lumped parameter mathematical model developed for the brachial artery, upper arm soft tissue, and blood pressure cuff. The three model compartments are then linked together to relate the intravascular brachial artery pressure to the circumferential strain on outer cuff wall.

2.2 Acoustic Model

The large central arteries are principally branching compliant tubes filled with fluid. In this section the general equations governing pressure wave propagation and reflection are developed.

The general form of deriving the governing equations for wave propagation in a compliant tube conveying fluid leads to partial differential equations which have complex mathematical involvement without important physical significance. Therefore a number of assumptions are made and justified to produce a practical model for wave propagation.

In this work, it is assumed that fluid contained in the arteries is homogenous and is non-viscous. This is obviously not true as the blood is both non-homogenous and viscous. However work by Taylor has shown that the effects of non-homogeneity and viscosity of blood are only significant in arteries with very small diameters such as arterioles. [42]

In addition, it assumed that the arteries are cylindrical elastic tubes. The artery walls are non-linearly viscoelastic but work by Fung [43] showed that the effect of nonlinear viscoelasticity on wave propagation is not important.

It is also assumed that the length of the tube is long compared with its diameter. This assumption surely holds for the central systemic arteries and is supported by the work of Chang and Atabek [44] which clearly shows that this assumption is justified. From the above assumptions it can be hypothesised that the flow is one dimensional.

Looking at the free body diagram shown in figure 2.1, the basic equations of conservation of mass and momentum can be derived by considering mass conservation in the segment of an artery dx as shown in figure 2.1 (a) which leads to equation 2.1. Balancing the forces acting on the axial direction on a fluid element dx and cross sectional area A as shown in figure 2.1 (b) leads to equation 2.2,

$$\frac{\partial A}{\partial t} + \frac{\partial}{\partial x}(Au) = 0 \quad (2.1)$$

$$\frac{\partial u}{\partial t} + u \frac{\partial u}{\partial x} + \frac{1}{\rho} \frac{\partial p}{\partial x} = 0 \quad (2.2)$$

where A is the area of the artery, u is the velocity of the fluid and ρ is the density of the fluid.

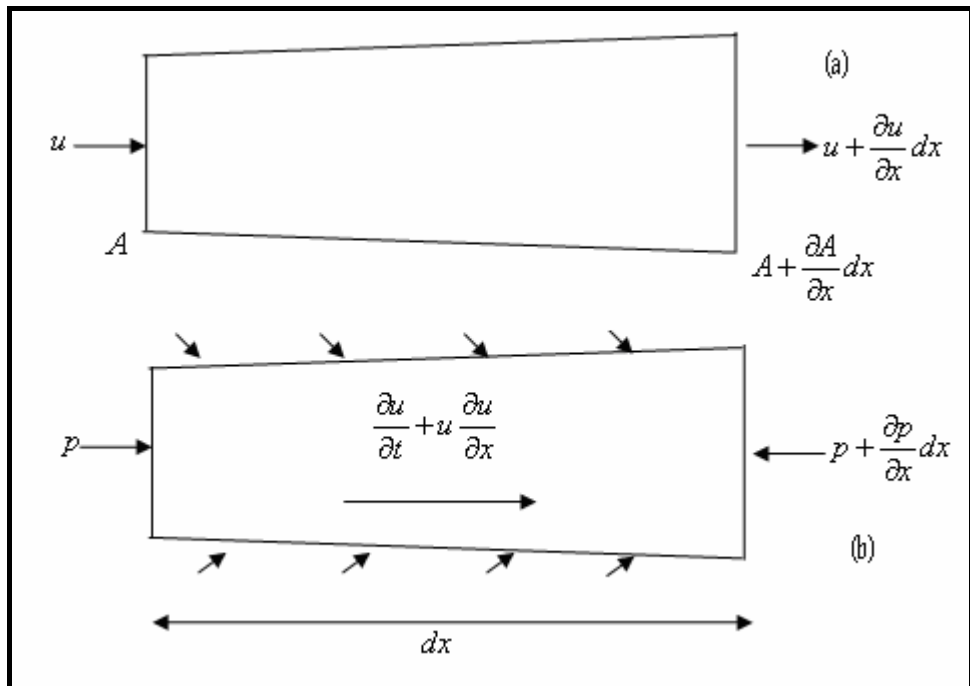


Figure 2.1: Arterial segment free body diagram showing mass and momentum conservation.

It is also assumed that the tube is thin-walled and obeys Hook's law. Hence any small change in transmural pressure dp is balanced by a change the artery's circumferential tension $\frac{Ehdr}{r}$ where E is Young's modulus of elasticity, h is artery wall thickness and r is the artery radius. From equilibrium of the forces acting on a free body shown in figure 2.2 one can write:

$$\frac{Ehdr}{r} = rdp \quad (2.3)$$

Equations 2.1 – 2.3 can now be used to derive an equation governing steady state flow through an elastic artery and with further simplifications the theoretical artery wave speed can be determined.

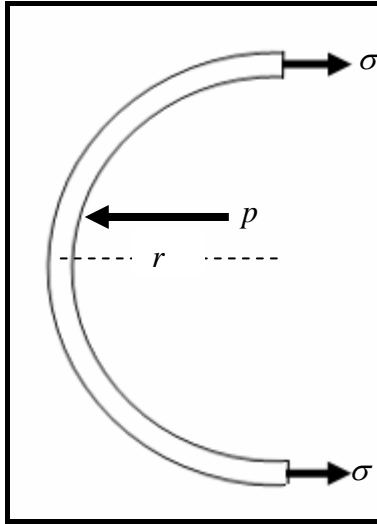


Figure 2.2: Arterial segment free body diagram showing balancing of forces.

Equation 2.1 is linearized by substituting $A = \pi r^2$ and by assuming that the wave amplitude is much smaller than the wave length. Neglecting second order terms reduces the equation to:

$$\frac{\partial u}{\partial x} + \frac{2}{r} \frac{\partial r}{\partial t} = 0 \quad (2.4)$$

Equation 2.2 can also be linearized by taking into account small disturbances in a motionless artery filled with fluid. Hence the $u \frac{du}{dx}$ term is not significant and equation 2.2 can be written as:

$$\frac{\partial u}{\partial t} + \frac{1}{\rho} \frac{\partial p}{\partial x} = 0 \quad (2.5)$$

Combining equations 2.3 and 2.5 results in:

$$\frac{\partial u}{\partial x} + \frac{2r}{Eh} \frac{\partial p}{\partial t} = 0 \quad (2.6)$$

Differentiating equation 2.4 with respect to x and equation 2.6 with respect to t , then neglecting the second order terms and substituting gives:

$$\frac{\partial^2 p}{\partial x^2} - \frac{1}{c^2} \frac{\partial^2 p}{\partial t^2} = 0 \quad (2.7)$$

where

$$c^2 = \frac{Eh}{2\rho r} \quad (2.8)$$

Equation 2.7 is the wave equation where c is the wave speed,

$$c = \sqrt{\frac{Eh}{2\rho r}} \quad (2.9)$$

The solution of equation 2.7 can be written as:

$$P(x,t) = P_0 f(x-ct) + P_0' f(x+ct) \quad (2.10)$$

Where $P_0 f(x-ct)$ represents an incident pressure wave travelling in the positive x direction and $P_0' f(x+ct)$ represents a pressure wave travelling in the negative x direction.

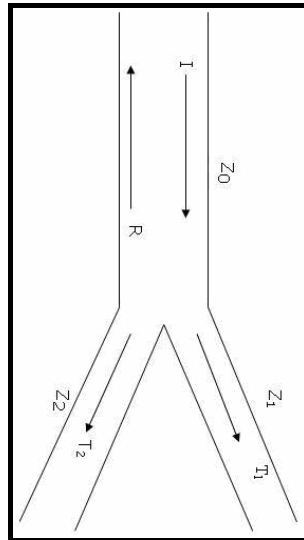


Figure 2.3: A schematic figure showing conditions at a bifurcation.

The above formulation demonstrates that pressure wave speed c through the artery depends on the arterial elasticity, thickness, radius and the density of the blood. This

will be used in Chapter 3 to develop the complete wave propagation model in the central arterial system of interest.

Pressure waves are partially reflected when they experience a sudden change in the medium of transmission such as a bifurcation or a sudden change in the artery's geometry or material properties. Central arteries such as the aorta bifurcate into a number of smaller arteries. Also in some diseases such as aneurysms, discrete batches of the arteries degenerate and cause a large change in material properties and geometry. When a pressure wave arrives at a bifurcation, part of that wave is transmitted while the other part is reflected back.

Consider a tube that branch into two daughter tubes T_1 and T_2 , as shown in figure 2.3. At the junction it is assumed that pressure p is a single valued function which can be written as:

$$p_I + p_R = p_{T_1} = p_{T_2} \quad (2.11)$$

where p_I is the incident pressure wave, p_R is the reflected pressure wave in the parent tube, p_{T_1} is the pressure transmitted into the first daughter tube T_1 , and p_{T_2} is the pressure transmitted into the second daughter tube T_2 . Also, it can be assumed that the flow is continuous:

$$Q_I - Q_R = Q_{T_1} + Q_{T_2} \quad (2.12)$$

where Q_I is the incident flow wave, Q_R is the reflected flow wave, Q_{T_1} is the flow into the first daughter tube T_1 and Q_{T_2} is the flow wave into the second daughter tube T_2 . Equations 2.11-2.12 describe the pressure and flow conditions at the junction. Now a relationship between the pressure and flow is required. The characteristic impedance of the artery is a very important characteristic and is defined by:

$$Z = \frac{pC}{A} \quad (2.13)$$

Z is also defined by the ratio of oscillatory pressure to oscillatory flow when the wave travels in the positive x direction:

$$Z = \frac{P}{Q} \quad (2.14)$$

Using equation 2.14, equation 2.12 can be written as:

$$\frac{p_I - p_R}{Z_0} = \frac{p_{T_1}}{Z_1} + \frac{p_{T_2}}{Z_2} \quad (2.15)$$

Using equations 2.11 and 2.15, the reflection coefficient R can be expressed as:

$$R = \frac{p_R}{p_I} = \frac{Z_0^{-1} - (Z_1^{-1} + Z_2^{-1})}{Z_0^{-1} + (Z_1^{-1} + Z_2^{-1})} \quad (2.16)$$

and the transmission coefficient T can be written as:

$$T = \frac{p_{T_1}}{p_I} = \frac{p_{T_2}}{p_I} = \frac{2Z_0^{-1}}{Z_0^{-1} + (Z_1^{-1} + Z_2^{-1})} \quad (2.17)$$

Using equations 2.16 and 2.17 the amplitude of the reflected pressure wave and the transmitted pressure wave at a junction can be calculated from the knowledge of the impedance of the parent and daughter arteries which is determined by the geometry and material properties of the respective arteries.

In this work it is also important to model the condition where pressure waves travel from a small artery into a larger artery as in reflected waves from any of the aorta's side branches.

Looking at figure 2.4, similar simplifying assumptions can be made as above. The pressure at the junction can be assumed to be a single valued function which can be written as:

$$p_I + p_R = p_T \quad (2.18)$$

where p_T is the pressure transmitted into the large artery. Furthermore, it can be assumed that the flow is continuous, hence:

$$Q_I - Q_R = Q_T \quad (2.19)$$

where Q_T is the flow transmitted into the large artery. Using equation 2.14, equation 2.19 can be written as:

$$\frac{p_I - p_R}{Z_0} = \frac{p_T}{Z_1} \quad (2.20)$$

Using equations 2.18 and 2.20, the reflection coefficient (R) can be expressed as:

$$R = \frac{p_R}{p_I} = \frac{Z_1^{-1} - Z_0^{-1}}{Z_1^{-1} + Z_0^{-1}} \quad (2.21)$$

and the transmission coefficient can be written as:

$$T = \frac{p_T}{p_I} = \frac{2Z_0^{-1}}{Z_0^{-1} + Z_1^{-1}} \quad (2.22)$$

From the above formulation, wave propagation phenomenon in branching arteries can be defined.

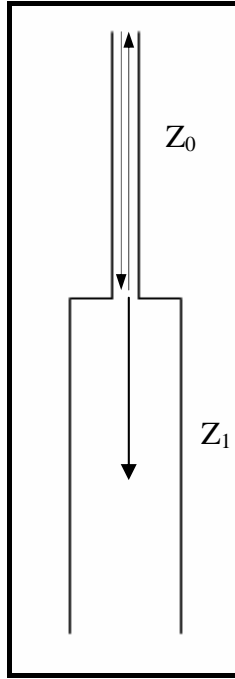


Figure 2.4: A schematic showing reflection from a small side branch.

The propagation speed of pressure waves is determined by the arterial geometry and material properties. The pressure in the parent artery can then be defined as:

$$p = p_I + p_R = p_I(t - x/c_0) + Rp_I(t + x/c_0) \quad (2.23)$$

and in the daughter artery, the pressure can be defined as:

$$p_T = Tp_I(t - x/c_{1,2}) \quad (2.24)$$

where $c_{1,2}$ is the wave speed in the either one of the daughter tubes.

2.3 Cuff - Soft Tissue -Brachial Artery Model

In this section a mathematical model for an upper arm compressed by a pneumatic cuff is developed. A literature review shows that a variety of models have been proposed to study this structure [36-41]. However all of these models were intended to study the oscillometric method of blood pressure measurement whereas the main purpose of this work is to study the interactions between the pneumatic cuff, upper arm soft tissue and brachial artery hemodynamics. The model developed in this work is based on recent work proposed by Ursino et al [39-41]. The model takes into account a number of important aspects overlooked by previous works. In this thesis, separate models will be

developed for the pneumatic cuff, soft tissue, and the brachial artery. Finally these models will be linked together as a complete representation of the interactions between the three structures so that the brachial artery pressure can be estimated non-invasively from the circumferential strain on the cuff's outer wall.

In this work, the upper arm is modelled as a cylinder of elastic homogenous tissue with a pneumatic cuff wrapped around it. The bone is modelled as a rigid cylinder embedded in the centre of the cylinder. Also the brachial artery is assumed to be embedded within the arm soft tissue as shown in figure 2.5.

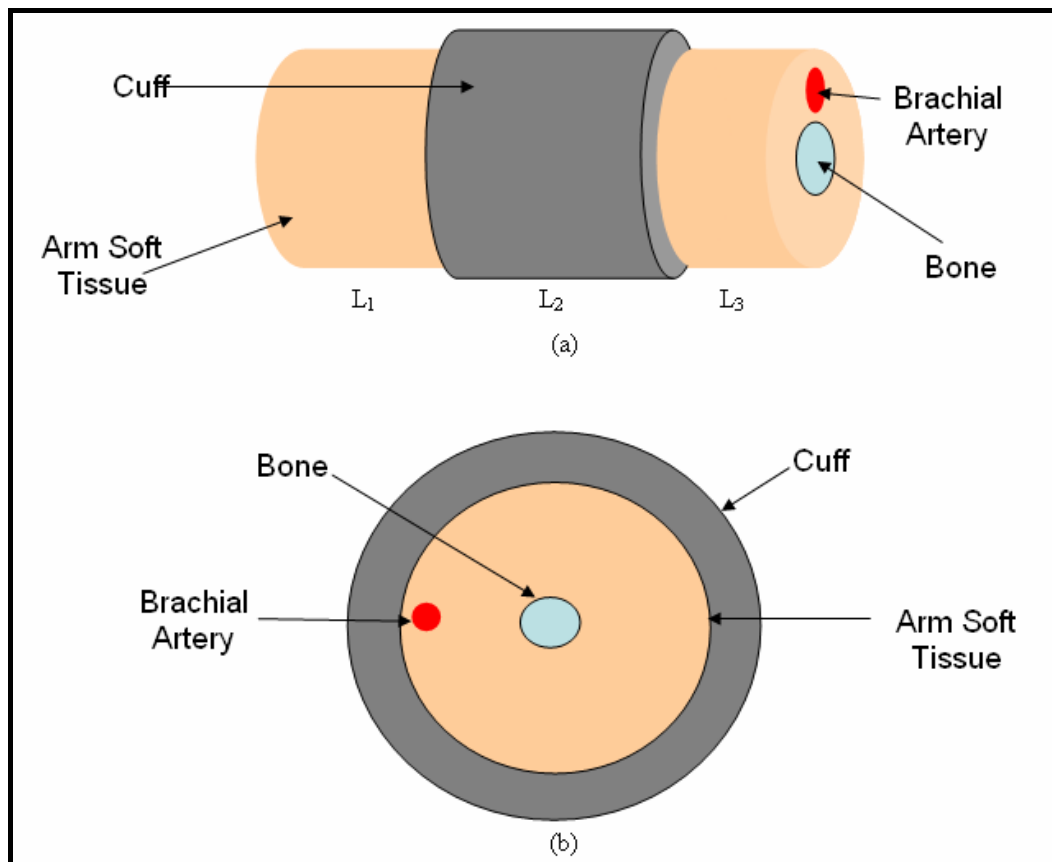


Figure 2.5: A schematic of the upper arm with a pneumatic cuff wrapped around it.

2.3.1 Cuff and Soft Tissue Model

In this work, the upper arm soft tissue is modelled as three adjacent segments as shown in figure 2.5 (a) where the middle segment L_2 is subjected to an external pressure applied by the pneumatic cuff. The pneumatic cuff is modelled as a cylinder made of inner and outer compliant sheets containing air. Current commercial cuffs have a relatively stiff external wall when compared with its internal wall [39, 41]. Also, the compliance of the walls is inversely proportional to the cuff's internal pressure [39, 41].

Using the above assumptions, the following relation between the cuff's internal pressure and the total volume enclosed by its external wall can be written:

$$\frac{dV_e}{dt} = C_e \frac{dp_c}{dt} = \frac{1}{\beta_e(p_c + p_{e0})} \frac{dp_c}{dt} \quad (2.25)$$

where V_e is the volume enclosed by the cuff external wall, C_e is the compliance of the cuff's external wall, p_c is the cuff internal pressure, β_e and p_{e0} are constants that govern the cuff's external wall mechanics. Also the relation between the cuff's internal pressure, pressure on the outside surface of the arm and the total volume enclosed by the cuff's internal wall can be expressed as:

$$\frac{dV_i}{dt} = C_i \left(\frac{dp_b}{dt} - \frac{dp_c}{dt} \right) = \frac{1}{\beta_i(p_c - p_b + p_{i0})} \left(\frac{dp_b}{dt} - \frac{dp_c}{dt} \right) \quad (2.26)$$

where V_i is the volume enclosed by the cuff's internal wall, C_i is the compliance of the cuff's internal wall, p_b is the pressure on the arm's external surface and β_i and p_{i0} are constants that govern the cuff's internal wall mechanics.

Also if it is assumed that the cuff's internal wall thickness is negligible, one can write:

$$V_e = V_i + V_c \quad (2.27)$$

where V_c is the volume of air inside the cuff.

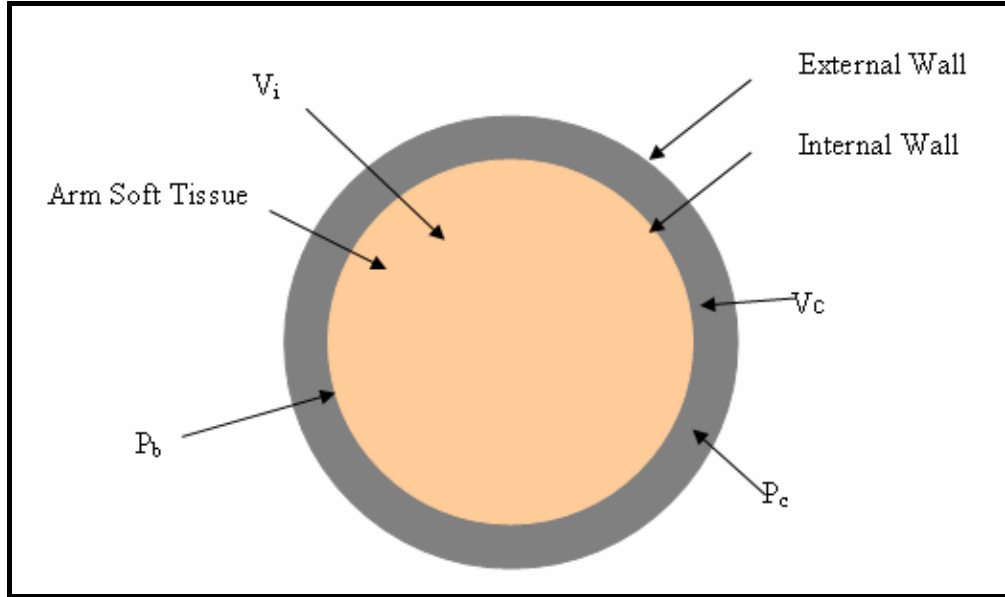


Figure 2.6: a transverse section of the upper arm with a pneumatic cuff wrapped around it showing pressures and the volumes.

Now, differentiating equation 2.27 and using equations 2.25 and 2.26 results in:

$$\frac{1}{\beta_e(p_c + p_{e0})} \frac{dp_c}{dt} = \frac{1}{\beta_i(p_c - p_b + p_{i0})} \left(\frac{dp_b}{dt} - \frac{dp_c}{dt} \right) \quad (2.28)$$

Equation 2.28 expresses the relationship between the cuff's internal pressure and the pressure on the outside surface of the arm.

As mentioned earlier, the arm's middle segment L_2 is subjected to an external pressure applied by the pneumatic cuff while segment L_1 and L_3 are not subjected to any pressure. Hence it can be assumed that the only interaction between the three segments is through the longitudinal stress σ_z . Assuming that stress distribution is symmetric around the axis, leads to the following equations describing stresses and displacements in the upper arm tissue. For each segment the stresses can be written as:

$$\sigma_r = \lambda \varepsilon_z + 2A(G + \lambda) - 2G \frac{B}{r^2} \quad (2.29)$$

$$\sigma_\theta = \lambda \varepsilon_z + 2A(G + \lambda) - 2G \frac{B}{r^2} \quad (2.30)$$

$$\sigma_z = 2A\lambda + (\lambda + 2G)\varepsilon_z \quad (2.31)$$

where $\sigma_r, \sigma_\theta, \sigma_z$ are the radial, tangential and longitudinal stresses respectively. u_r and u_z are the radial and longitudinal displacements respectively. ε_z is the strain in the longitudinal direction and A and B are parameters that depend on the boundary conditions and will be derived hereafter by imposing two boundary conditions.

The displacements can be written as:

$$u_r = Ar + \frac{B}{r} \quad (2.32)$$

$$u_z = \varepsilon_z z \quad (2.33)$$

G and λ are Lamé constants and can be expressed as:

$$G = \frac{E_s}{2(1+\nu_s)} \quad (2.34)$$

$$\lambda = \frac{2G\nu_s}{1-2\nu_s} \quad (2.35)$$

where E_s is the soft tissue elasticity and ν_s is the soft tissue's Poisson's ratio.

The first boundary condition imposed in this model considers the pressure on the outside surface of the arm as equal to the radial stress:

$$\sigma_r = -P_b \quad (2.36)$$

The second boundary condition imposed in this model is that the volume changes due to blood pressure fluctuations in the upper arm are concentrated around the centre of the arm near the bone which is considered to be undeformable. This is done to obtain a simple model that preserves the symmetry of the arm. Hence:

$$u_r(r_i) = \frac{dV_b}{2\pi r_i} \quad (2.37)$$

where u_r is the radial tissue displacement, r_i is the radius of the bone and dV_b is the change in brachial artery volume per unit length. Expressions for A and B can now be found by using equations 2.29, 2.31, 2.32, 2.36, and 2.37:

$$A = \frac{-p_b}{N} - \frac{\lambda\sigma_z}{(\lambda + 2G)N} + \frac{G}{\pi r_e^2 N} dV_b \quad (2.38)$$

$$B = \frac{r_i^2}{N} p_b + \frac{\lambda r_i^2}{(\lambda + 2G)N} \sigma_z + \frac{N r_e^2 - 2G r_i^2}{2\pi r_e^2 N} \quad (2.39)$$

$$N = 2G\left(1 + \frac{r_i^2}{r_e^2}\right) + 4\lambda \frac{G}{\lambda + 2G} \quad (2.40)$$

Substituting equation 2.31 into equations 2.38 and 2.39 then substituting equations 2.38 – 2.40 into equation 2.32 results in an expression describing the changes in the arm's radius $\frac{dr_e}{dt}$:

$$\begin{aligned} \frac{dr_e}{dt} = & \frac{1}{2\pi r_e^2 D} \left(2G \left(\frac{r_e^2 - r_i^2}{r_e} \right) + r_e D \right) \frac{dV_b}{dt} - \frac{1}{D} \left(\frac{r_e^2 - r_i^2}{r_e} \right) \frac{dp_b}{dt} \\ & - \frac{\lambda}{D(\lambda + 2G)} \left(\frac{r_e^2 - r_i^2}{r_e} \right) \frac{d\sigma_z}{dt} \end{aligned} \quad (2.41)$$

Furthermore, an expression describing changes in the segment's length $\frac{dl}{dt}$ can be established for each segment by substituting equation 2.31 into equations 2.38 and 2.39 then substituting equations 2.38 – 2.40 into equation 2.33 and assuming small soft tissue displacements:

$$\begin{aligned} \frac{dl}{dt} = & \left(\frac{2\lambda l}{(\lambda + 2G)D} \right) \frac{dp_b}{dt} + \left(\frac{l}{\lambda + 2G} + \frac{2l\lambda^2}{D(\lambda + 2G)^2} \right) \frac{d\sigma_z}{dt} \\ & - \left(\frac{2\lambda Gl}{(\lambda + 2G)\pi r_e^2 D} \right) \frac{dV_b}{dt} \end{aligned} \quad (2.42)$$

The extravascular pressure is defined as the external pressure acting on the brachial artery. The brachial artery lies longitudinally in the arm and it can thus be assumed that it does not receive any significant longitudinal stresses. The extravascular pressure can be estimated to be equal to the average of radial and tangential stresses in each segment:

$$p_e = \frac{\sigma_r + \sigma_\theta}{2} \quad (2.43)$$

From equation 2.43, an expression describing changes in the extravascular pressure $\frac{dp_e}{dt}$ in each segment can be established by substituting equation 2.31 into equations 2.38 and 2.39 then substituting equations 2.38 - 2.40 into equation 2.43. This results in:

$$\begin{aligned} \frac{dp_e}{dt} = & \left(\frac{2G(3\lambda + 2G)}{D(\lambda + 2G)} \right) \frac{dp_b}{dt} + \left(\frac{2G\lambda(3\lambda + 2G)}{D(\lambda + 2G)^2} - \frac{\lambda}{\lambda + 2G} \right) \frac{d\sigma_z}{dt} \\ & - \left(\frac{2G^2(3\lambda + 2G)}{\pi r_e^2 D(\lambda + 2G)} \right) \frac{dV_b}{dt} \end{aligned} \quad (2.44)$$

In equations 2.41, 2.42, and 2.44, D is equal to:

$$D = \frac{4G\lambda}{\lambda + 2G} + 2G \left(1 + \frac{r_i^2}{r_e^2} \right) \quad (2.45)$$

Differential equations 2.41, 2.42 and 2.44 establish expressions for $\frac{dr_e}{dt}$, $\frac{dl}{dt}$ and $\frac{dp_e}{dt}$ in terms of $\frac{dV_b}{dt}$, $\frac{dp_b}{dt}$ and $\frac{d\sigma_z}{dt}$. Considering the three tissue segments, equations 2.41, 2.42 and 2.43 constitute nine differential equations in eighteen unknowns. Hence nine additional constrains need to be imposed in order for the system to be solvable. These constrains are considered below.

The only external pressure on the upper arm is the pressure applied by the cuff on segment L₂ and is equal to P_b. Hence:

$$p_{b2} = p_b \quad (2.46)$$

$$p_{b1} = p_{b3} = 0 \quad (2.47)$$

Also, from Newton's second law, we can assume that longitudinal stress on each of the three segments is the same, hence:

$$\sigma_z = \sigma_{z1} = \sigma_{z2} = \sigma_{z3} \quad (2.48)$$

Moreover, it can be assumed that there is no significant change in the blood volume in segments L_1 and L_3 because the brachial artery does not collapse in these segments. Hence:

$$\frac{dV_{b1}}{dt} = \frac{dV_{b3}}{dt} = 0 \quad (2.49)$$

In addition, it can be assumed that the total length of the upper arm remains constant and so:

$$\frac{dl_1}{dt} + \frac{dl_2}{dt} + \frac{dl_3}{dt} = 0 \quad (2.50)$$

Now, an expression describing changes in the upper arm longitudinal stress can be found by substituting equation 2.42 into equation 2.50 and making use of equations 2.46 – 2.49:

$$\frac{d\sigma_z}{dt} = \frac{-\left(\frac{2\lambda l}{(\lambda + 2G)D}\right)_2 \frac{dp_b}{dt} - \left(\frac{2\lambda Gl}{(\lambda + 2G)\pi r_e^2 D}\right)_2 \frac{dV_b}{dt}}{\left(\frac{l}{\lambda + 2G} + \frac{2l\lambda^2}{D(\lambda + 2G)^2}\right)_1 + \left(\frac{l}{\lambda + 2G} + \frac{2l\lambda^2}{D(\lambda + 2G)^2}\right)_2 + \left(\frac{l}{\lambda + 2G} + \frac{2l\lambda^2}{D(\lambda + 2G)^2}\right)_3} \quad (2.51)$$

where the subscript indicates the arm segment number.

Also, by assuming that the cuff is always in contact with the outside surface of the arm and assuming small cuff longitudinal displacement, a relationship between the arm's radius r_{e2} and the volume enclosed by the cuff's internal surface V_i can be expressed as:

$$V_i = \pi r_{e2}^2 l_2 \quad (2.52)$$

Differentiating equation 2.52 and using equation 2.26 results in:

$$2\pi r_{e2} \frac{dr_{e2}}{dt} l_2 = \frac{1}{\beta_i(p_c - p_b + p_{i0})} \left(\frac{dp_b}{dt} - \frac{dp_c}{dt} \right) \quad (2.53)$$

Considering the three tissue segment (L_1, L_2, L_3), equations 2.28, 2.41, 2.42, 2.44, 2.51 and 2.53 form a system of twelve differential equations in twelve unknowns ($l_{1,2,3}, r_{e1,2,3}, p_{e1,2,3}, p_c, p_b, \sigma_z$). In these differential equations, the variables are required as inputs to the equation, hence equations 2.28 and 2.53 are to be re-written in order to avoid this open loop iteration and numerically solve the differential equations in MATLAB. Substituting equation 2.51 into equation 2.41 and substituting the result into equation 2.53 results in:

$$\begin{aligned} \frac{dp_b}{dt} = & \left(\frac{1}{J\beta_i(p_c - p_b + p_{i0})} \right) \frac{dp_c}{dt} - \frac{2\pi r_{e2} l_2}{J} \left(\frac{1}{2\pi r_e^2 D} \left(2G \left(\frac{r_e^2 - r_i^2}{r_e} \right) + r_e D \right) \right) \frac{dV_b}{dt} \quad (2.54) \\ & - \frac{2\pi r_{e2} l_2}{J} \left(\frac{\left(\frac{\lambda}{D(\lambda + 2G)} \right)_2 \left(\frac{2\lambda G l}{(\lambda + 2G)\pi r_e^2 D} \right) \left(\frac{r_e^2 - r_i^2}{r_e} \right)_2}{\left(\frac{l}{\lambda + 2G} + \frac{2l\lambda^2}{D(\lambda + 2G)^2} \right)_1 + \left(\frac{l}{\lambda + 2G} + \frac{2l\lambda^2}{D(\lambda + 2G)^2} \right)_2 + \left(\frac{l}{\lambda + 2G} + \frac{2l\lambda^2}{D(\lambda + 2G)^2} \right)_3} \right) \frac{dV_b}{dt} \end{aligned}$$

where,

$$\begin{aligned} J = & \frac{1}{\beta_i(p_c - p_b + p_{i0})} + 2\pi r_{e2} l_2 \left(\frac{1}{D} \left(\frac{r_e^2 - r_i^2}{r_e} \right) \right)_2 \quad (2.55) \\ & - 2\pi r_{e2} l_2 \left(\frac{\frac{\lambda}{D(\lambda + 2G)} \left(\frac{r_e^2 - r_i^2}{r_e} \right) \left(\frac{2\lambda l}{(\lambda + 2G)D} \right)}{\left(\frac{l}{\lambda + 2G} + \frac{2l\lambda^2}{D(\lambda + 2G)^2} \right)_1 + \left(\frac{l}{\lambda + 2G} + \frac{2l\lambda^2}{D(\lambda + 2G)^2} \right)_2 + \left(\frac{l}{\lambda + 2G} + \frac{2l\lambda^2}{D(\lambda + 2G)^2} \right)_3} \right) \end{aligned}$$

Substituting equation 2.54 into equation 2.28 results in:

$$\frac{dp_c}{dt} = \frac{2\pi r_e l_2}{JK\beta_i(p_c - p_b + p_{i0})} \left(\frac{1}{2\pi r_e^2 D} \left(2G \left(\frac{r_e^2 - r_i^2}{r_e} \right) + r_e D \right) \right) \frac{dV_b}{dt} \quad (2.56)$$

$$- \frac{2\pi r_e l_2}{JK\beta_i(p_c - p_b + p_{i0})} \left(\frac{\left(\frac{\lambda}{D(\lambda + 2G)} \right)_2 \left(\frac{2\lambda Gl}{(\lambda + 2G)\pi r_e^2 D} \right)_2 \left(\frac{r_e^2 - r_i^2}{r_e} \right)_2}{\left(\frac{l}{\lambda + 2G} + \frac{2l\lambda^2}{D(\lambda + 2G)^2} \right)_1 + \left(\frac{l}{\lambda + 2G} + \frac{2l\lambda^2}{D(\lambda + 2G)^2} \right)_2 + \left(\frac{l}{\lambda + 2G} + \frac{2l\lambda^2}{D(\lambda + 2G)^2} \right)_3} \right) \frac{dV_b}{dt}$$

where K is:

$$K = \frac{1}{\beta_e(p_c + p_{e0})} + \frac{1}{\beta_i(p_c - p_b + p_{i0})} - \left(\frac{1}{J(\beta_i(p_c - p_b + p_{i0}))^2} \right) \quad (2.57)$$

In the Pulsecor device, a piezoelectric sensor is attached on to the circumference of the pneumatic cuff outside wall. The sensor measures circumferential strains in the cuff external wall. Hence a relationship is required between the cuff pressure and the strain on the cuff external wall. It is known that the volume of a cylinder can be written as:

$$V = \pi r^2 l \quad (2.58)$$

Commercial cuffs are designed to be relatively stiff in the longitudinal direction [41]; hence it can be assumed that any change in the cuff volume is attributed to change in its radius. By using equation 2.25 one can write:

$$\frac{dR}{dt} = C_e \frac{dp_c}{dt} = \frac{1}{2\pi R l_2 \beta_e(p_c + p_{e0})} \frac{dp_c}{dt} \quad (2.59)$$

Now the circumferential strain can be written as:

$$\frac{dR}{R_0} = \frac{\frac{dR}{dt} dt}{R_0} \quad (2.60)$$

The above system of differential equations can now be solved numerically using MATLAB. The only missing variable is the change in the volume of blood under the cuff $\frac{dV_b}{dt}$ which will be derived in the next section.

2.3.2 Brachial Artery Model

In this section, the segment of the brachial artery under the pneumatic cuff is modelled. A lumped parameter model is used to describe the blood volume changes under the cuff where all blood changes are assumed to be concentrated in a single representative section of the artery.

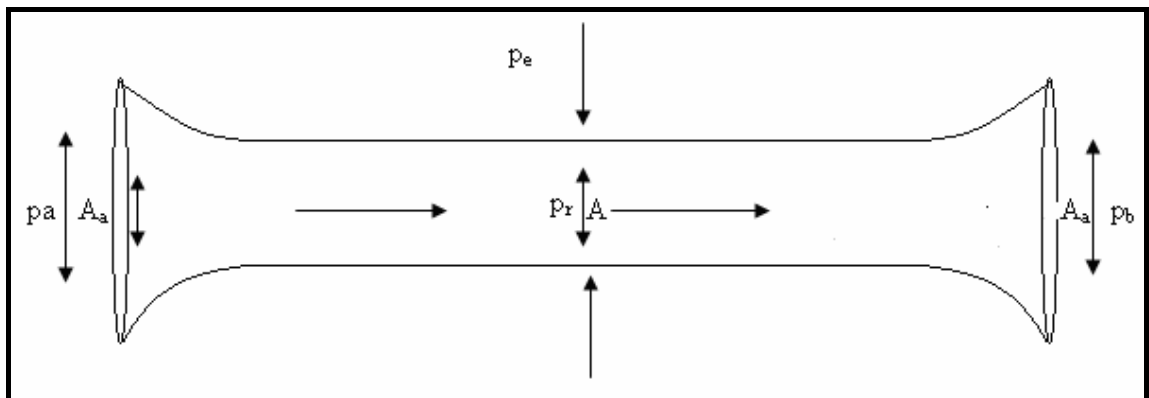


Figure 2.7: A schematic of the brachial artery compressed by a pneumatic cuff. p , v and A are the blood pressure, blood velocity and artery area at different sections of the artery.

Muriso et al [40, 41] modelled and defined expressions describing all pressure losses caused by the collapse of the brachial artery caused by the cuff. These included losses due to the conversion of pressure into kinetic energy, inertial and viscous losses and expansion losses due to the reopening of the artery [40,41]. These were simulated using MATLAB and were found to decrease the brachial artery pressure (p_a) by a maximum of 4% near diastolic pressure. The computation power required to solve the differential equations describing the pressure losses outweigh the improvement in accuracy of the model and therefore were ignored. Hence, in this work, (p_r) is assumed to equal the intravascular pressure (p_a) and is used to represent the pressure under the pneumatic cuff.

In this research it is assumed that the total blood volume changes under the pneumatic cuff are due to blood volume changes in the brachial artery. This is obviously not entirely true as blood volume change is also caused by blood volume change in the capillaries and veins of the upper arm. However, these segments are compressed during the measurement and their volume changes can be assumed to be insignificant. Hence the change in blood volume per unit length under the cuff ($\frac{dV_b}{dt}$) is assumed to be equal to the change in the cross sectional area of the brachial artery ($\frac{dA}{dt}$).

Now the cuff and soft tissue model can be linked to the brachial artery model by finding an expression describing the compliance of the brachial artery under the cuff. This is given by a relationship between the area of the brachial artery under the pneumatic cuff (A) and the transmural pressure ($p_a - p_e$). Two separate relations must be formed, one describing the artery compliance at positive transmural pressure and another describing the artery compliance at negative transmural pressure.

At positive transmural pressure, the artery can be assumed to maintain its circular cross section and hence the Laplace law can be used to describe the relationship:

$$(p_a - p_e) \sqrt{\frac{A}{\pi}} = \sigma h = (\sigma_e + \sigma_v) h \quad (2.61)$$

where σ is the circumferential stress, σ_e is the elastic stress, σ_v is the viscous stress and h is the artery wall thickness.

A bi-exponential relationship is used to describe the relationship between the brachial artery elastic circumferential stress and circumferential strain in order to reproduce experimental results reported by Learoyd and Taylor [45]:

$$\sigma_e(A) = \frac{E_0}{\beta_a'} (\exp(\beta_a' \varepsilon_a) + \exp(\beta_a'' \varepsilon_a^2) - 2) \quad (2.62)$$

where β_a' , β_a'' , E_0 are constants and ε_a is the circumferential strain which is defined by:

$$\varepsilon_a = \frac{\sqrt{A} - \sqrt{A_0}}{\sqrt{A_0}} \quad (2.63)$$

The wall thickness (h) at positive transmural pressure can be described by assuming the artery wall to be incompressible and that longitudinal strain is negligible:

$$h = -\sqrt{\frac{A}{\pi}} + \sqrt{\frac{A}{\pi} + 2h_0\sqrt{\frac{A_0}{\pi}} + h_0^2} \quad (2.64)$$

where h_0 and A_0 are the wall thickness and cross sectional area at zero transmural pressure respectively.

The viscous stress can be assumed to be linearly dependent on the rate of change of the artery wall strain and can be written as:

$$\begin{aligned} \sigma_v &= \eta \frac{d\varepsilon_a}{dt} \\ &= \frac{\eta}{2\pi\sqrt{\frac{A_0}{\pi}}\sqrt{\frac{A}{\pi}}} \frac{dA}{dt} \end{aligned} \quad (2.65)$$

Finally by using equations 2.61 – 2.65, a relation for the rate of change of the brachial artery area at positive transmural pressure can be expressed as:

$$\frac{dV_b}{dt} = \frac{dA}{dt} = \frac{2(p_a - p_e)A\sqrt{\frac{A_0}{\pi}}}{\eta \cdot h(A)} - 2\frac{\sqrt{\frac{A_0}{\pi}}\sqrt{\pi A}}{\eta} \sigma_e(A) \quad (2.66)$$

As the transmural pressure become negative, the brachial artery collapses and loses its cylindrical shape. Hence, the Laplace law can not be applied and the tube law is used to describe the relationship between the transmural pressure and the artery cross sectional area:

$$\frac{dV_b}{dt} = \frac{dA}{dt} = k \left(\frac{p_a - p_e}{k_p} - 1 + \left(\frac{A}{A_0} \right)^{-3/2} \right) \quad (2.67)$$

where k is a proportionality factor and k_p is a constant that depends on the geometry and material properties of the brachial artery and is described by:

$$k_p = \frac{h_0 E_0}{3r_{a0}}$$

The constant k_p determines the way the artery will collapse while k is a constant parameter that was calculated by keeping $\left(\frac{dA}{dt}\right)$ continuous between positive and negative transmural pressures. Equation 2.67 can now be written as:

$$\frac{dV_b}{dt} = \frac{dA}{dt} = \frac{2(p_a - p_e)A_0 \sqrt{\frac{A_0}{\pi}}}{\eta h_0} - \frac{2k_p A_0 \sqrt{\frac{A_0}{\pi}}}{\eta h_0} \left(1 - \left(\frac{A}{A_0} \right)^{-3/2} \right) \quad (2.68)$$

Now that an expression linking the change in the blood volume under the cuff and the intravascular and extravascular brachial artery pressure has been established, the Cuff - Soft Tissue - Brachial Artery model is linked and the transmission of the pressure across the soft tissue and the pneumatic cuff is also found. The material properties and geometry for the cuff, arm soft tissue, and the brachial artery used in this model were adopted from the values reported by Muriso et al [39-41] and are listed in section 3.3.

2.4 Closure

A mathematical formulation has been developed to describe pressure wave propagations and reflection in elastic branching arteries. Also, the transmission of pressure from the brachial artery through the arm soft tissue to the pneumatic cuff has been established. This formulation will be used in Chapter 3 to simulate the pressure wave propagation and reflection phenomenon in the aorta and the brachial artery in order to reproduce the brachial artery pressure and the strain imposed on the cuff external wall.

Chapter 3 Model Development and Simulation

3.1 Introduction

This chapter is divided into three sections. The first section uses the acoustic model developed in Chapter 2 to build a physiologically based model of the central systemic arteries that can be used to simulate the brachial artery pressure. The second section uses the Brachial Artery-Soft Tissue-Cuff Model developed in Chapter 2 to describe the transmission of this brachial artery pressure through the arm soft tissue and the pneumatic cuff. The third section describes how these two models can be combined to obtain a complete model that can be used to non-invasively estimate the brachial artery pressure and strain contour created on the cuff outside wall.

3.2 Acoustic Model

In this section, the acoustic model developed in Chapter 2 was used to build a model that estimates the intravascular pressure at the brachial artery. Firstly, the tapering and the variation of the material properties in the systemic arteries were examined and modelled. The input wave to the system from the heart was then determined and mathematically described. Also, the sites of wave reflection within the system were adopted from the available literature. Finally, the complete acoustic model was simulated by describing the propagation and reflection of pressure waves generated by the heart contraction and tracing these waves as they reach the brachial artery.

3.2.1 Geometric Consideration

The central arteries take the shape of tapered tubes. Since the speed of wave propagations is influenced by the area, thickness and modulus of elasticity, it was important to consider variations in these geometric and material properties when developing a model.

In this research, the arteries of interest were divided into small lumps E1, E2, E3... etc with constant geometric and mechanical properties as shown in figure 3.1. This assumption simplified the governing equations dramatically and reduced the complexity of the mathematical solution.

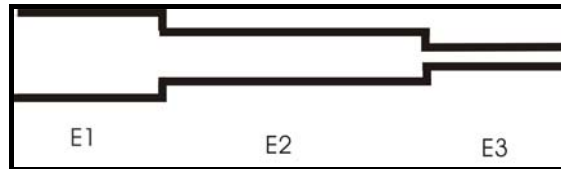


Figure 3.1: The arteries are divided into elements with different properties.

In order to find the optimum number of lumps which gives an accurate and acceptable solution, calculations are conducted on the aorta and the brachial artery. Westerhof et al [46] conducted experiments on human arteries and listed the thickness, radius and the modulus of elasticity at 10 positions along the aorta and 7 positions along the subclavian and brachial arteries as given in figures 3.2 and 3.3. These data varied smoothly and were fitted with appropriate functions. A suitable power function was found to describe the variation in thickness and radius of the aorta, while a linear function was used to describe the thickness and radius variation of the subclavian-brachial arteries.

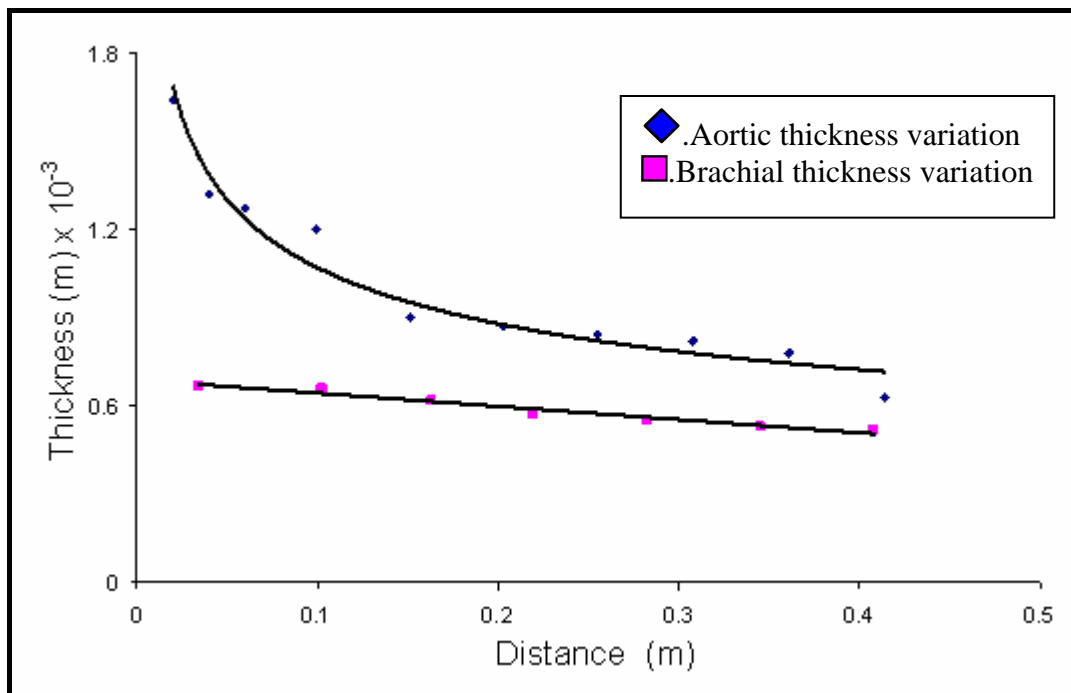


Figure 3.2: Power Function describing the human aorta thickness variation and a linear function describing the thickness variations along the subclavian and brachial arteries.

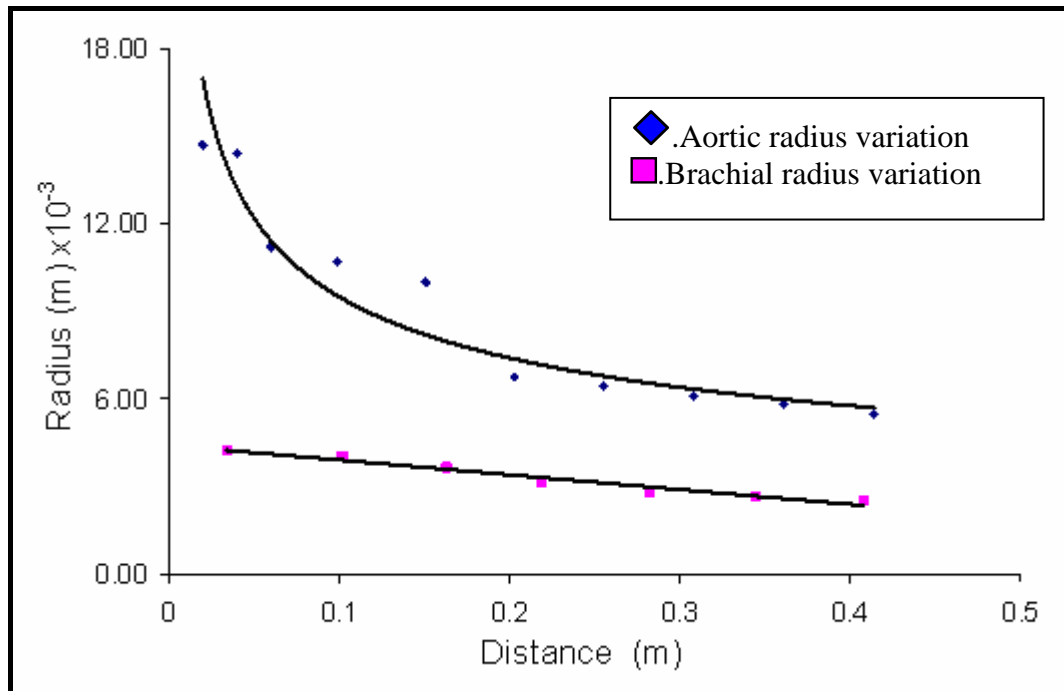


Figure 3.3: Power Function describing the human aorta radius variations and a linear function describing the human subclavian and brachial artery radius variations.

The next step was to determine the appropriate number of lumps that would accurately describe wave propagation in the arteries. The model was simulated for different numbers of lumps using equation 2.9. Figure 3.4 shows the relation between the time it takes for the wave to travel through the aorta and brachial artery versus the number of lumps used. This figure shows that the time converged after 24 and 16 lumps for the aorta and the brachial artery respectively. Hence the aorta was divided into 24 lumps of 0.018m length each while the subclavian and brachial arteries were divided into 16 lumps of 0.026m length each.

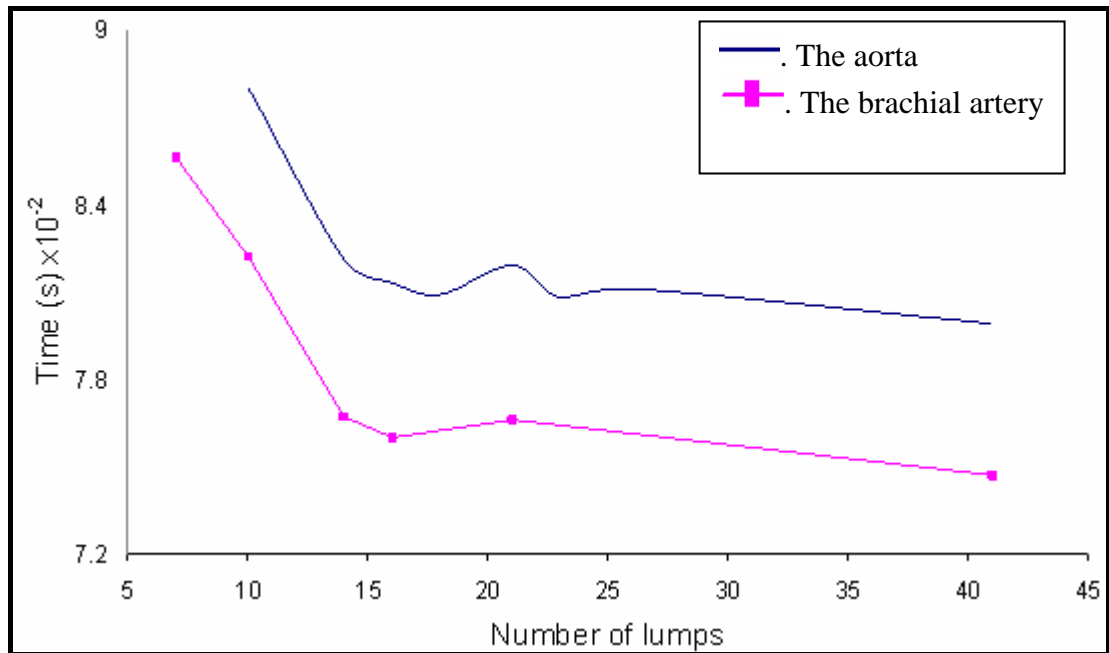


Figure 3.4: Pressure wave travelling time vs. number of lumps

3.2.2 Input Wave to the System

The left ventricle is the most muscular chamber of the heart. In normal conditions, it generates a pressure of approximately 120 mmHg when it contracts. The pressure can be much higher during exercise and in some pathological conditions [4].

When the electric excitation wave reaches the left ventricle, the ventricle myocardium starts to contract and hence the pressure inside the ventricle increases. When the left ventricle pressure exceeds the left atrium pressure, blood starts to flow back into the left atrium and creates a back flow which closes the mitral valve. As long as the left ventricle pressure remains less than pressure in the aorta, the aortic valve remains closed. During this period when left ventricle pressure is less than the pressure in the aorta, both the mitral and aortic valves are closed and thus the volume of the left ventricle stays constant. This period is called the isovolumic contraction period.

When the left ventricular pressure becomes greater than the aortic pressure, the aortic valve opens and blood flows from the left ventricle into the aorta. As contraction continues, the left ventricle pressure continues to rise and blood continues to accelerate into the aorta. Eventually the contraction ceases and left ventricle pressure starts to decrease. Finally, the velocity of the blood decreases to zero and begins to reverse. The back flow closes the aortic valve which marks the end of ventricular systole. This

sequence of events can be seen in figure 3.5. The pressure transmitted from the left ventricle to the ascending aorta can be assumed to be the supra-diastolic left ventricular pressure as shown in figure 3.6 because the aortic valve opens only at this pressure.

In this research, the cardiac cycle was assumed to be periodic and repeat every 0.8 seconds. Hence the ventricular pressure was assumed to be a periodic function and was reconstructed using Fourier series.

One supra-diastolic left ventricular pulse was selected. The pulse's period (T) was 0.8 seconds which was further divided into 38 equally spaced intervals (N) as shown in figure 3.7.

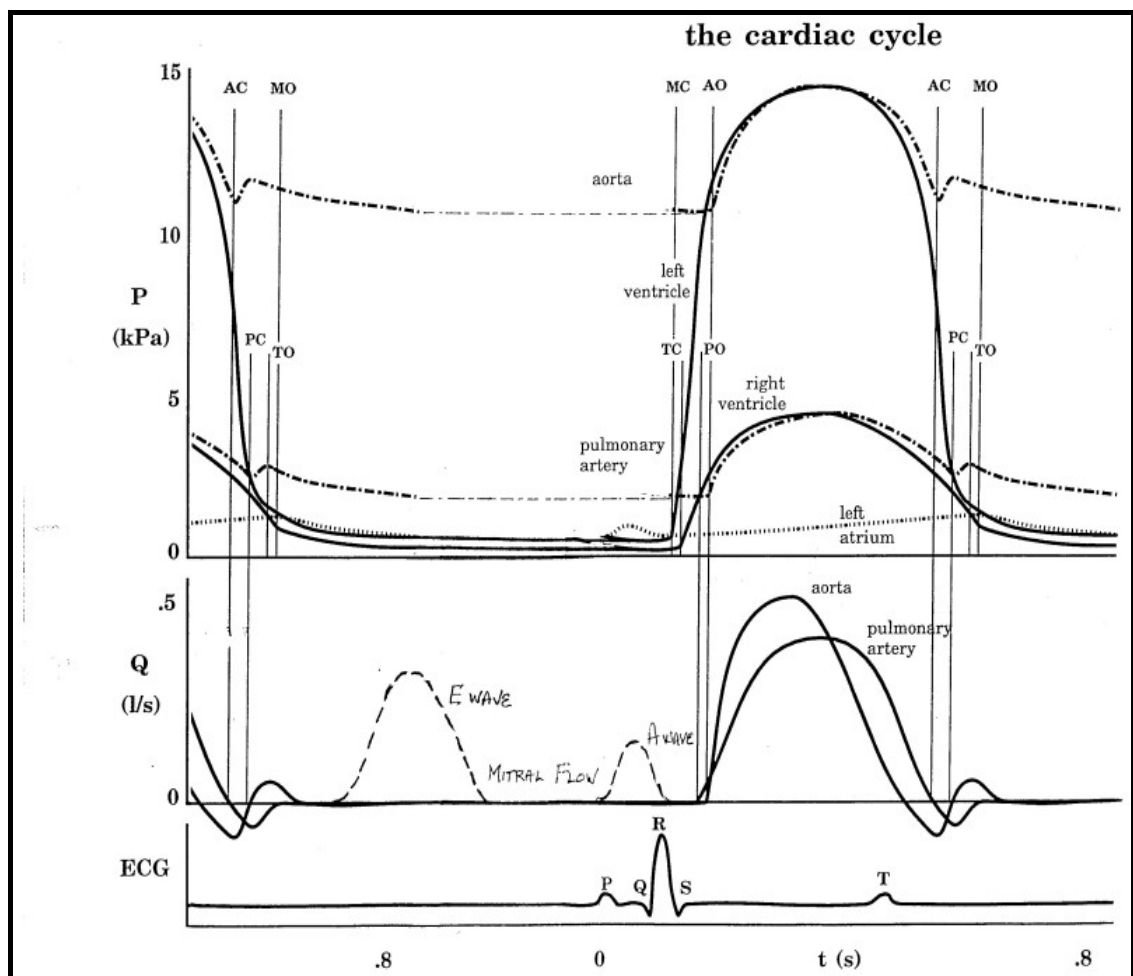


Figure 3.5: Tracings of pressure, flow and ECG during the cardiac cycle of a normal adult. [4]

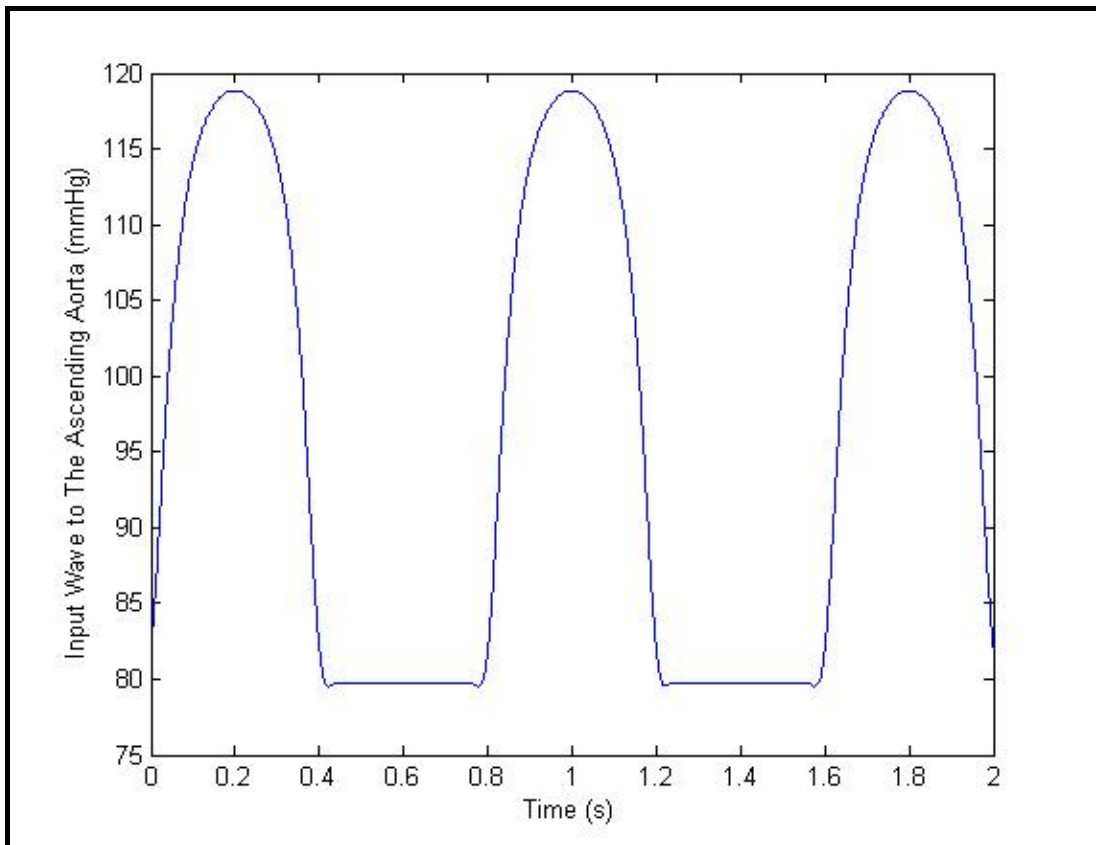


Figure 3.6: The periodic pressure wave transmitted from the left ventricular to the ascending aorta.

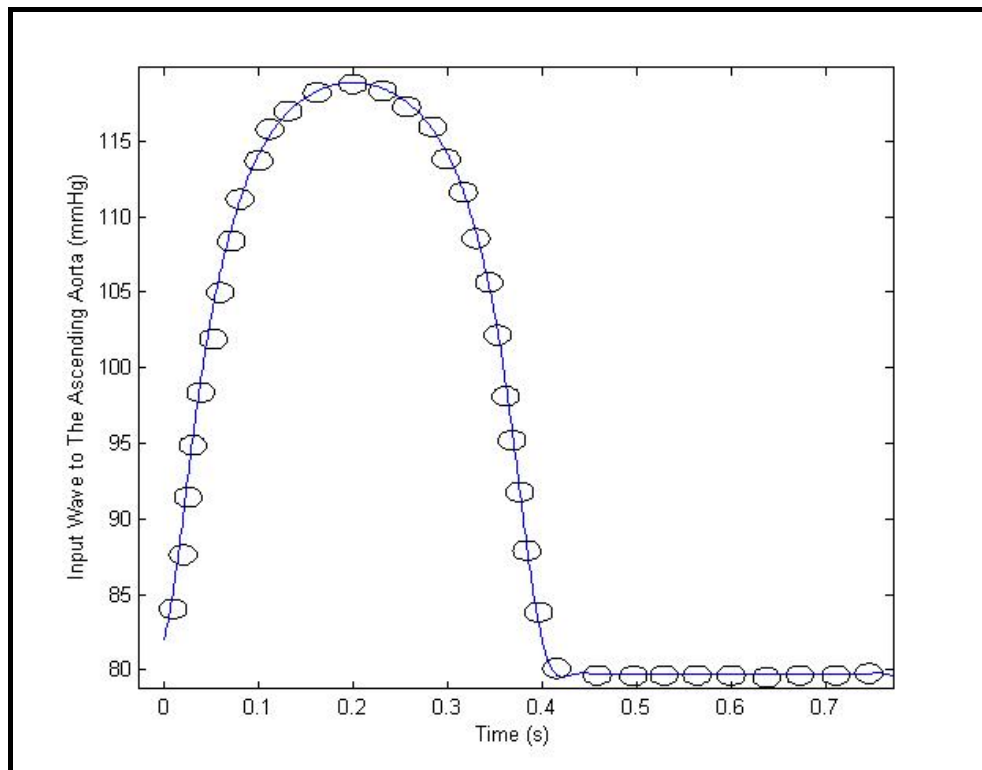


Figure 3.7: One supra-diastolic pressure pulse divided into 38 equally spaced intervals (N).

Each of the 38 ordinates was designated by the letter S. The Fourier coefficients A_0 , A_n and B_n were then calculated using:

$$A_n = \frac{2}{N} \sum_{s=0}^N y_s \cos n\omega t_s \text{ (for } n=0, 1, 2, \dots, \frac{N}{2}) \quad (3.1)$$

$$B_n = \frac{2}{N} \sum_{s=0}^N y_s \sin n\omega t_s \text{ (for } n=0, 1, 2, \dots, \frac{N}{2}) \quad (3.2)$$

$$A_0 = \frac{\sum y_s}{N} \quad (3.3)$$

where

$$\omega = \frac{2\pi}{T} \quad (3.4)$$

The function is then defined by a finite series where the function value (y_s) can be found for any time (t_s):

$$y_s = \frac{A_0}{2} + \left[\sum_{n=1}^{N/2} A_n \cos n\omega t_s + \sum_{n=1}^{N/2} B_n \sin n\omega t_s \right] \quad (3.5)$$

3.2.3 Wave Reflection Locations

The precise locations of the major reflection sites in the human aorta have been studied in several past and recent publications. It has been reported that the major reflection site is in the abdominal aorta and is located at the iliac bifurcation [33-35]. Hence in this work, the impedance mismatch between the abdominal aorta and the iliac arteries was assumed to be the only significant source of reflection for forward travelling waves in the lower body. The geometry and material properties for the aorta and the iliac arteries were obtained from experimental data reported by Westerhof et al [46].

The compression of the upper arm by the pneumatic cuff causes a sudden decrease in the area of the brachial artery which results in large impedance mismatch that leads to a reflection at this site. Furthermore, from the data reported by Westerhof et al [46], the

reflected brachial wave will reflect negatively when it reaches the mouth of the subclavian artery because of the sudden increase in area [43, 47]. Hence, in this work the following wave reflection model is proposed.

Any wave generated by the heart travels via the aorta into the brachial artery and iliac bifurcation. The aortic wave is reflected at the iliac bifurcation and then travels back to the brachial artery. The original wave which travelled to the brachial artery reflects back due to the cuff and travels to the mouth of the subclavian artery where it reflects back negatively to the brachial artery. Secondary reflections other than the one produced by the occlusion caused by the cuff are not considered in this work because their magnitude is too small to be detected by the sensors on the cuff. Hence the above three waves reach the brachial artery at different times as shown in figure 3.8.

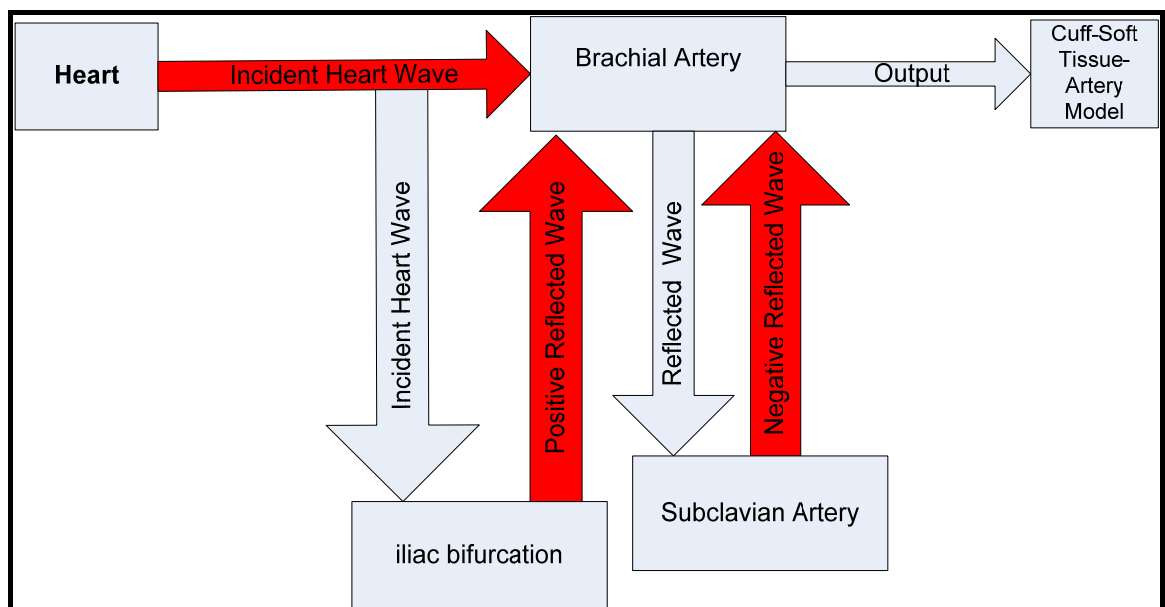


Figure 3.8: A schematic diagram showing the propagation and reflection of pressure waves in the system.

3.2.4 Simulation of Acoustic Model

The above model was simulated using the MATLAB software package. An invasive left ventricle waveform obtained from (Nichols & O'Rourke) was used to represent the periodic pressure wave generated from the heart [3]. This wave was then represented using a Fourier series as an input into the ascending aorta. The left ventricle supra-diastolic pressure was used because the aortic valve opens at this pressure and the pressure of the ventricle is transferred to the ascending aorta. The Brachial Artery-Soft

Tissue-Cuff model was then used to determine the area of the brachial artery under the inflated cuff. This will be explained further in Section 3.3.

Equations 2.13, 2.14, 2.16 and 2.21 were used to calculate the reflection coefficient at the iliac bifurcation, the brachial artery and the mouth of the subclavian artery. The radius and thickness of the iliac arteries were also obtained from work by Westerhof et al [46]. These were used to calculate the area mismatch between the descending aorta and the iliac bifurcation.

The travel time was then calculated using equation 2.9 for each element. The total time for the waves to travel from the heart and the respective reflection sites to the brachial artery was determined by adding the time for each element between the heart and the reflection sites to the brachial artery. Figure 3.9 shows the three waves that make up the brachial artery wave and the combination of these waves. It is important to note that the timing of these waves plays a major role in determining the shape of the brachial artery wave.

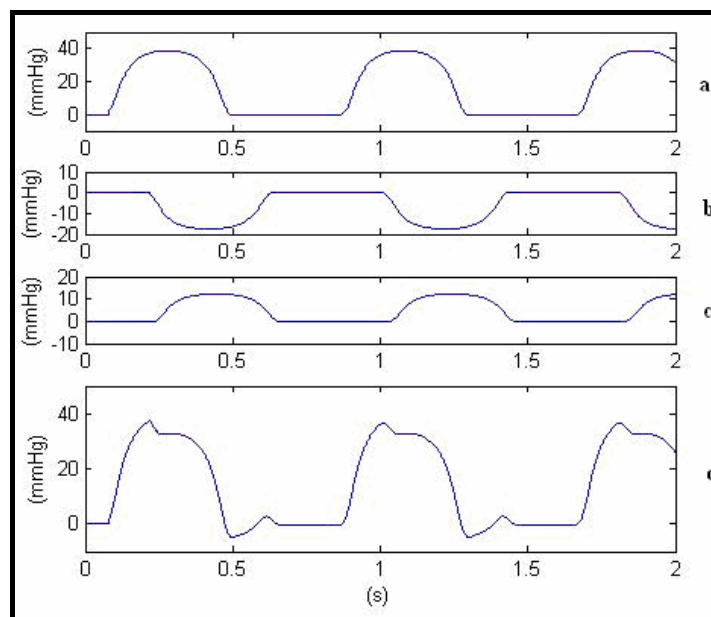


Figure 3.9: Pressure waves determined at the brachial artery: a) Heart wave, b) First reflected wave from the subclavian artery, c) Second reflected wave from the iliac bifurcation, d) Combined wave.

3.3 Cuff - Soft Tissue - Brachial Artery Model

In this section, the model parameters and input quantities used in this research for the pneumatic cuff, soft tissue and the brachial artery are defined. The lumped parameter models are then linked together and simulated to describe the transmission of pressure

from the brachial artery through the arm soft tissue to the pneumatic cuff. The ordinary differential equations are then numerically solved using the MATLAB software package.

3.3.1 Lumped Models Parameters

In this section, all the lumped models' parameters and input quantities are defined using values obtained from the literature. Firstly the parameters of the cuff β_e , p_{e0} , β_i , p_{i0} were adopted from experiments conducted by Ursino et al [39, 41] where two different experiments were conducted on the inside and the outside of the cuff to characterise their compliance. The parameters of the cuff are listed in table 3.1.

Table 3.1: Parameters of the pneumatic cuff

Parameter	Value
β_e	0.0038 cm ⁻³
p_{e0}	1.5832 cm ⁻³
β_i	0.00136 dyn/cm ²
p_{i0}	5.5998 dyn/cm ²

The parameters of the arm soft tissue were also adopted from experiments conducted by Ursino et al [41]. Average values for the upper arm initial radius and length were used [41]. The arm tissue elastic properties were estimated in an experimental study performed on healthy subject. The Young's modulus (E_s) was assumed to increase linearly with the pressure on the outside surface of the arm (p_b):

$$E_s = E_{s0} + \beta_s p_b \quad (3.6)$$

where E_{s0} is the Young modulus at zero pressure and β_s is a constant parameter estimated from the experiments.

Table 3.2 lists the values used in this research for the parameters of the upper arm soft tissue.

Table3.2: Parameters of the upper arm soft tissue

Parameter	Value
r_{e0}	5.4 cm
r_i	1.2 cm
L_1	7 cm
L_2	14 cm
L_3	7 cm
E_{s0}	$4 * 10^5 \text{ dyn/cm}^2$
β_t	8
v_s	0.45

The geometry for the brachial artery (A_o) and (h_0) have been adopted from data reported in previous research [41]. The length of the brachial artery (L) was assumed to be equal to the cuff length (L_2) because this is where all the interactions between the three models take place. Also, the parameters that describe the mechanics of the brachial artery wall (E_0 , β_a' , β_a'' and η) have been adopted from the work reported by Ursino and others [40, 41]. The brachial artery parameters used in this research are listed in table 3.3:

Table 3.3: Parameters of the brachial artery

Parameter	Value
L	14 cm
A_o	0.166 cm^2
h_0	0.0575 cm
E_0	$3 * 10^5 \text{ dyn/cm}^2$
η	$4 * 10^3 \text{ dyn/cm}^2$
β_a'	5
β_a''	21.5

3.3.2 Simulating the Interactions between the Lumped Models

The purpose of this section is to illustrate the connections among the three lumped parameter models and to show how these models can be simulated on a computer.

Before inflating the cuff, the area of the brachial artery at diastolic pressure was estimated by using the brachial artery model described in Chapter 2. The intravascular pressure (p_a) was iteratively increased from zero to 80 mmHg while keeping the extravascular pressure zero. The brachial artery area was then calculated using the brachial artery model.

The cuff pressure in the cuff model was then iteratively increased from zero to the required pressure for the simulation. The change in the upper arm soft tissue and the brachial artery state variables was then calculated using the cuff, soft tissue and the brachial artery models.

The brachial artery pressure was then fed into the brachial artery model to determine the rate of change in the brachial artery volume ($\frac{dV_b}{dt}$). This was then fed into the soft tissue and cuff model where changes in the extravascular pressure, pressure on the arm outside surface, and other state variables were calculated. The change in the pressure on the outside surface of the upper arm was then fed into the cuff model where changes in the cuff pressure and the strain on the cuff outside wall were determined. Figure 3.10 shows the sequence of events described above.

Figure 3.11 shows how the three models were simulated numerically using MATLAB and the differential equations solved in each model. Block 1 shows the calculation of the brachial area at diastolic blood pressure. This area is then used as an initial condition in block 2 where the inflation of the pneumatic cuff is simulated and the new state variables are found. The new state variables are then used in block 3 where the brachial artery pressure wave form is fed into the model. The model is then used to estimate a number of variables including the fluctuations in cuff pressure and cuff strain.

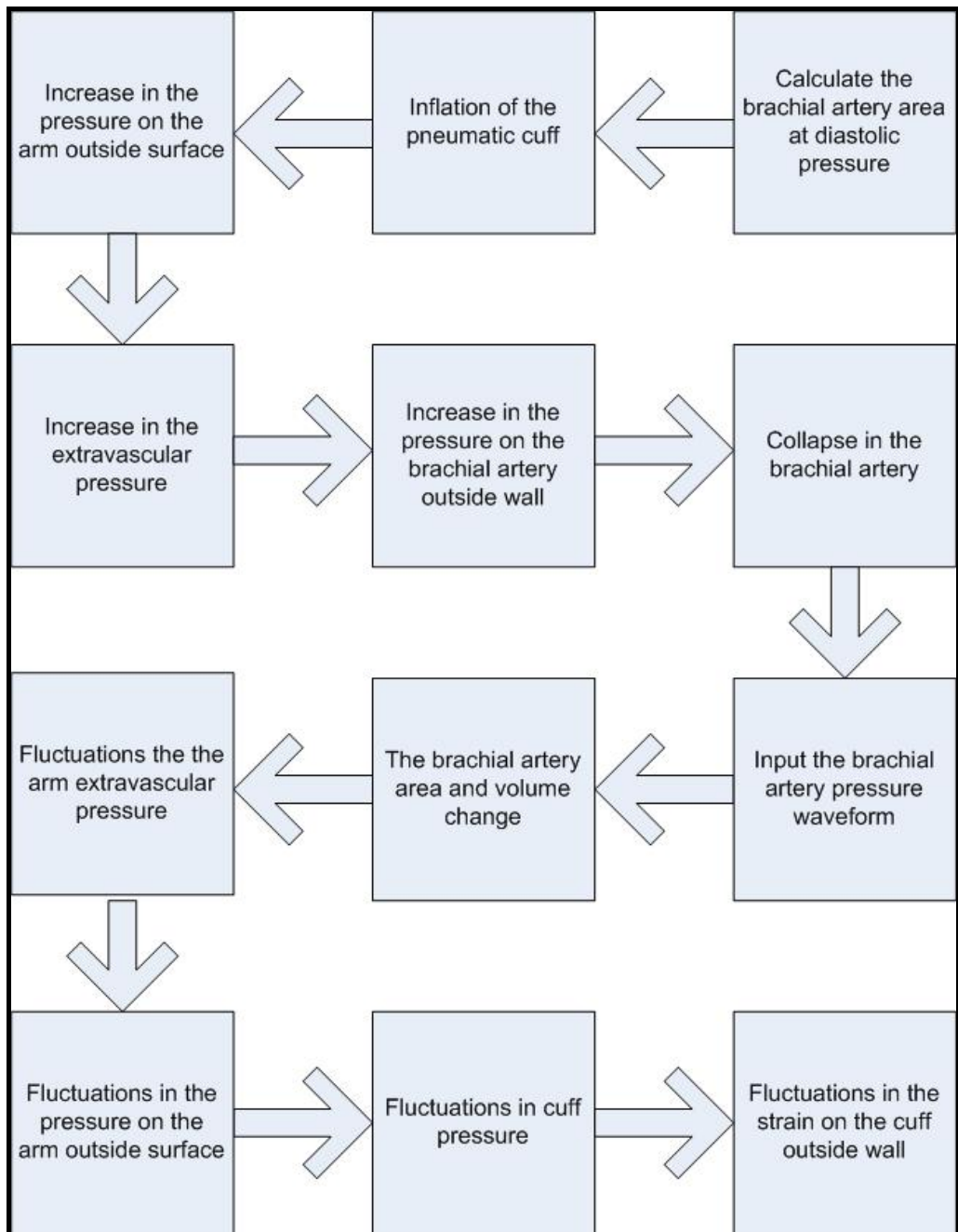


Figure 3.10: Flow chart describing the chain of events in simulating the Cuff-Soft Tissue-Brachial Artery Model.

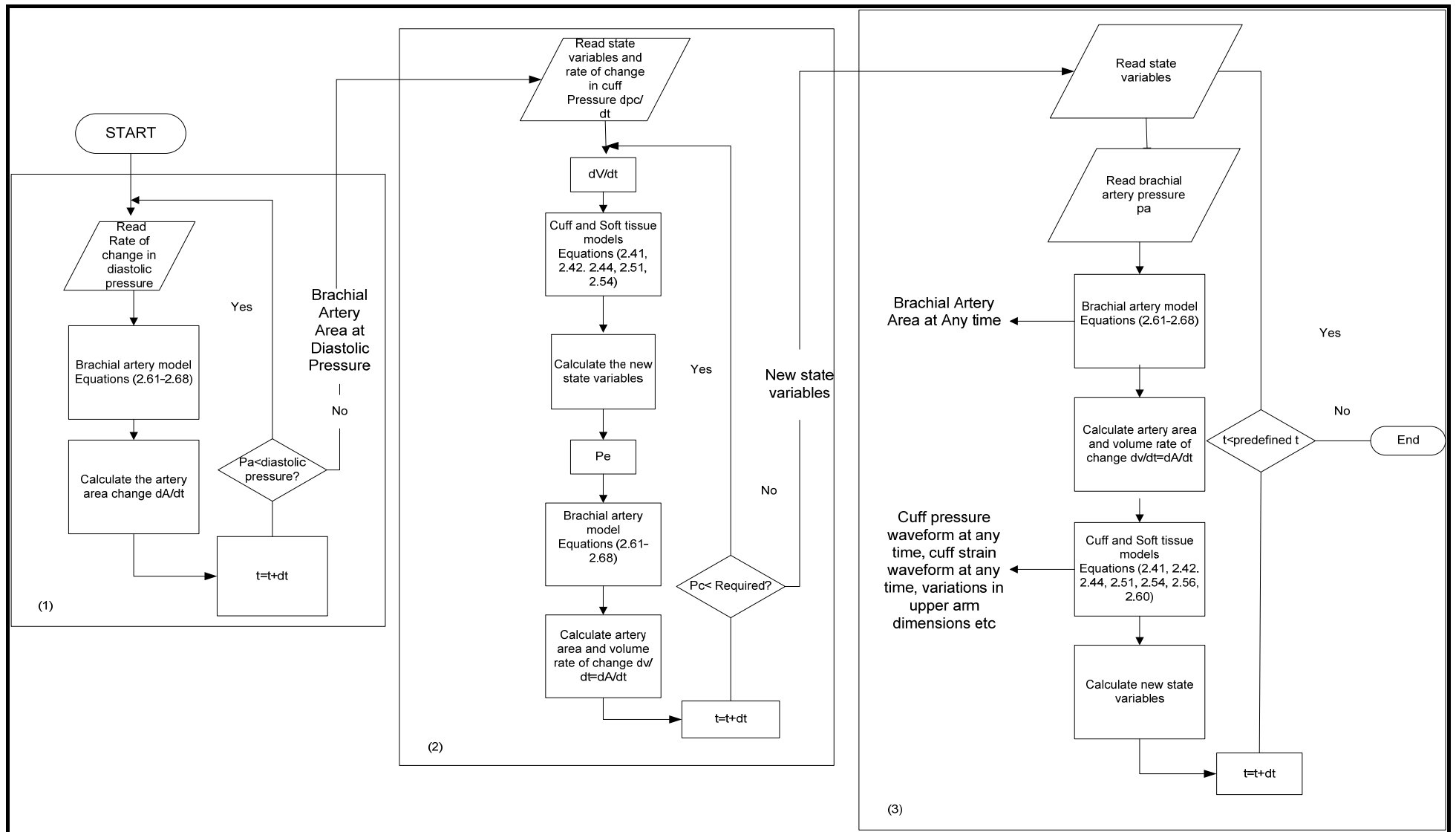


Figure 3.11: Flow chart of how the model was implemented using MATLAB.

3.4 Combined Model

In this section, the acoustic model and the Cuff-Soft Tissue-Brachial Artery model described in Sections 3.2 and 3.3 are combined. The area of the brachial artery under the pneumatic cuff was calculated using Cuff-Soft Tissue-Brachial Artery model. This area was then used by the acoustic model to calculate the wave reflection at the brachial artery. The acoustic model was then simulated as described in Section 3.2 where brachial artery pressure waveform is replicated. This pressure waveform was then fed into the Cuff-Soft Tissue-Brachial Artery model where the fluctuations in the cuff outer wall were simulated. The combined model is illustrated in figure 3.12.

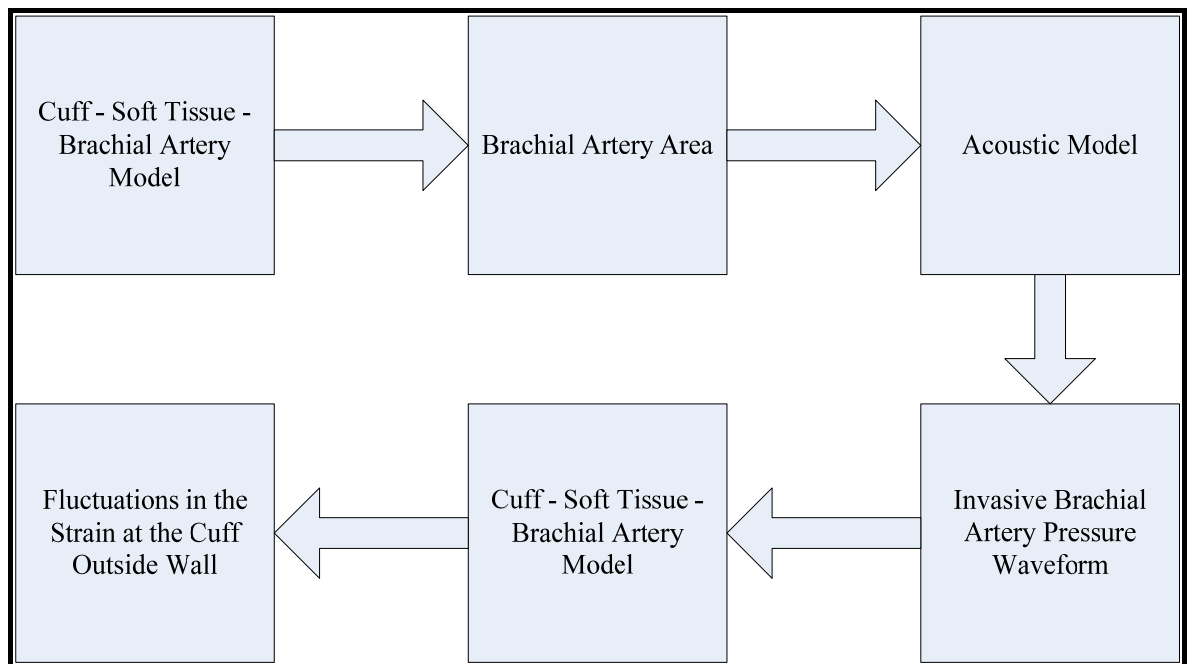


Figure 3.12: A flow diagram showing the connections among the combined model.

The combined physiologically based mathematical model provides a computer simulation of the pressure waves in the central arteries and the contours picked up by the Pulsecor device. It is capable of simulating the pressure contours in the brachial artery and the non-invasive estimation of these pressure contours by detecting the strain on the outside wall of the pneumatic cuff. The computer simulated model provides a quick and easy to use tool to investigate the effect of variations in the central arteries geometry and material properties on the brachial artery pressure contours and the strain on the cuff outside wall. It can also be used to investigate the effect of variations in the pneumatic cuff and soft tissue properties on the acquired pressure and strain contours.

This model is very useful in the development and validation of the Pulsecor device as it will help in developing the stiffness estimation algorithms and investigate the sensitivity of the results to other factors such as artery geometry and cuff pressure.

3.5 Closure

In this chapter, a physiologically based model is developed for the central systemic arteries where the brachial artery pressure can be estimated. Also, a Cuff-Soft Tissue-Brachial Artery model has been developed where the transmission of brachial artery pressure through the arm soft tissue and the pneumatic cuff is described. These two models are combined to provide a computer simulation of non-invasive indirect brachial artery pressure estimation.

This combined model will be used in Chapter 4 to simulate the brachial artery pressure waveforms and the strain on the outer wall contours of the cuff. The model will also be used to investigate the sensitivity of the model to variations in some important model parameters.

Chapter 4 Simulation Results

4.1 Introduction

In this chapter, the simulation results for the combined model discussed in Chapter 3 are presented. The brachial artery pressure and strain on the pneumatic cuff outer wall are first simulated using the model. Important features in the simulated waveforms are then defined and extracted. These feature points are used to calculate the brachial Augmentation Index (AI) and the Time Lag. The effects of variations in a number of model parameters on the AI and Time Lag are then investigated by simulating the model.

4.2 Simulation and Feature Extraction

The combined model discussed in Chapter 3 was used to simulate the brachial artery pressure and pneumatic cuff external wall strain contours as shown in figures 4.1 and 4.2 respectively. Average model parameters were adopted from the literature and used to simulate the contours for a young healthy male adult [46]. Also, an above systolic cuff pressure of 120 mmHg was used to simulate these plots.

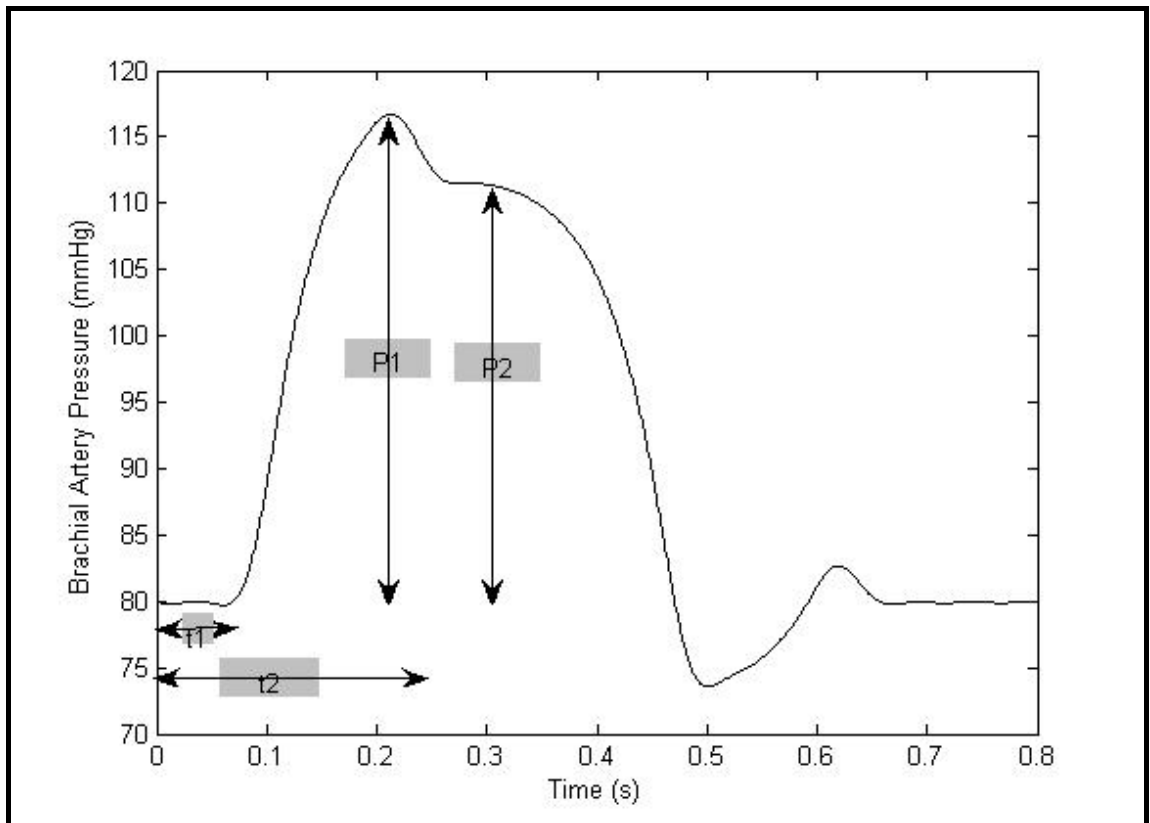


Figure 4.1: Simulated brachial artery pressure waveform for a healthy young adult. Arrows indicate the four feature points extracted (P1, P2, t1, t2).

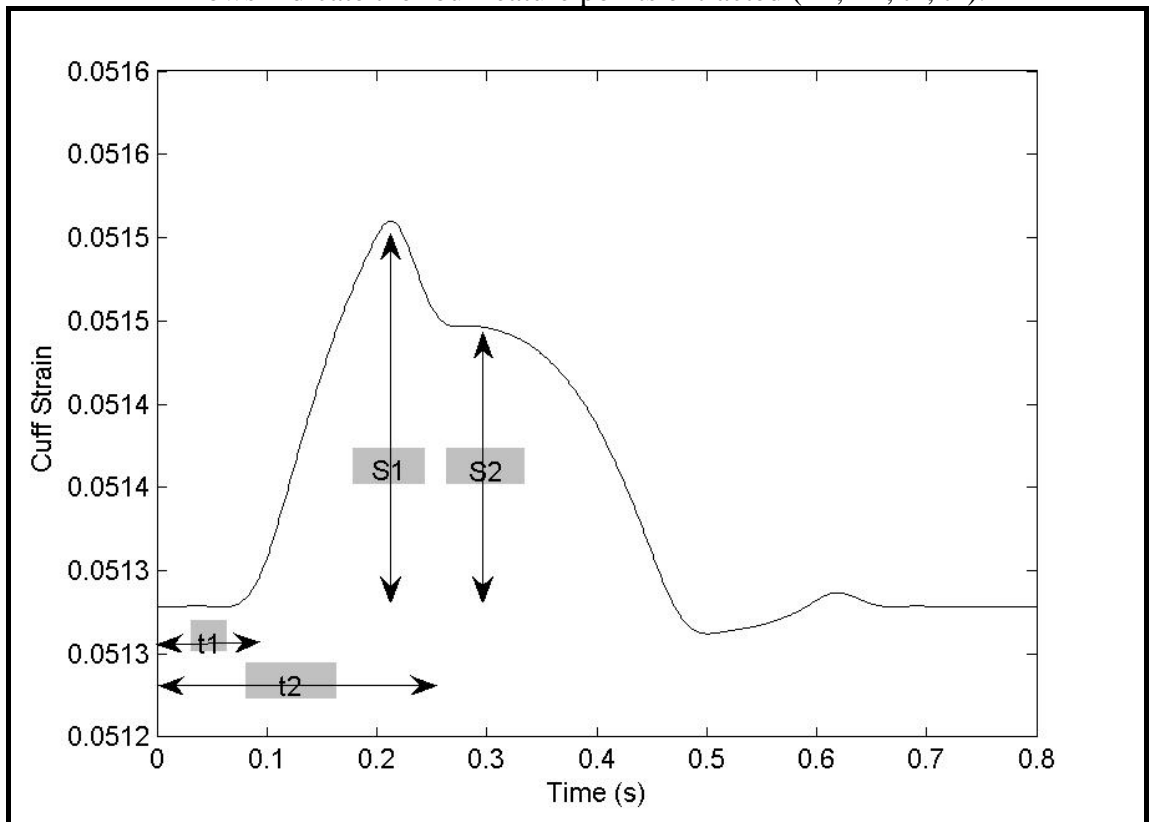


Figure 4.2: Simulated strain waveform on the pneumatic cuff outer wall for a healthy young adult. Arrows indicate the four feature points extracted (S1, S2, t1, t2).

Four feature points were extracted from the pressure contours. These feature points are the time duration before the deflection marking the arrival of the incident wave (t1), the

time duration before the deflection marking the arrival of the reflected wave (t_2), the peak of the first pressure deflection minus the diastolic pressure (P_1) and the peak of the second pressure deflection minus the diastolic pressure (P_2).

The same feature points were extracted from the strain contours where S_1 is the peak of the first strain deflection minus the strain at diastolic pressure and S_2 is the peak of the second strain deflection minus the strain at diastolic pressure.

These feature points were then used to calculate the brachial Augmentation Indices (AI_p , AI_s) and the Time Lag which are used as a measure of arterial stiffness. The brachial AI is not mentioned in the open literature due to the unavailability of non-invasive brachial blood pressure monitoring devices. On the other hand, the radial AI is widely used as an indicator for aortic stiffening where the radial pulse is obtained non-invasively using applanation tonometry. Also the aortic AI is widely used to predict aortic stiffening.

The brachial artery pressure AI (AI_p) can be written as:

$$AI_p = \frac{P_2}{P_1} \quad (4.1)$$

where the brachial artery strain AI (AI_s) can be written as:

$$AI_s = \frac{S_2}{S_1} \quad (4.2)$$

And the Time Lag is written as:

$$Time\ Lag = t_2 - t_1 \quad (4.3)$$

4.3 Effect of Artery Stiffness Variations

The effect of the stiffness of the aorta on the brachial artery pressure waveform and the strain on the external wall of the pneumatic cuff was investigated by simulating the combined model at different stiffness values and keeping all other parameters constant at their normal healthy level. A global stiffness increment was assumed in the simulation.

4.3.1 Brachial Artery Pressure

Figure 4.3 shows the brachial artery pressure waveforms at different aortic stiffnesses ranging from a healthy aortic stiffness (75%) to a diseased/aged aortic stiffness (400%) and keeping all other parameters constant. The four feature points were extracted from the figure to calculate the pressure AI (AI_p) and the Time Lag. These values are reported in table 4.1.

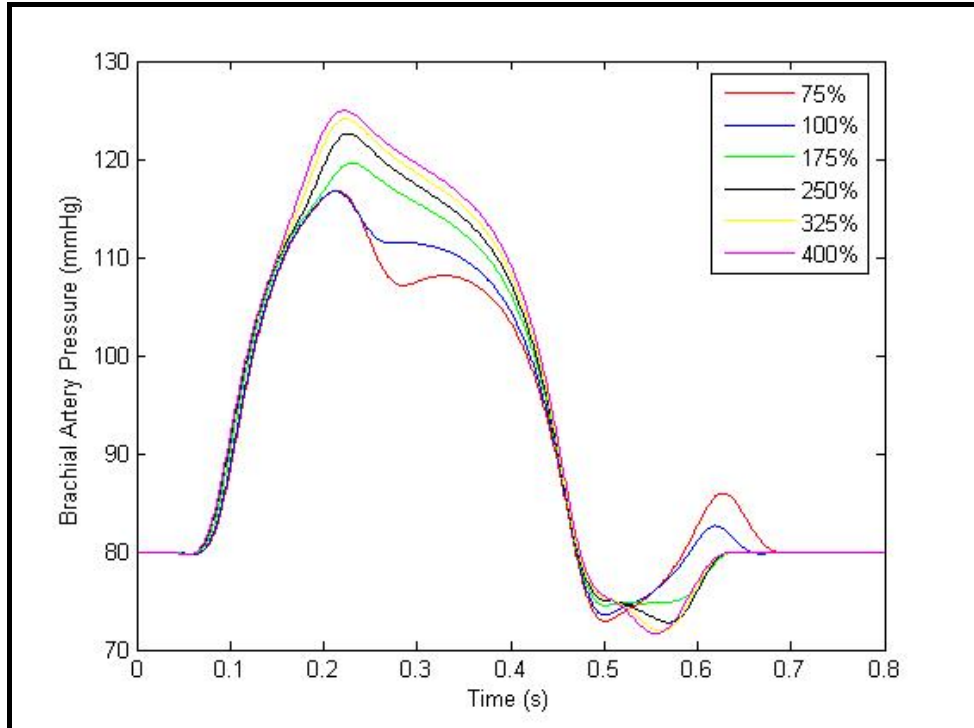


Figure 4.3: Brachial artery pressure waveforms at different aortic stiffness values ranging from healthy (75%) to diseased (400%).

Table 4.1: Table showing the effect of arterial stiffness on the feature points of the brachial artery pressure contours, (AI_p), and Time Lag.

Stiffness %	P1 mmHg	P2 mmHg	AI %	t1 (s)	t2 (s)	Time Lag (s)
75.0	116.8	108.1	76.36	0.076	0.282	0.206
87.5	116.8	109.9	81.25	0.075	0.27	0.195
100.0	116.8	111.5	85.60	0.074	0.265	0.191
112.5	116.8	113	89.67	0.074	0.261	0.187
125.0	116.8	114.3	93.21	0.074	0.235	0.161
137.5	116.8	117.3	101.36	0.074	0.22	0.146
150.0	116.10	118	105.26	0.072	0.197	0.125
162.5	115.5	119	109.86	0.072	0.191	0.119
175.0	115.3	119.6	112.18	0.072	0.189	0.117
187.5	114.2	120.3	117.84	0.071	0.179	0.108
200.0	114.1	120.8	119.65	0.071	0.178	0.107
212.5	114	121.5	122.06	0.071	0.177	0.106

225.0	113.8	121.7	123.37	0.07	0.175	0.105
237.5	113.5	122.3	126.27	0.069	0.172	0.103
250.0	113.1	122.6	128.70	0.069	0.169	0.1
262.5	113	123	130.30	0.069	0.168	0.099
275.0	112.7	123.3	132.42	0.069	0.166	0.097
300.0	112.3	123.6	134.98	0.069	0.163	0.094
325.0	111.8	124.1	138.68	0.069	0.159	0.09
350.0	111.3	124.5	142.17	0.069	0.156	0.087
375.0	110.9	124.8	144.98	0.069	0.154	0.085
400.0	110.5	124.9	147.21	0.069	0.152	0.083

4.3.2 Cuff Strain

Figure 4.4 shows the strain contours on the outer wall of the pneumatic cuff at different aortic stiffness ranging from a healthy aortic stiffness (75%) to a diseased/aged aortic stiffness (400%). The model was simulated at a cuff pressure of 120 mmHg while all other parameters were kept constant. The four feature points were extracted from the figure and the strain AI (AI_s) and the Time Lag were then calculated. These values are reported in table 4.2.

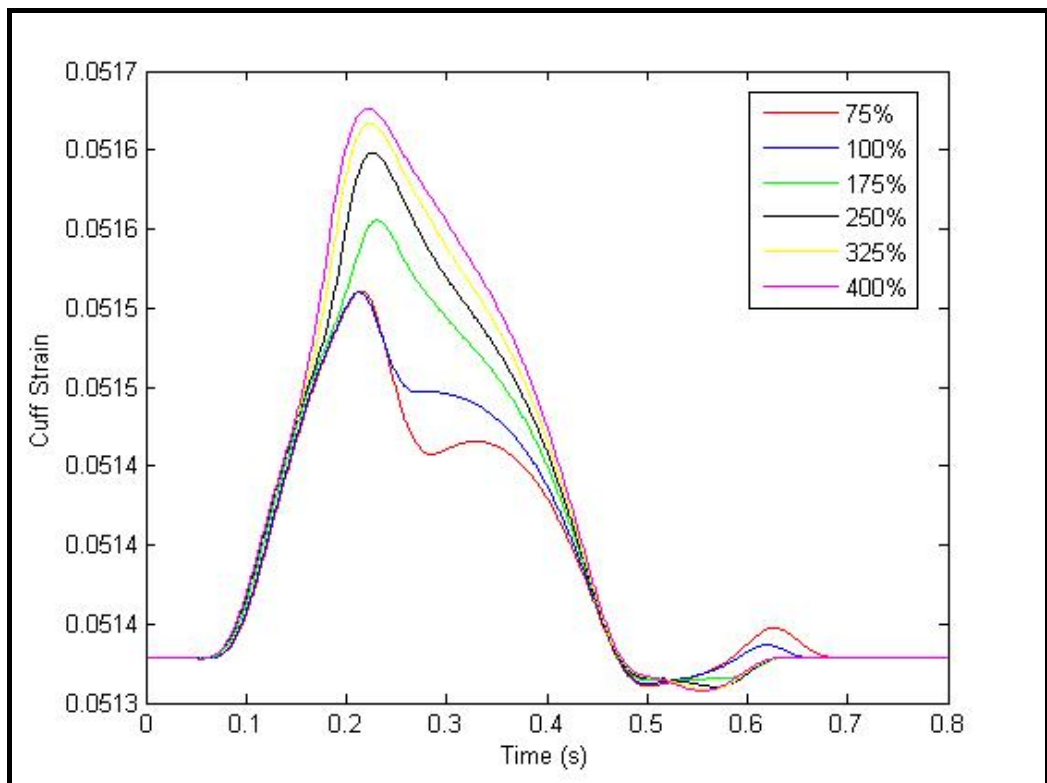


Figure 4.4: Strain on the pneumatic cuff outer wall contours at different aortic stiffness values ranging from healthy (75%) to diseased (400%).

4.4 Effect of Artery Radius Variations

The effect of the aortic radius on the brachial artery pressure waveform and the strain on the external wall of the pneumatic cuff was investigated by simulating the combined model at different aortic internal radii and keeping all other parameters constant at their normal healthy level. The aortic radius elevation was assumed to act globally across the entire aorta. Hence, each lump of the aorta was increased by the percentage shown. All other model parameters were kept constant

Table 4.2: The effect of arterial stiffness on the feature points of the pneumatic cuff strain contours, (AI_s) and Time Lag.

Stiffness%	S1	S2	AI%	t1 (s)	t2 (s)	Time Lag (s)
75	0.05156	0.05147	60.87	0.076	0.282	0.206
87	0.05156	0.05149	69.57	0.075	0.27	0.195
100	0.05156	0.0515	73.91	0.074	0.265	0.191
112	0.05156	0.05151	78.26	0.074	0.261	0.187
125	0.05156	0.05152	82.61	0.074	0.235	0.161
137	0.05156	0.051555	97.83	0.074	0.22	0.146
150	0.05156	0.05159	113.04	0.072	0.197	0.125
162	0.05154	0.05159	123.81	0.072	0.191	0.119
175	0.05154	0.05161	133.33	0.072	0.189	0.117
187	0.05153	0.05162	145.00	0.071	0.179	0.108
200	0.05153	0.05163	150.00	0.071	0.178	0.107
212	0.05152	0.05163	157.89	0.071	0.177	0.106
225	0.05152	0.05164	163.16	0.07	0.175	0.105
237	0.05152	0.05164	163.16	0.069	0.172	0.103
250	0.05151	0.05165	177.78	0.069	0.169	0.1
262	0.05151	0.05165	177.78	0.069	0.168	0.099
275	0.05151	0.05166	183.33	0.069	0.166	0.097
300	0.0515	0.05166	194.12	0.069	0.163	0.094
325	0.0515	0.05167	200.00	0.069	0.159	0.09
350	0.05149	0.05167	212.50	0.069	0.156	0.087
375	0.05149	0.05167	212.50	0.069	0.154	0.085
400	0.05149	0.05168	218.75	0.069	0.152	0.083

4.4.1 Brachial Artery Pressure

Figure 4.5 shows the brachial artery pressure waveforms at different internal radii ranging from a normal radius (100%) to an elevated aortic radius caused by

degeneration of the arteries (200%). The four feature points were extracted from the figure and the pressure AI (AI_p) and the Time Lag were then calculated. These values are reported in table 4.3.

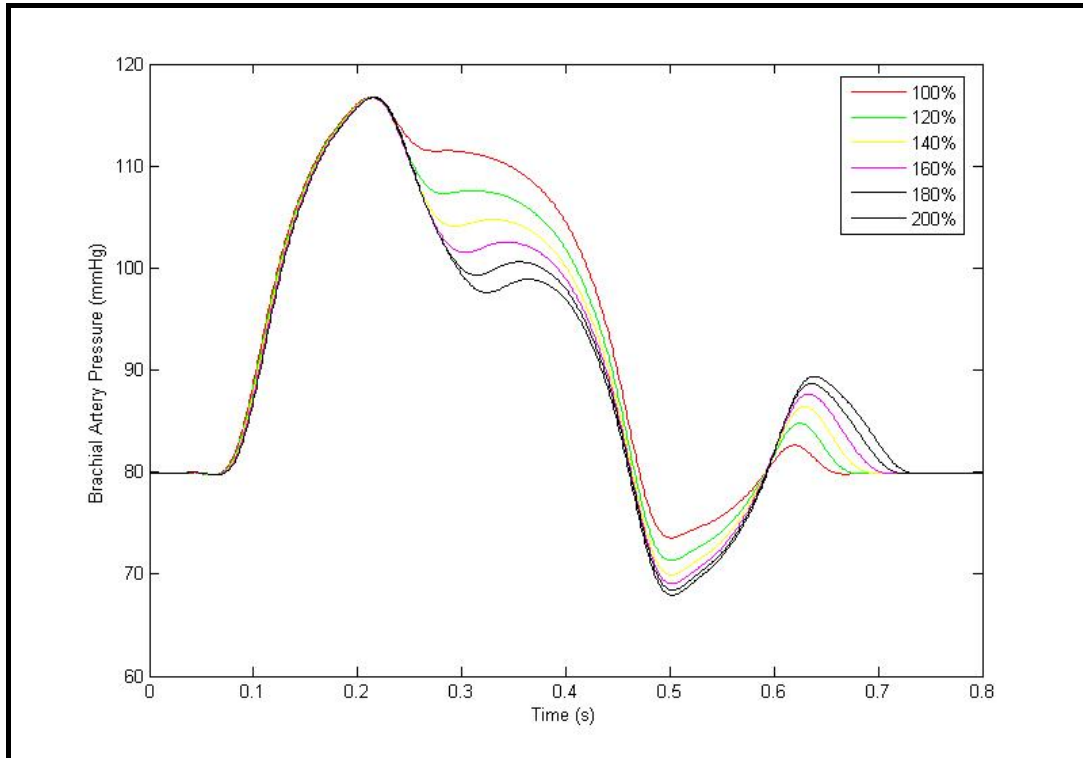


Figure 4.5: Brachial artery pressure waveforms at different aortic radius values ranging from normal (100%) to elevated (200%).

Table 4.3: The effect of aortic radius on the feature points of the brachial artery pressure contours, (AI_p) and Time Lag.

Radius %	P1 mmHg	P2 mmHg	AI%	t1 (s)	t2 (s)	Time Lag (s)
100	116.8	111.5	85.60	0.074	0.265	0.191
110	116.8	109.5	80.16	0.074	0.269	0.195
120	116.8	107.6	75.00	0.075	0.274	0.199
130	116.8	106.2	71.20	0.075	0.278	0.203
140	116.8	105.8	70.11	0.075	0.284	0.209
150	116.8	103.6	64.13	0.075	0.289	0.214
160	116.8	102.5	61.14	0.075	0.3	0.225
170	116.8	101.6	58.70	0.075	0.305	0.23
180	116.8	100.6	55.98	0.075	0.309	0.234
190	116.8	99.76	53.70	0.075	0.32	0.245
200	116.8	98.88	51.30	0.075	0.321	0.246

4.4.2 Cuff Strain

Figure 4.6 shows the strain contours on the outer wall of the pneumatic cuff at different aortic radii ranging from a normal radius (100%) to an elevated aortic radius (200%). The four feature points were extracted from the figure and the pressure AI (AI_s) and the Time Lag were then calculated. These values are reported in table 4.4.

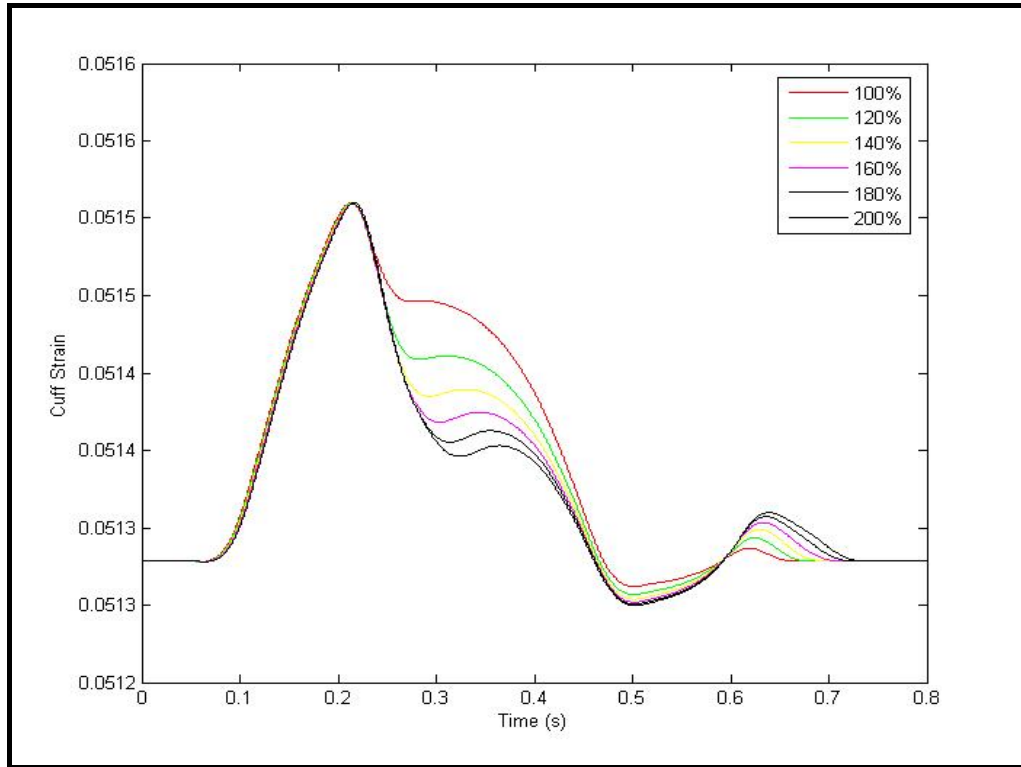


Figure 4.6: Strain on the pneumatic cuff outer wall contours at different aortic radii ranging from healthy (75%) to diseased (200%).

Table 4.4: The effect of the radius of the aorta on the feature points of the pneumatic cuff strain contours, (AI_s) and Time Lag.

Radius%	S1	S2	AI%	t1 (s)	t2 (s)	Time Lag (s)
100	0.05156	0.0515	73.91	0.074	0.265	0.191
110	0.05156	0.051478	64.35	0.074	0.269	0.195
120	0.05156	0.05146	56.52	0.075	0.274	0.199
130	0.05156	0.05145	52.17	0.075	0.278	0.203
140	0.05156	0.05144	47.83	0.075	0.284	0.209
150	0.05156	0.05143	43.48	0.075	0.289	0.214
160	0.05156	0.05142	39.13	0.075	0.3	0.225
170	0.05156	0.051417	37.83	0.075	0.305	0.23
180	0.05156	0.051413	36.09	0.075	0.309	0.234
190	0.05156	0.05141	34.78	0.075	0.32	0.245
200	0.05156	0.0514	30.43	0.075	0.321	0.246

4.5 Effect of Aortic Thickness Variations

The effect of the global thickness of aorta on the brachial artery pressure waveforms and the strain contours of the pneumatic cuff outer wall was investigated by simulating the combined model at different aortic thicknesses while keeping all other model parameters constant. The aortic thickness elevation was also assumed to act globally across the entire aorta.

4.5.1 Brachial Artery Pressure

Figure 4.7 shows the brachial artery pressure waveforms at different aortic thicknesses ranging from a normal thickness (100%) to an elevated thickness (200%). The four feature points were extracted from the figure and the pressure AI (AI_p) and the Time Lag were then calculated. These values are reported in table 4.5.

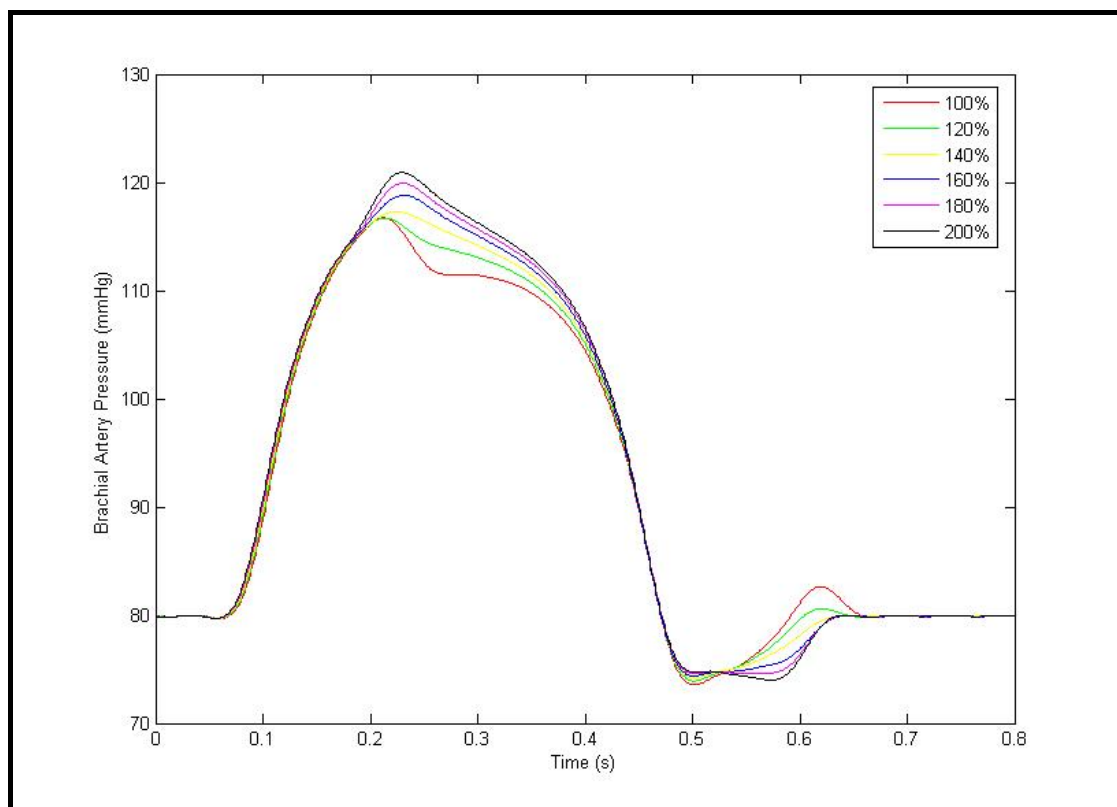


Figure 4.7: Brachial artery pressure waveforms at different aortic thicknesses ranging from healthy (100%) to diseased (200%).

4.5.2 Cuff Strain

Figure 4.8 shows the strain contours on the outer wall of the pneumatic cuff at different aortic thicknesses ranging from normal thickness (100%) to an elevated aortic thickness

(200%). The four feature points were extracted from the figure and the pressure AI (AI_p) and the Time Lag were then calculated. These values are reported in Table 4.6.

Table 4.5: The effect of aortic thickness on the feature points of the brachial artery pressure waveforms, (AI_p) and Time Lag.

Thickness%	P1 mmHg	P2 mmHg	AI%	t1 (s)	t2 (s)	Time Lag (s)
100	116.8	111.5	85.60	0.074	0.265	0.191
110	116.8	113	89.67	0.074	0.258	0.184
120	116.8	114.2	92.93	0.074	0.249	0.175
130	116.8	116.5	99.18	0.074	0.231	0.157
140	116.8	117.3	101.36	0.074	0.219	0.145
150	116.6	118	103.83	0.074	0.207	0.133
160	116.2	118.8	107.18	0.074	0.197	0.123
170	116	119.5	109.72	0.074	0.195	0.121
180	115.4	119.9	112.71	0.074	0.189	0.115
190	115.3	120.4	114.45	0.075	0.187	0.112
200	115.2	120.9	116.19	0.075	0.186	0.111

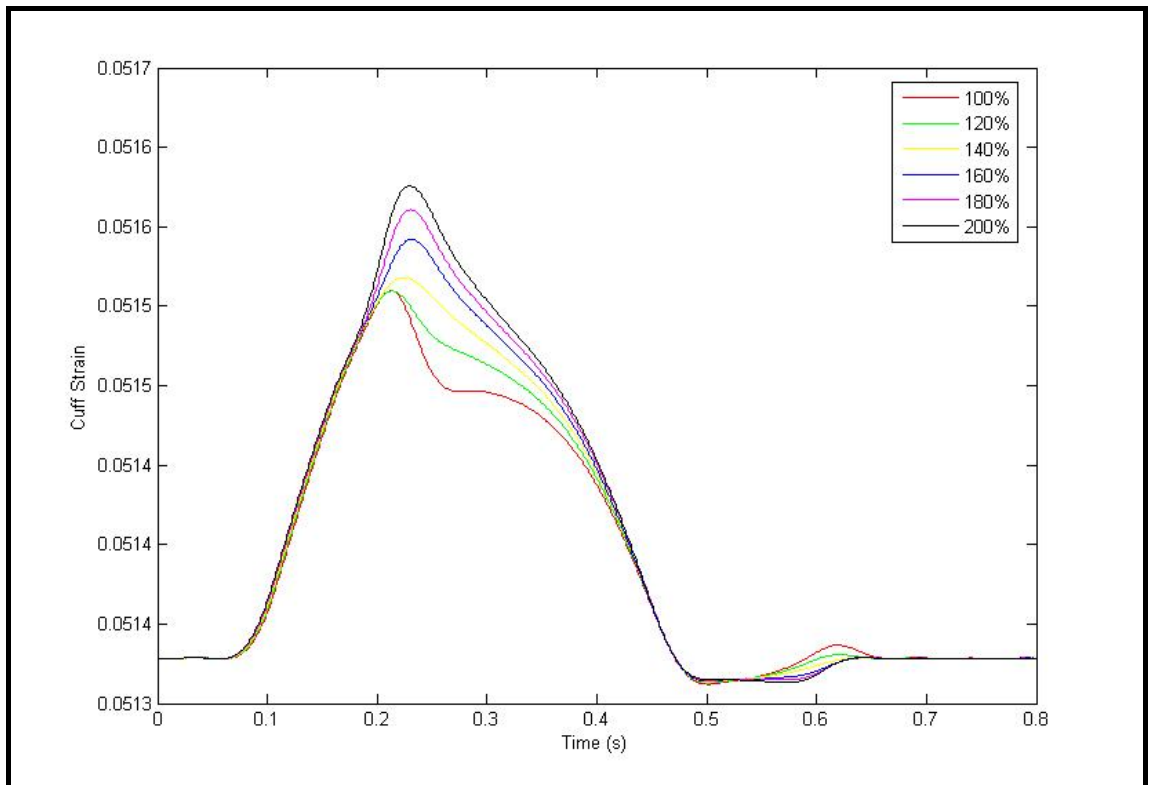


Figure 4.8: Pneumatic cuff outer wall strain contours at different aortic thicknesses ranging from healthy (100%) to diseased (200%).

Table 4.6: The effect of aortic thickness on the feature points of the strain contours on the cuff outer wall, (AI_s) and Time Lag.

Thickness%	S1	S2	AI%	t1(s)	t2(s)	Time Lag (s)
100	0.05156	0.0515	73.91	0.074	0.265	0.191
110	0.05156	0.051515	80.43	0.074	0.258	0.184
120	0.05156	0.051525	84.78	0.074	0.249	0.175
130	0.05156	0.051556	98.26	0.074	0.231	0.157
140	0.051553	0.05157	107.62	0.074	0.219	0.145
150	0.05155	0.05158	113.64	0.074	0.207	0.133
160	0.051546	0.05159	120.37	0.074	0.197	0.123
170	0.05154	0.0516	128.57	0.074	0.195	0.121
180	0.051537	0.05161	135.27	0.074	0.189	0.115
190	0.051533	0.05162	142.86	0.075	0.187	0.112
200	0.05153	0.05163	150.00	0.075	0.186	0.111

4.6 Effect of Heart Rate

The effect of heart rate on the brachial artery pressure and the strain on the cuff outer wall was investigated by simulating the combined model at different heart rates and keeping all other model parameters constant. The heart rate was assumed to affect both the diastole and systole time periods equally.

4.6.1 Brachial Artery Pressure

Figure 4.9 shows the brachial artery pressure contours at a range of simulated heart rates ranging from 75 b/m to 120 b/m. This figure was then used to extract the four feature points and calculate the pressure AI (AI_p) and the Time Lag which are listed in Table 4.7.

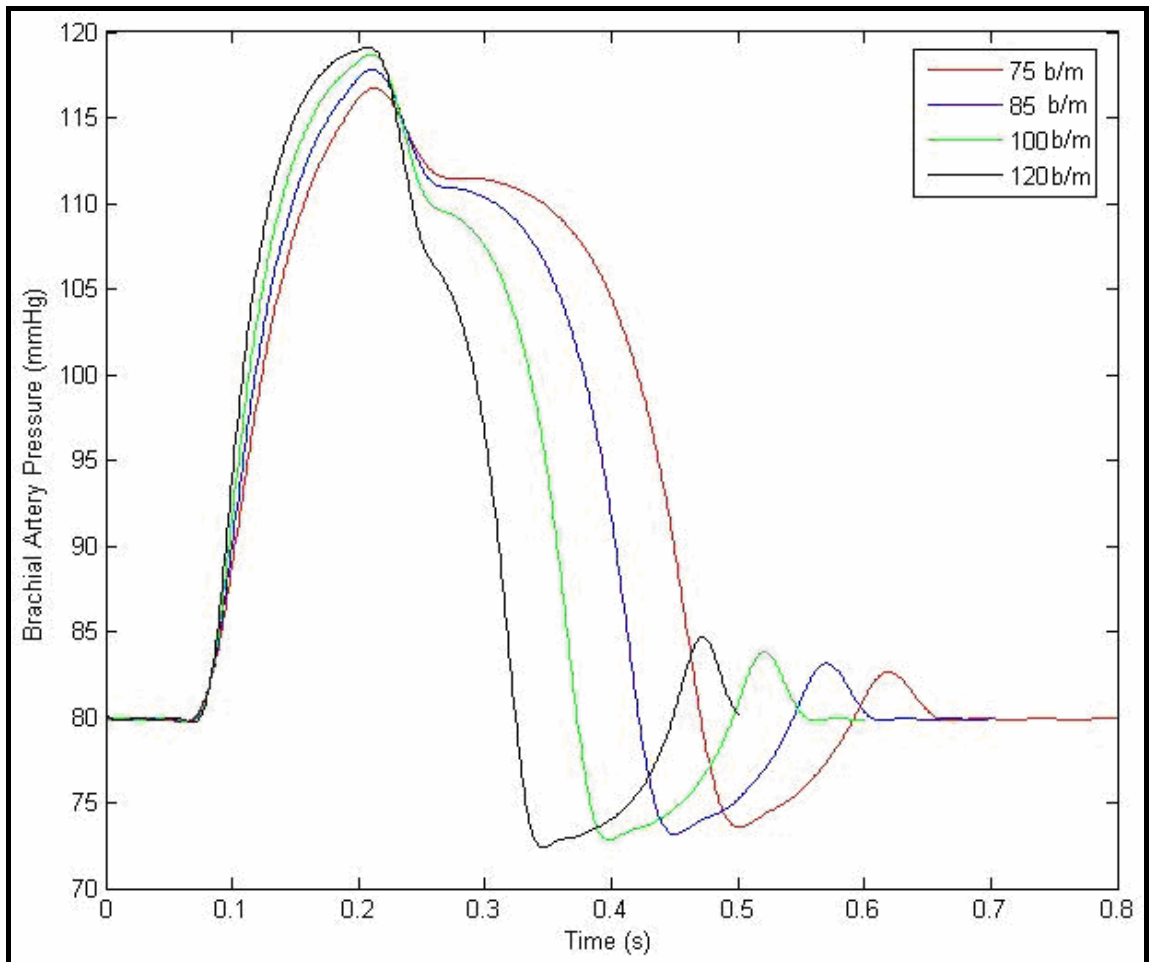


Figure 4.9: Brachial artery pressure simulation at different heart rates ranging from 75 b/m to 120 b/m.

Table 4.7: The effect of heart rate on the brachial artery pressure feature points, (AI_p), and Time Lag.

Heart Rate (b/m)	P1 mmHg	P2 mmHg	AI_p	t1(s)	t2(s)	Time Lag (s)
75	116.7	111.4	85.56	0.074	0.265	0.191
85	117.8	110.7	81.22	0.074	0.265	0.191
100	118.7	109.1	75.19	0.074	0.265	0.191
120	119.1	105.4	64.96	0.074	0.265	0.191

4.6.2 Cuff Strain

Figure 4.10 shows the strain contour on the pneumatic cuff outer wall at a number of simulated heart rates ranging from 75 b/m to 120 b/m. The four feature points were extracted from the figure and the strain AI (AI_s) and the Time Lag were then calculated. These values are reported in table 4.8.

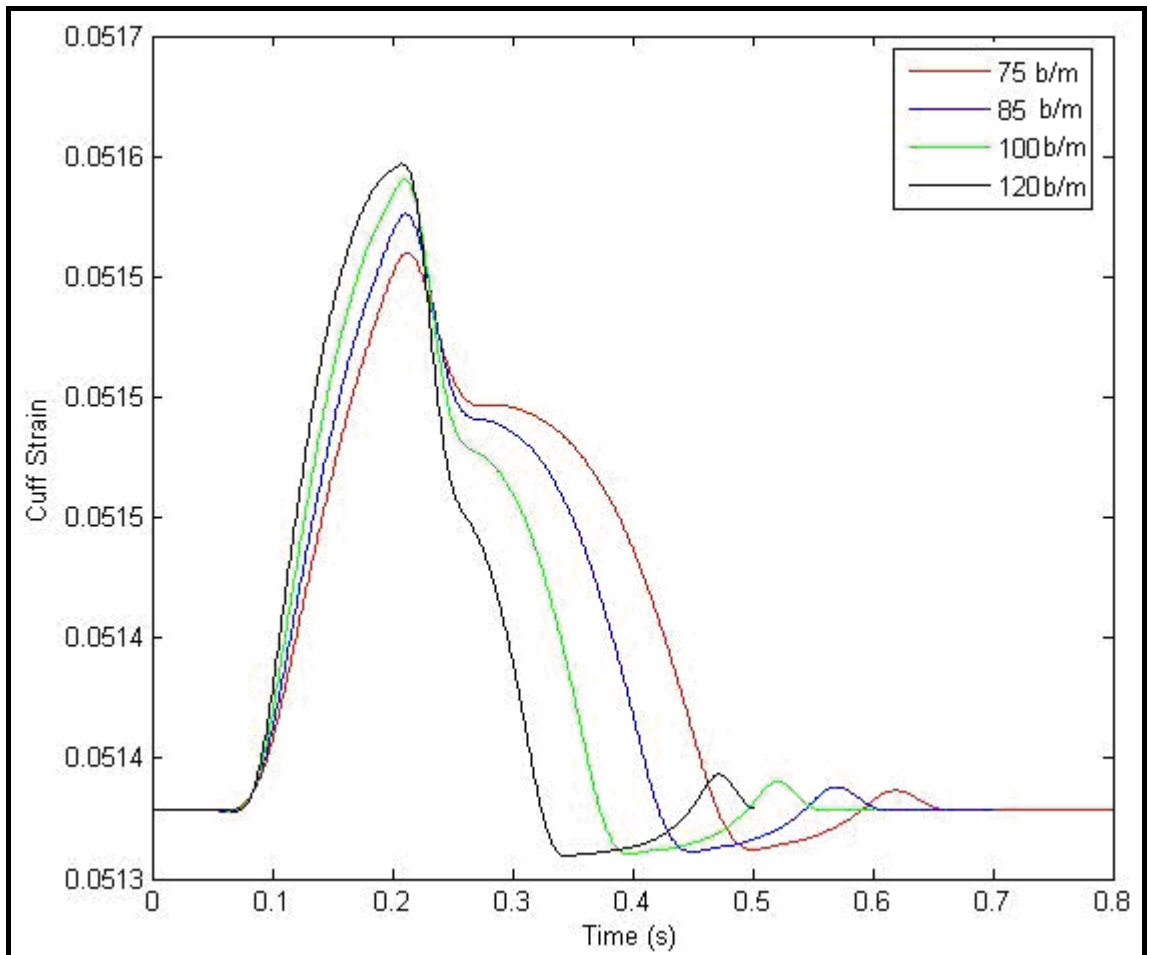


Figure 4.10: Strain contour on the pneumatic cuff outer wall at a number of heart rates ranging from 75 b/m to 120 b/m.

Table 4.8: The effect of heart rate on the feature points in the strain contours of the pneumatic cuff outer wall, (AI_s) and Time Lag.

Heart Rate (b/m)	S1	S2	AI%	t1(s)	t2(s)	Time Lag (s)
75	0.05156	0.0515	73.91	0.074	0.265	0.191
85	0.05158	0.05149	64.00	0.074	0.265	0.191
100	0.05159	0.05148	57.69	0.074	0.265	0.191
120	0.0516	0.05145	44.44	0.074	0.265	0.191

4.7 Effect of Cuff Pressure

The effect of cuff pressure on the brachial artery pressure waveform and the strain contour on the cuff outer wall is investigated by simulating the combined model at different cuff pressures. All other model parameters were kept constant to a normal value.

4.7.1 Brachial Artery Pressure

Figure 4.11 shows the brachial artery pressure contours at a range of cuff pressures ranging from 90 mmHg to a significantly high cuff pressure of 175 mmHg. This figure was then used to extract the four feature points; the Augmentation Index and the Time Lag were then calculated. These values are listed in table 4.9.

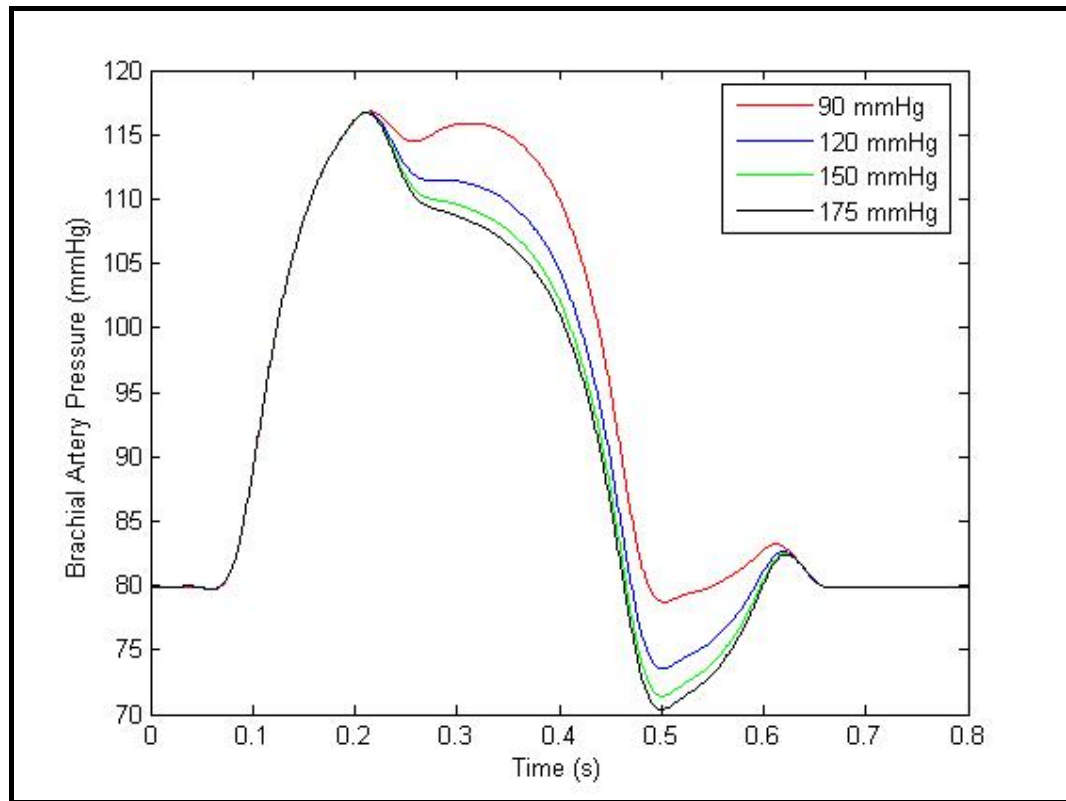


Figure 4.11: Brachial artery pressure simulation at a number of cuff pressures ranging from 90 mmHg to 170 mmHg.

Table 4.9: The effect of cuff pressure on the brachial artery pressure feature points, (AI_p) and Time Lag.

Pressure mmHg	P1 mmHg	P2 mmHg	AI%	t1 (s)	t2 (s)	Time Lag (s)
120	116.8	111.5	85.60	0.074	0.265	0.191
125	116.8	111.1	84.51	0.074	0.265	0.191
130	116.8	110.8	83.70	0.074	0.265	0.191
135	116.8	110.5	82.88	0.074	0.265	0.191
140	116.8	110.3	82.34	0.074	0.265	0.191
145	116.8	110.1	81.79	0.074	0.265	0.191
150	116.8	109.8	80.98	0.074	0.265	0.191
155	116.8	109.6	80.43	0.074	0.265	0.191
160	116.8	109.5	80.16	0.074	0.265	0.191
165	116.8	109.3	79.62	0.074	0.265	0.191
170	116.8	109.1	79.08	0.074	0.265	0.191
175	116.8	109	78.80	0.074	0.265	0.191

4.7.2 Cuff Strain

Figure 4.12 shows the strain contours on the pneumatic cuff outer wall at a range of cuff pressures ranging from 90 mmHg to a significantly high cuff pressure of 170 mmHg. This figure was then used to extract the four feature points; the strain AI (AI_s) and the Time Lag were then calculated and are listed in table 4.10.

Table 4.10: The effect of cuff pressure on strain contours on the pneumatic cuff outer wall feature points, (AI_s) and Time Lag

Pressure mmHg	S1	S2	AI%	t1 (s)	t2 (s)	Time Lag (s)
120	0.05156	0.0515	73.91	0.074	0.265	0.191
125	0.053	0.05295	73.68	0.074	0.265	0.191
130	0.05442	0.05438	73.33	0.074	0.265	0.191
135	0.05582	0.05578	69.23	0.074	0.265	0.191
140	0.05719	0.05716	72.73	0.074	0.265	0.191
145	0.058543	0.05852	75.27	0.074	0.265	0.191
150	0.05987	0.05985	75.90	0.074	0.265	0.191
155	0.061175	0.061153	70.67	0.074	0.265	0.191
160	0.06245	0.06243	71.43	0.074	0.265	0.191
165	0.06379	0.06369	76.50	0.074	0.265	0.191
170	0.064936	0.064923	75.93	0.074	0.265	0.191
175	0.06615	0.066136	72.00	0.074	0.265	0.191

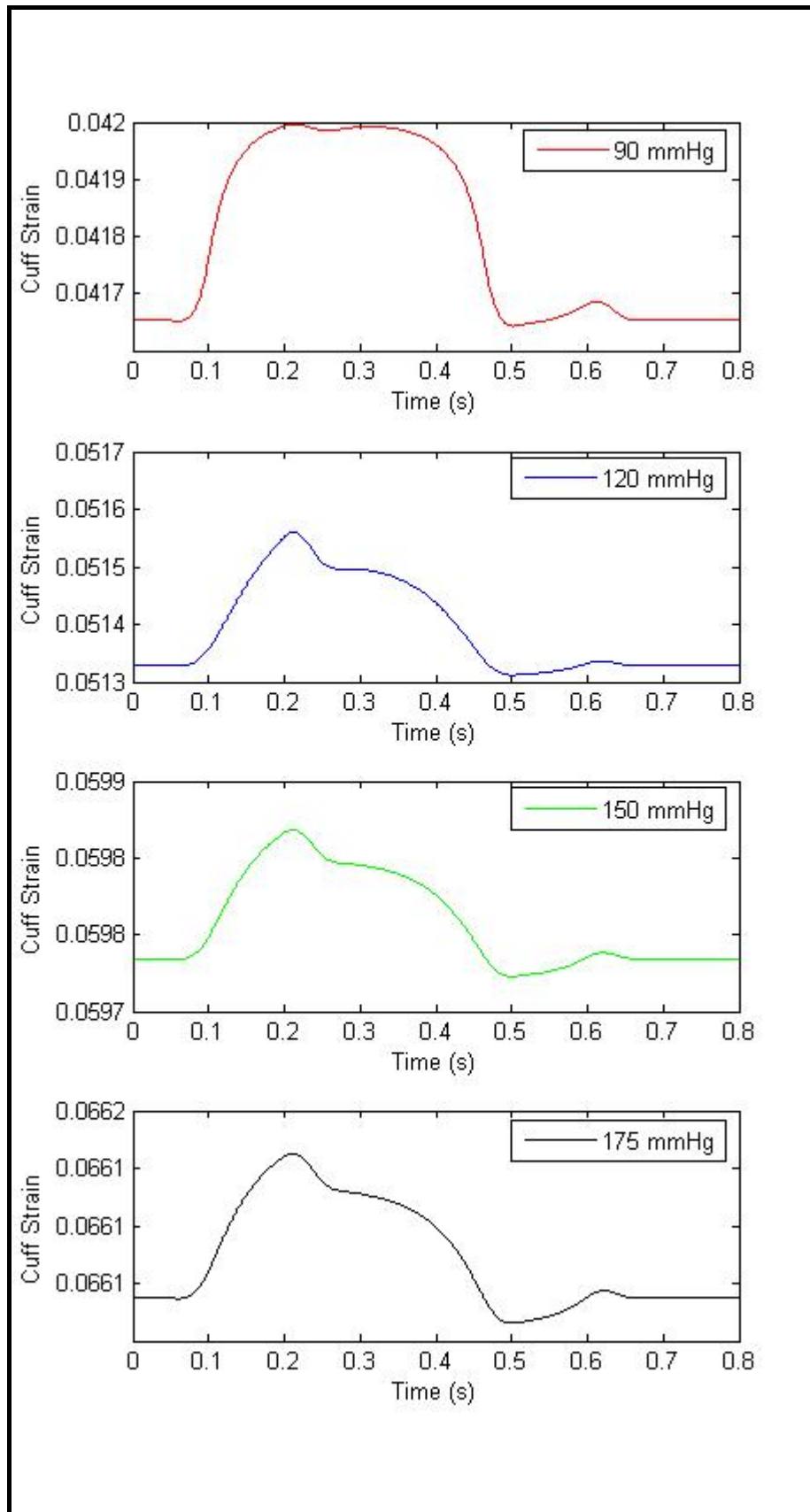


Figure 4.12: Strain contours on the pneumatic cuff outer wall at a number of cuff pressures ranging from 90 mmHg to 170 mmHg.

4.8 Closure

The combined model was used to simulate the brachial artery pressure waveforms and strain contours on the pneumatic cuff outer wall. A number of feature points and widely used indicators were defined to allow for the analysis of these waves. The model sensitivity to variations of important parameters was then investigated by changing one parameter at a time and observing the changes in the waveforms feature points and indicators.

These results will be discussed in more detail in Chapter 5. The validity of these results will be examined by comparing them with clinical data where available. Also the implications of these results on the suitability of this model for arterial stiffness assessment will be discussed.

Chapter 5 Discussion and Conclusions

5.1 Introduction

The simulation results given in Chapter 3 and 4 are discussed in more detail in this chapter. The model results are compared with the results obtained from the Pulsecor WEP monitor and experimental work and independent conclusions are drawn. The significance of the model developed in this work and the fact that it can be used to investigate the effect of variations in a number of cardiovascular, arm and cuff parameters, is also discussed. Finally a summary of the thesis and a recommendation for some future work are also given.

5.2 Discussion of Results

5.2.1 Brachial Artery Contours

The brachial artery pressure and cuff strain contours obtained by simulating the combined model are shown in figures 4.1 and 4.2 respectively. The pressure contour obtained from the model has the same shape and contains all the feature points found in invasively measured brachial artery contours reported in the literature as shown in figure 5.1 [3, 48]. In both our model and invasive data, the reflected pressure wave arrives to the brachial artery in diastole in healthy subjects.

It is important to note that there is no reflection at the measurement site in invasive measurements since there is no cuff occlusion. However there is a significant reflection that comes from the resistive vessels of the hand in invasive measurements [3]. This reflection was not taken into account in this model since it was assumed that the occlusion caused by supra-systolic cuff pressure prevents the transmission of pressure beyond the occlusion. The validity of this assumption becomes questionable as the cuff pressure is reduced because more pressure will be transmitted beyond the cuff where the reflection from the hand vessels becomes significant.

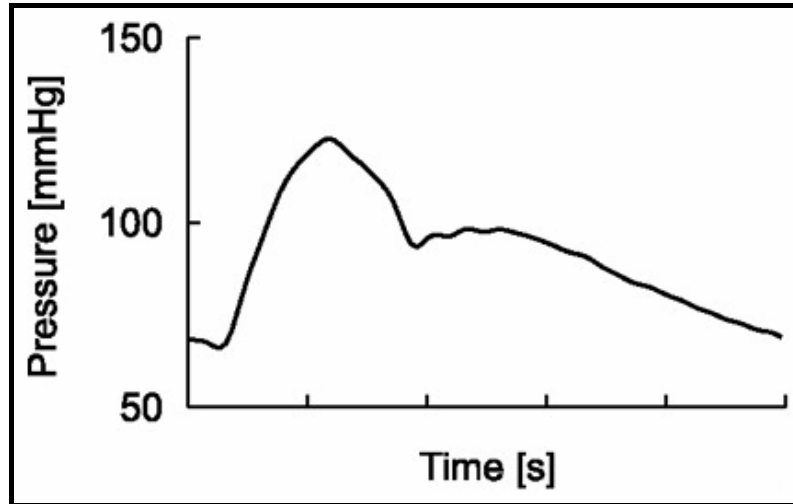


Figure 5.1: Brachial artery pressure pulse for healthy young subject [48].

The cuff strain contour shown in figure 4.2 appears to be very similar to the brachial pressure contour shown in figure 4.1. However, if a closer look is taken, it is clear that the relative amplitude between the first and second peaks is different. It appears that the first peak is amplified while the second peak is diminished when compared with the pressure contour as can be seen in figure 5.2.

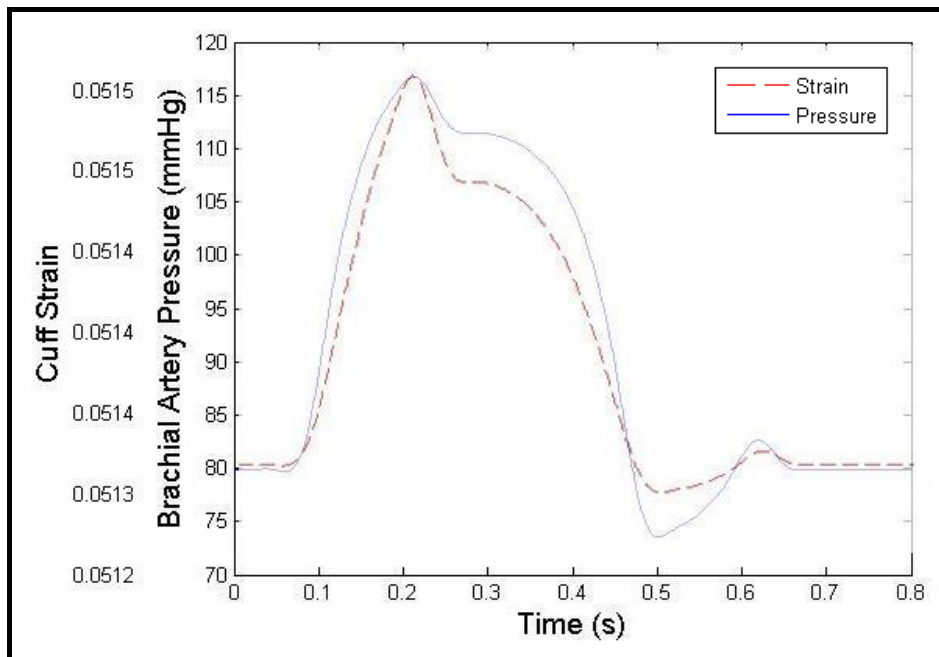


Figure 5.2: Pressure and strain contours simulated by the model for normal healthy adult input parameters.

The change can be explained by reviewing the brachial hemodynamics model described in Chapter 2. Figure 5.3 shows the relationship between the compliance of the brachial artery versus the transmural pressure as simulated by the model. This relationship was

also confirmed by experimental studies conducted by Linden and Drzewiecki as shown in figure 5.4 [49]. Figure 5.3 shows that the artery compliance is highest at zero transmural pressure. There is a very small change in the compliance of the brachial artery with age therefore this relationship should not be affected with aging or central arterial stiffening [3].

The simulation was performed at a cuff pressure of 120 mmHg while the brachial artery pressure pulsated from 80 mmHg to 118 mmHg. Hence, the higher the brachial artery pressure, the closer the transmural pressure is to zero, resulting in a more compliant brachial artery. This leads to more change in the artery area for a given pressure change and hence more soft tissue deformation. The increase in soft tissue deformation increases the cuff inner wall deformation which in turn increases the cuff pressure fluctuations. The increase in cuff pressure fluctuation results in an increase in the outer wall deformation and strain.

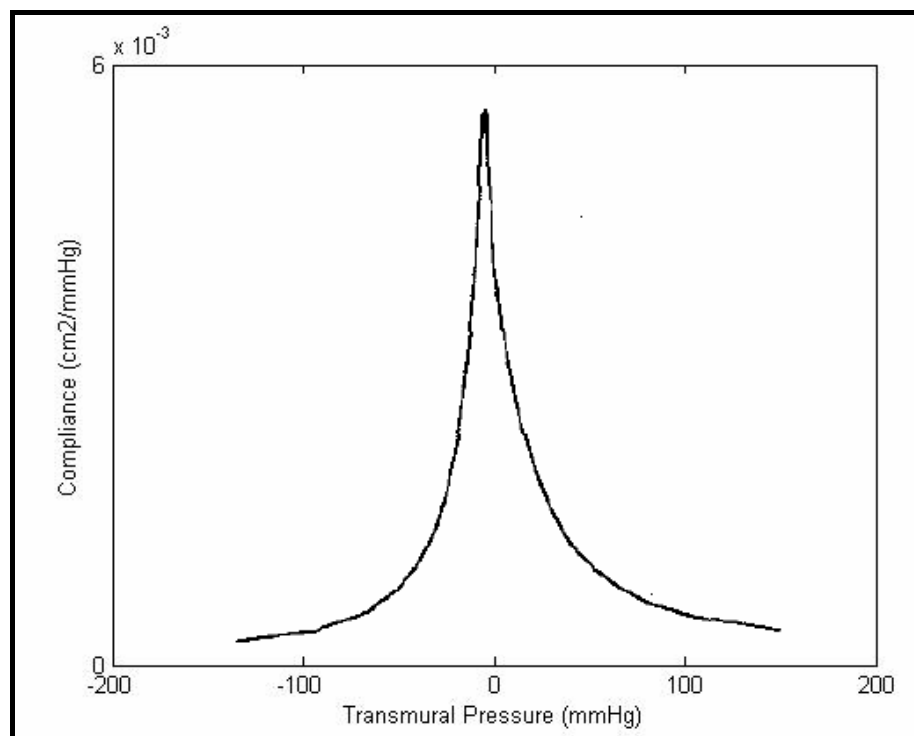


Figure 5.3: The compliance of the brachial artery versus transmural pressure.

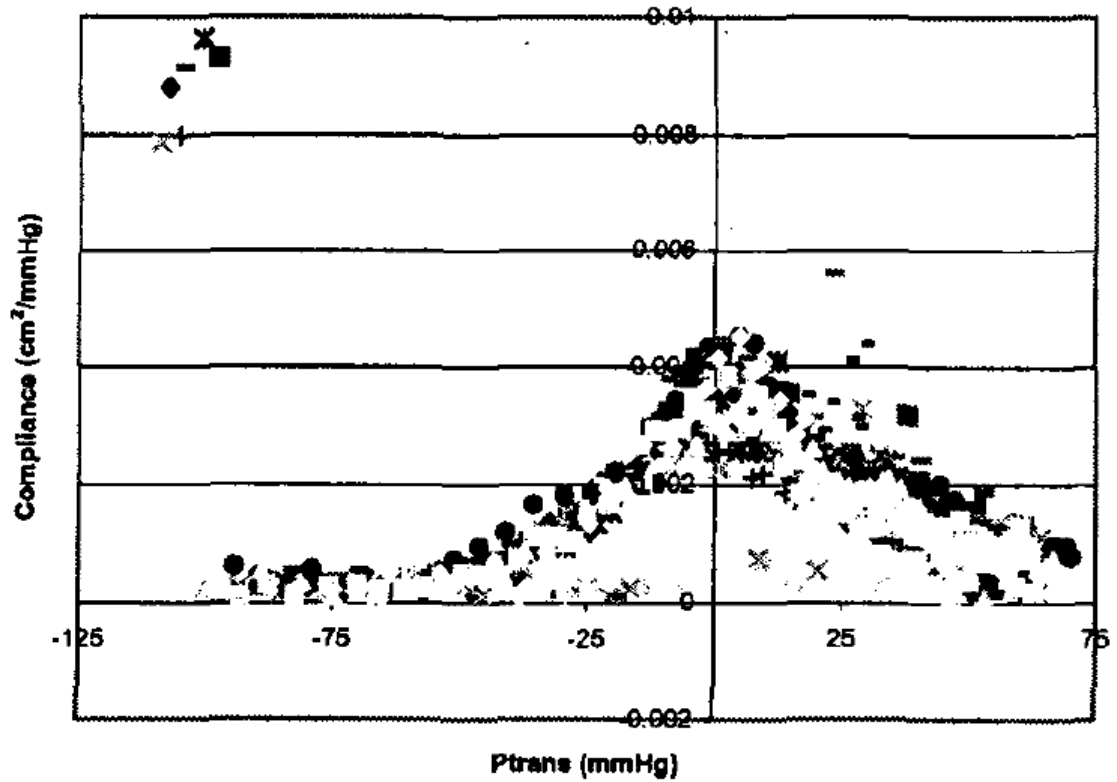


Figure 5.4: The compliance of the brachial artery versus the transmural pressure (Experimental). [49]

Recent experimental studies to measure the change in cross-sectional area of the brachial artery under a pressure cuff was conducted by Bank et al [50] as shown in figure 5.5.

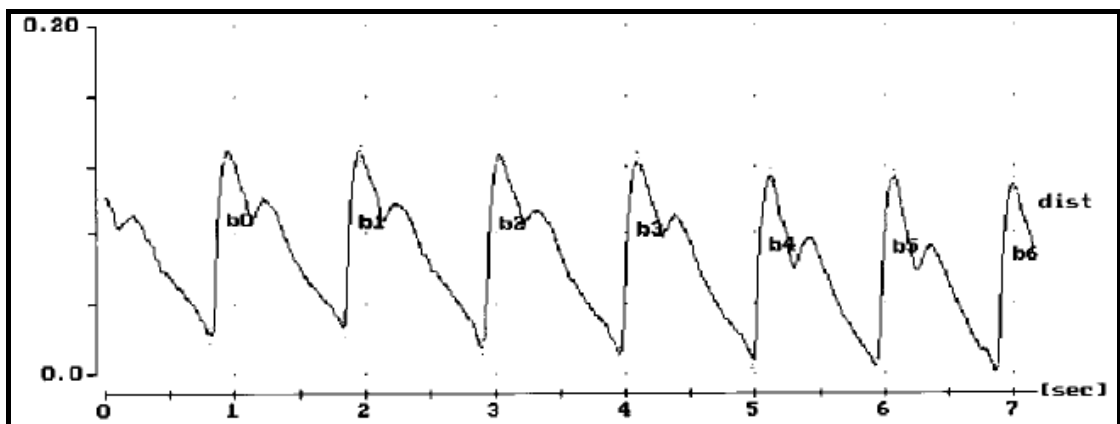


Figure 5.5: Brachial artery cross-sectional area under a pressure cuff versus time for a healthy adult male [50].

According to the combined model developed in this work, the strain contour on the cuff external wall has the same shape as the brachial artery cross-sectional area variations. Hence, figure 5.5 can be used to verify the shape of the strain contours obtained from the model. A comparison of figure 4.2 with figure 5.5 shows that the shape of the

contours is reasonably similar. In both figures, the reflected wave arrives at the brachial artery after around 0.2 seconds which shows that the acoustic model used in this work is adequate in predicting the propagation velocity of the pressure waves in the cardiovascular system.

The AI from the model simulation and experimental results are in close agreement at around 80%. The only noticeable difference between the two contours is that the simulated contour goes back to the diastolic level immediately while the measured contour slowly settles down. This can be attributed to the fact that the model does not consider secondary wave reflections that come later in diastole.

5.2.2 Effect of Aortic Stiffness Variations

Recent in-vivo human studies by Pearson et al [51] and other published research [3] confirm that aortic stiffness increases by an average of 300% in humans between the ages of 10 to 80 years. The effects of variations in aortic stiffness on the AI of the brachial artery pressure waveforms and the strain contours on the pneumatic cuff outer wall are shown graphically in figure 5.6.

The figure shows a prediction that an increase in aortic stiffness results in an increase in both the brachial pressure and strain augmentation indices. The pressure AI increased from 76% at 75% of the normal aortic stiffness for a young healthy adult male to 147% at 400% of the normal aortic stiffness while the strain AI increased from 61% to 218%.

The increase in pressure augmentation is caused by the increase in propagation velocity of the pressure waves in the aorta due to the increased stiffness which causes the reflected wave from the lower body to return to the brachial artery early where it augments with the incident wave. This can also be seen from the decreased time lag between the upstroke of the incident wave and the arrival of the reflected wave from 0.206 seconds to 0.083 seconds as shown in figure 5.7.

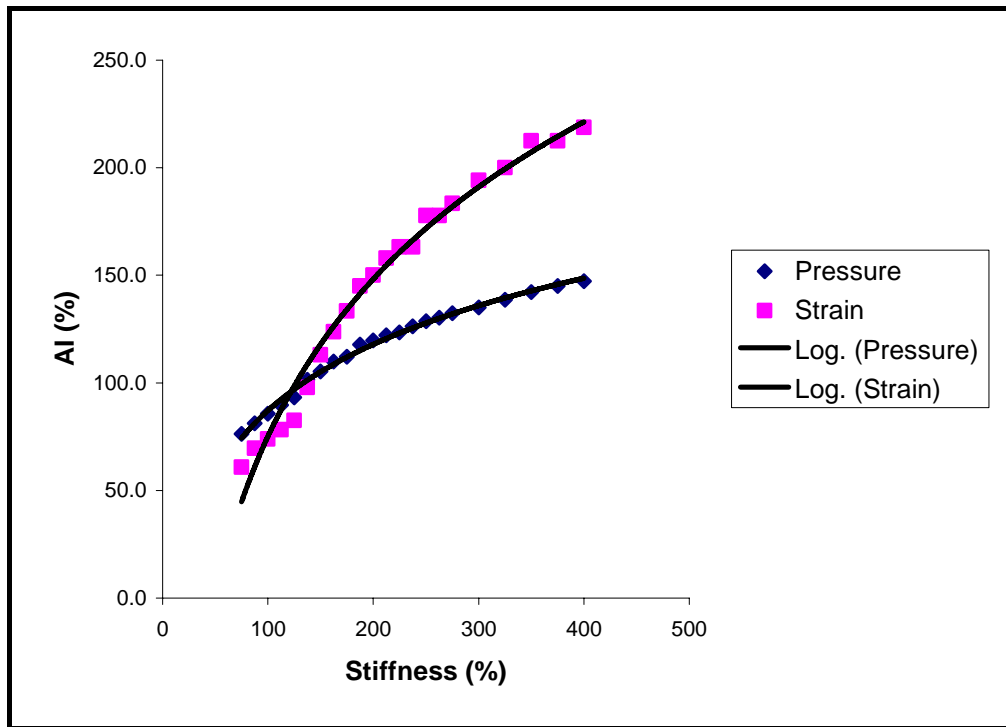


Figure 5.6: The effect of variations in aortic stiffness on the brachial Augmentation Index.

It is evident from figure 5.6 that the strain AI (AI_s) is less than the pressure AI (AI_p) for indices less than 100%. The reason for this is that the incident wave peak is higher than the reflected wave peak and hence the transmural pressure is closer to zero where more arterial and cuff deflection is caused as explained in Section 5.2.1.

On the other hand, when the AI exceeds 100%, the reflected wave peak is higher than the incident wave peak and hence causes more strain in the brachial artery and cuff outer wall which causes more augmentation in the strain contour and increases the strain AI (AI_s).

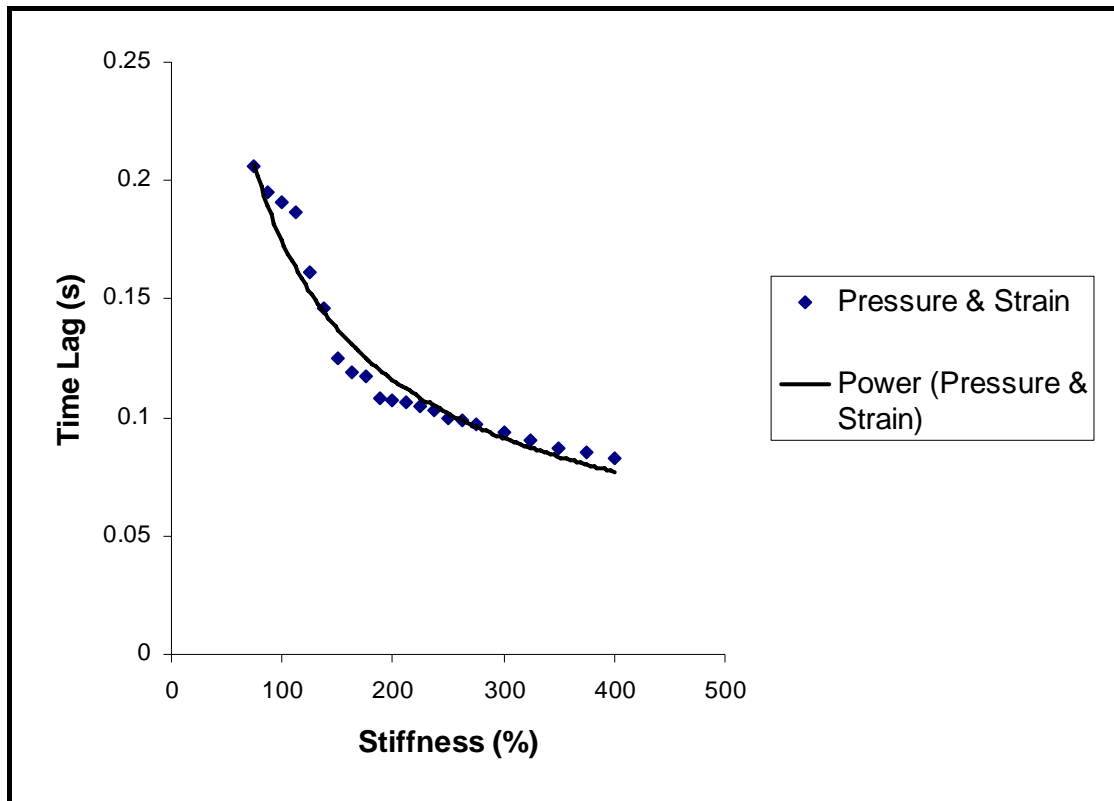


Figure 5.7: The effect of variations in aortic stiffness on the time lag of the arrival of the reflected wave in both the pressure and strain contours.

5.2.3 Effect of Aortic Radius Variations

In vivo studies conducted by Pearson et al [51] show that the radius of the aorta increases by an average of 100% in human subjects from the age of 10 to 80 years. Figure 5.8 shows the relationship between aortic radius and the pressure and cuff strain augmentation indices. The pressure AI (AI_p) decreased from 86% at normal aortic radius to 51% at 200% aortic stiffness while the cuff strain AI (AI_s) decreased from 74% at normal aortic radius to 30% at 200% the normal aortic radius. This is due to the decrease in the pressure wave propagation velocity as the radius of the aorta increases.

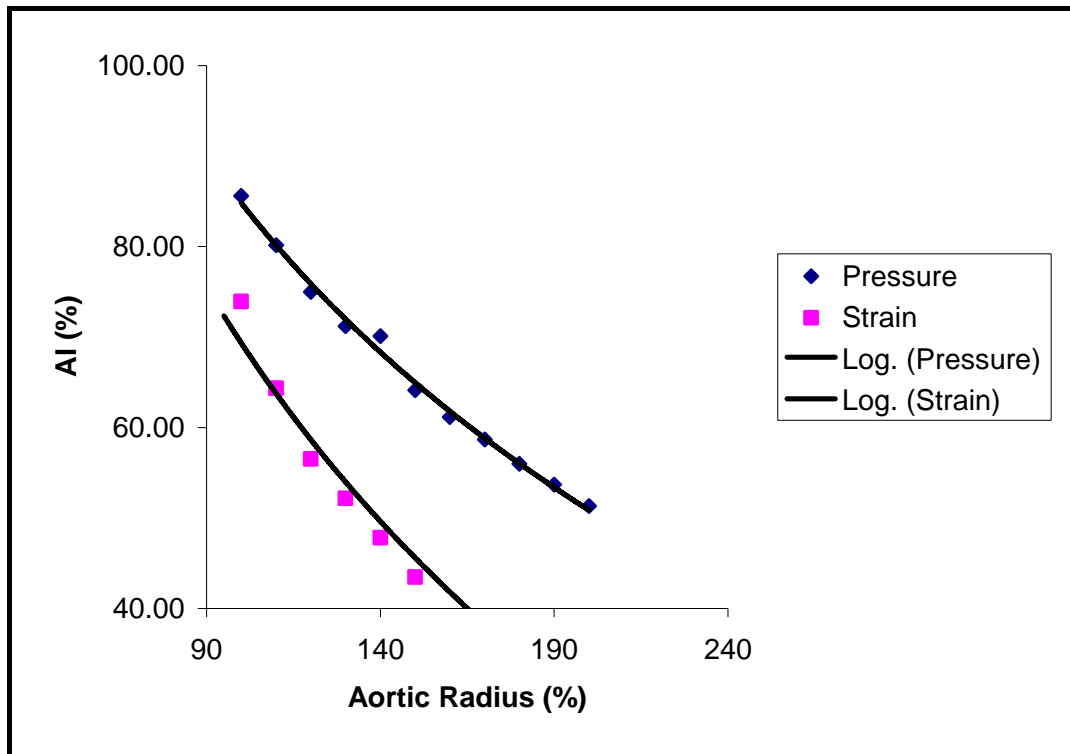


Figure 5.8: The effect of aortic radius variations on the brachial pressure and cuff strain augmentation indices.

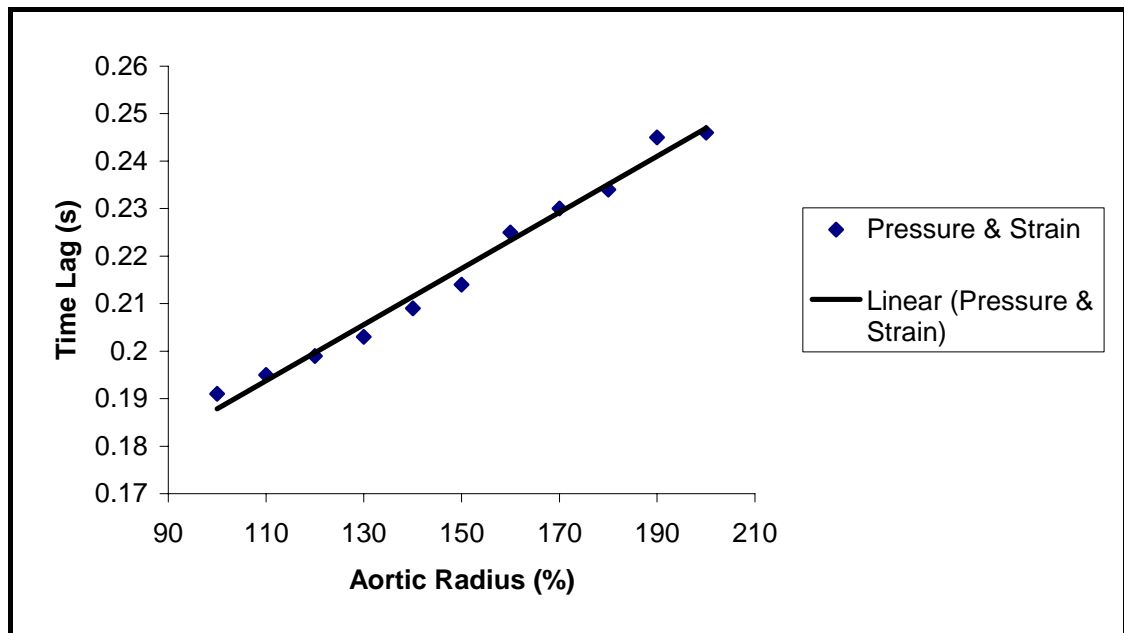


Figure 5.9: The effect of aortic radius variations on the Time Lag of the reflected wave.

The decrease in the propagation velocity caused the reflected wave from the lower body to arrive to the brachial artery later on diastole where less pressure augmentation takes place. This is also shown by the increase in the Time Lag of the reflected wave from as shown in figure 5.9. The difference between the pressure and the cuff strain augmentation indices is also attributed to the different brachial artery compliance at different transmural pressures as explained in Sections 5.2.1 and 5.2.2.

5.2.4 Effect of Aortic Thickness Variations

In-vivo experimental results from Pearson et al [51] confirm that the thickness of the human aorta increases by an average of 100% between the ages of 10 and 80 years old. The relationship between the thickness of the aorta and the brachial artery pressure and cuff strain augmentation indices is plotted in figure 5.10.

The brachial artery pressure AI increased from 85.60 % at normal aortic thickness to 116.19 % at double the thickness. The increase in pressure augmentation is caused by the increase in the propagation velocity of the pressure waveform caused by the increased artery wall thickness which in turn causes the reflected wave from the lower body to return faster to the brachial artery where it augments with the incident wave from the heart.

The decrease in the Time Lag between the upstroke of the incident wave and the arrival of the reflected wave is another indicator of the increase in pressure wave velocity as shown in figure 5.11. The difference in the pressure and strain augmentation indices is also caused by the effect of transmural pressure on the compliance of the brachial artery as explained in the previous sections.

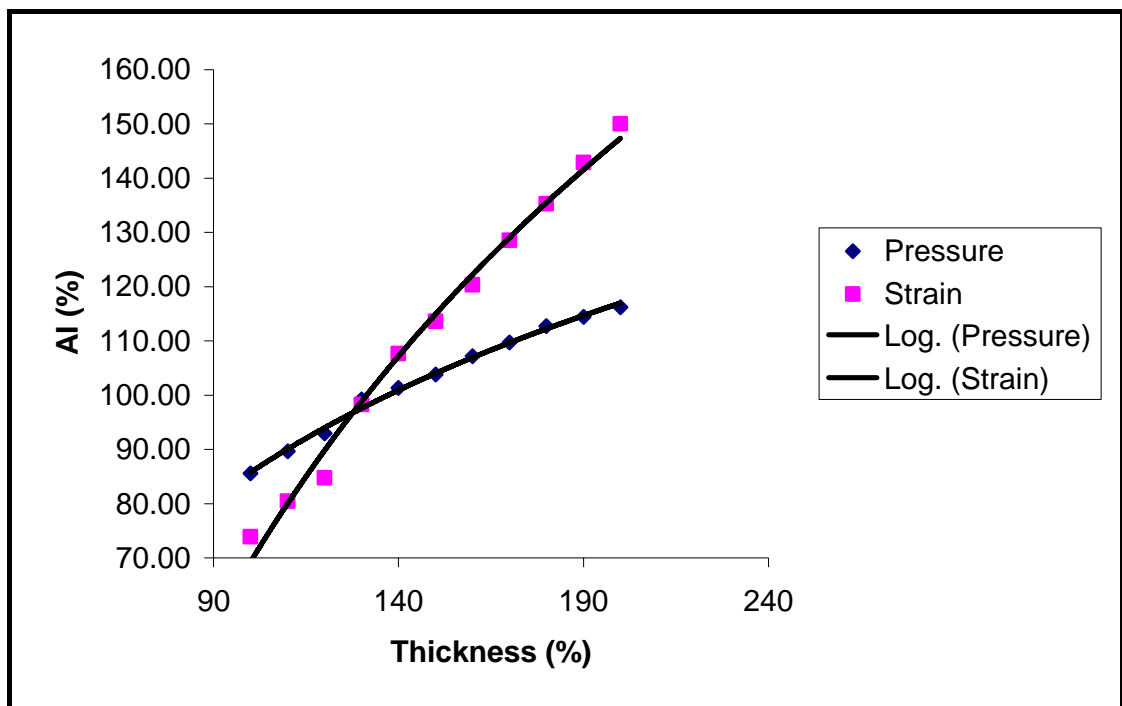


Figure 5.10: The effect of variations in aortic thickness on the brachial artery and the cuff strain augmentation indices.

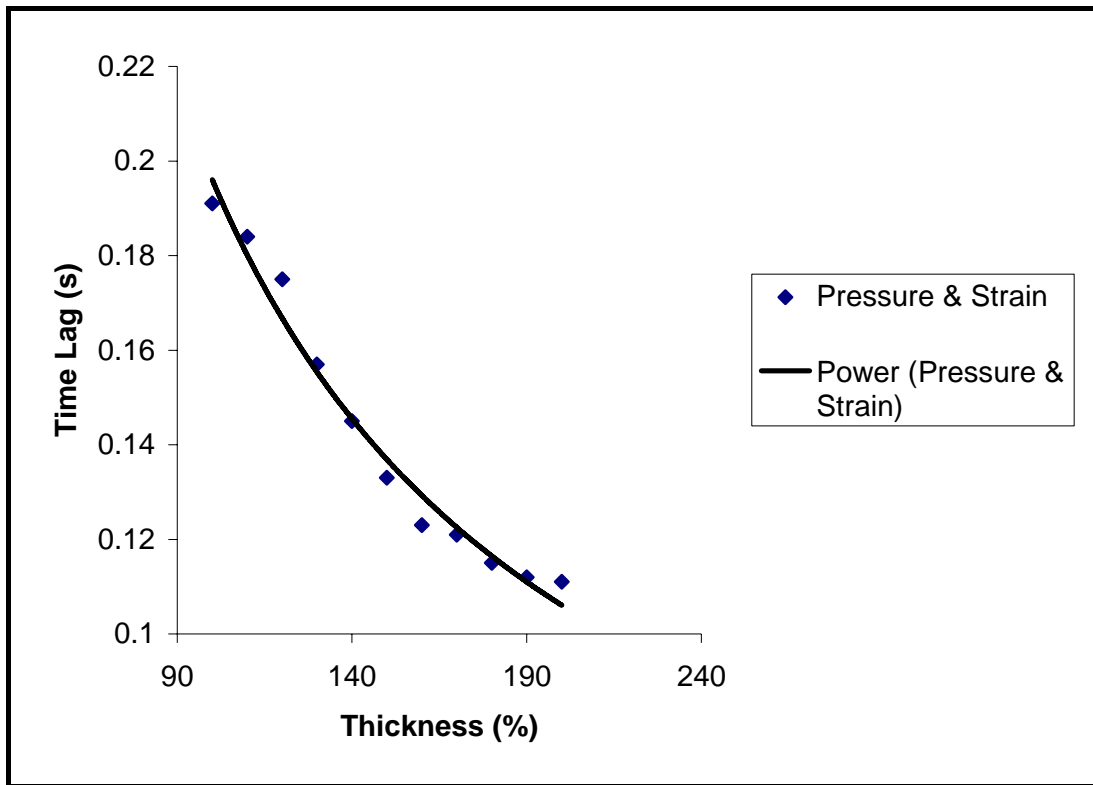


Figure 5.11: The effect of variations in aortic thickness on the Time Lag between the upstroke of the incident wave and the arrival of the reflected wave to the brachial artery.

5.2.5 Effect of Heart Rate

Resting heart rate varies between individuals and usually increases with age and poor physical fitness [52]. The effects of increasing heart rate on the brachial artery pressure and cuff strain augmentation indices are plotted in figure 5.12. The model predicts a decrease in the pressure AI (AI_p) from 85.6% at 75 Hz to 64.96 % at 120 Hz. The cuff strain AI (AI_s) also decreases from 74% at 75 Hz to 44% at 125 Hz. The decrease in pressure augmentation is caused by the decrease in the systolic period. The pressure wave velocity is independent of the heart rate hence the reflected pressure wave still arrives at the brachial artery at the same time which is confirmed by the unchanged Time Lag value. However, the reflected pressure wave now arrives in diastole because of the shortened systolic period and hence less pressure augmentation takes place. This phenomenon is also supported by an increasing number of recent studies [53].

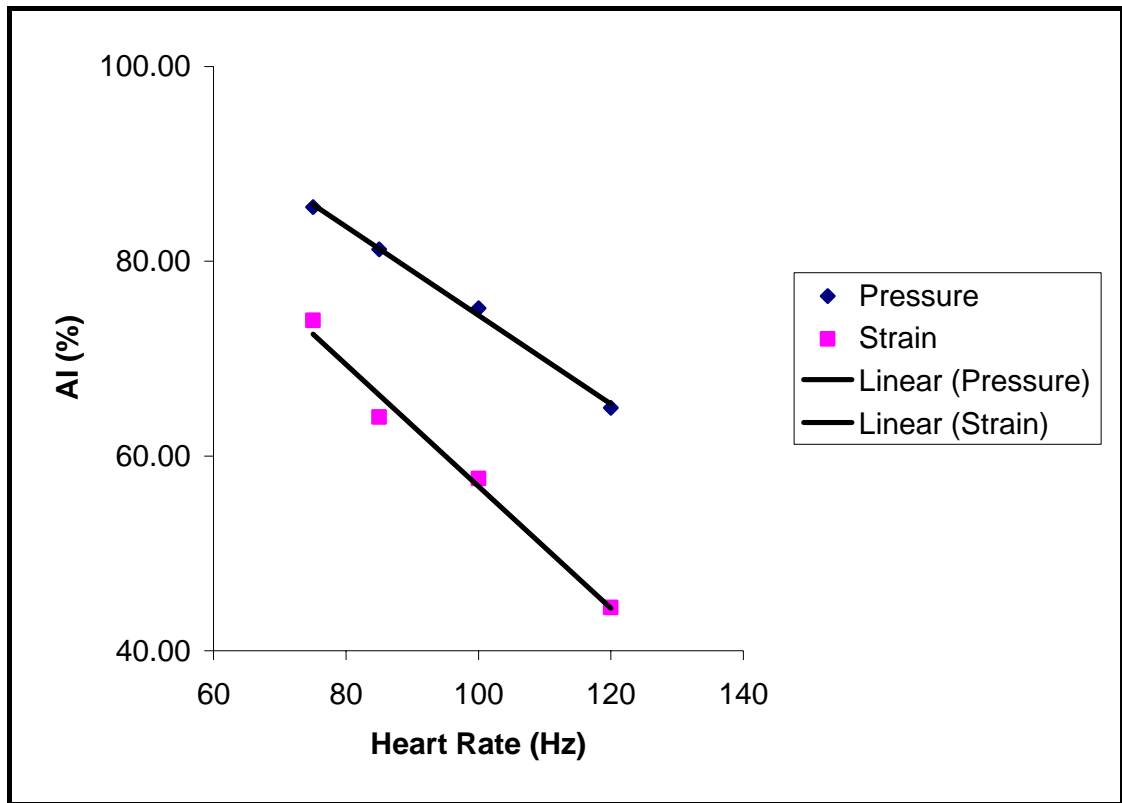


Figure 5.12: The effect of heart rate on the brachial artery pressure and cuff strain augmentation indices.

5.2.6 Effect of Cuff Pressure

It is essential to observe the effect of the value of cuff pressure on the pressure and strain contours and their feature points. The model predicts that pressure and strain augmentation indices will decrease with increasing the cuff pressure as shown in figure 5.13. This decrease is attributed to the increase in the magnitude of the negative reflected wave. As the cuff pressure increases, the cross-sectional area of the brachial artery under the cuff decreases, which in turn increases the impedance mismatch between the section of the brachial artery proximal to the cuff and the section under the cuff. The impedance mismatch increase therefore enlarges the amplitude of the positive wave reflection as discussed in Chapter 3. This reflected wave further negatively reflects at the mouth of the subclavian artery and returns to the brachial artery at a similar time to the positive reflection from the lower body and hence the apparent pressure augmentation is reduced.

Furthermore, the strain AI does not change as much as the pressures AI with increasing cuff pressures. This can be explained by the dependence of the brachial artery compliance on the transmural pressure as explained in section 5.2.1. As the cuff pressure increases, the transmural pressure becomes more negative where the brachial

artery is less compliant and not as dependent on the transmural pressure as it is near zero transmural pressure as shown in figure 5.3. This decreases the variation in the artery response between the first and second pressure peaks as discussed in section 5.2.1.

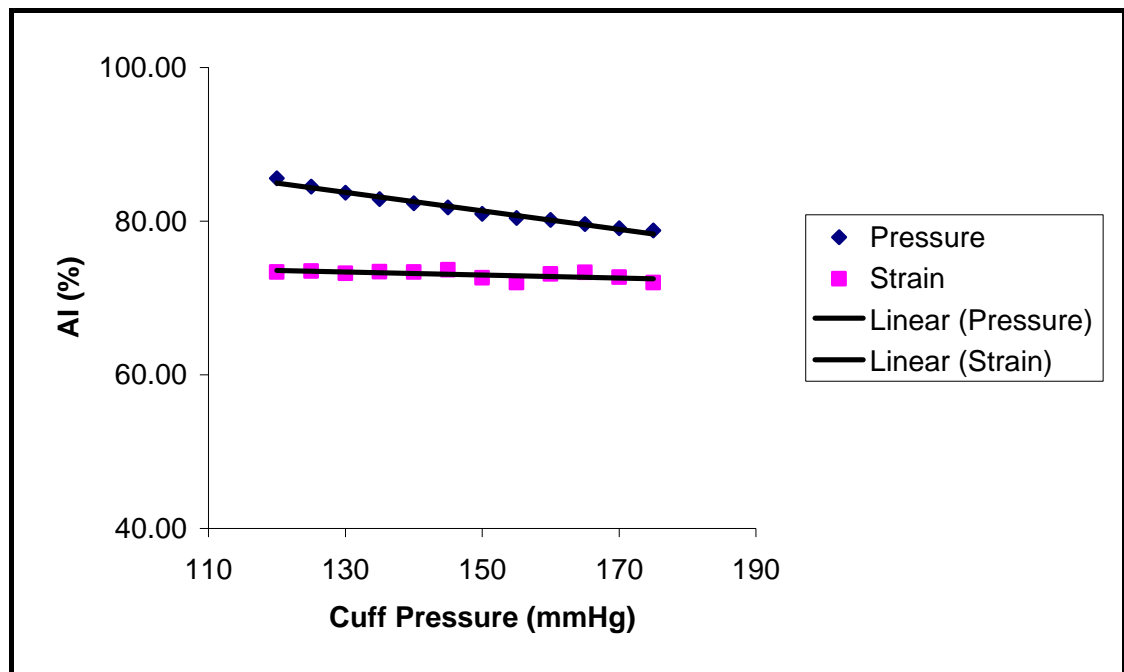


Figure 5.13: The effect of cuff pressure on the brachial artery pressure and the cuff strain augmentation indices.

5.3 General Discussion

The results of the model simulation demonstrated that the model developed in this work is able to simulate the brachial artery pressure and cuff outer wall strain contours. The results also show that the model is able to predict the effect of aortic stiffness, aortic thickness, aortic cross-sectional area, heart rate and cuff pressure on the simulated pressure and strain waveforms.

All model results developed in this work are qualitatively in agreement with published results. Quantitative validation of the model developed in this work is extremely difficult for a number of reasons. This is the first published investigation that looks at the brachial augmentation index and Time Lag as a measure of arterial stiffness. Hence there is no evidence of previous experimental studies that report any model or experimental results that show the effect of any of the above parameters on the brachial pressure and strain contours. Furthermore, conducting an experimental investigation using the Pulsecor WEP monitor to investigate the effect of aortic material and

geometric properties on the measured contours will not produce conclusive results as it is impossible to study only one parameter in the system i.e. there is a large number of factors that affect the propagation and reflection of pressure waves in the system as demonstrated earlier and measuring the contours using the Pulsecor WEP monitor for different subjects would only show the combined effect of an enormous range of factors.

In Pulsecor's WEP monitor, a piezoelectric sensor is fixed circumferentially to the pneumatic cuff outside wall, giving a sensor output proportional to the circumferential strain on the wall. Several readings are taken using this device as part of another study being carried out by Pulsecor Ltd. Some of these readings are used to qualitatively compare the waveforms obtained from this model and readings from the device as shown in figure 5.14. The shape of the strain contours obtained from the device compared very well with the model results. Some of the strain contours showed two pressure peaks while some contours showed increased pressure augmentation. These could be a result of increased aortic stiffness but such a hypothesis can not be verified.

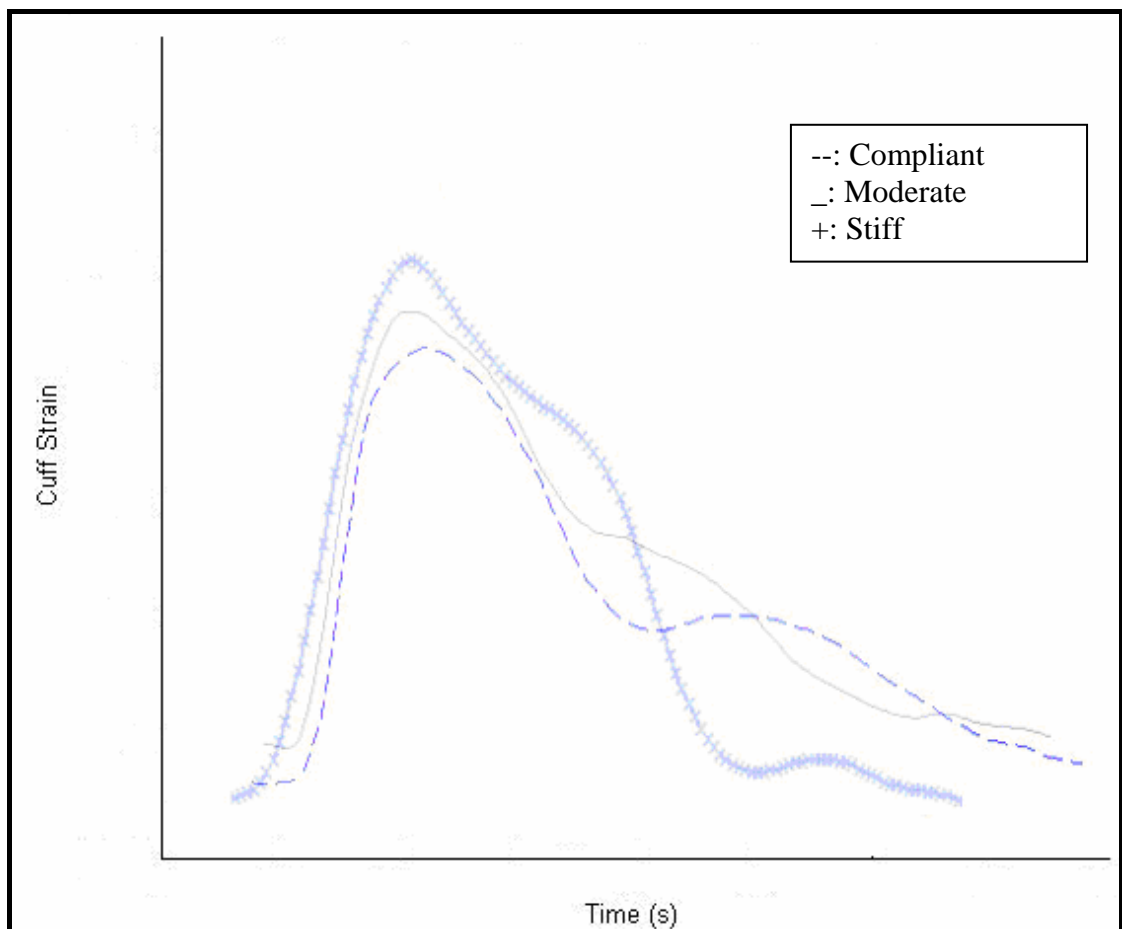


Figure 5.14: Strain contours obtained from the Pulsecor device for three individuals. The legend shows a speculative artery stiffness state.

In both reality and modelling; aortic pulse wave velocity does not depend only on the aortic stiffness but also depends on the radius and thickness of the aorta as shown in the model simulation. However recent in-vivo human studies by Pearson et al [51] confirm that aortic stiffness increases by an average of 300% in humans between the ages of 10 to 80 years with no or little change in the “thickness to radius ratio”. Furthermore, there is much less geometric variation within the same age group when compared to aortic stiffness [51]. Hence from equation 2.9, it can be seen that aortic pulse wave velocity is mainly dependent on aortic stiffness.

In order to validate the model, Aortic PWV is simulated using age dependent aortic stiffness values obtained from Pearson et al [51] as shown in figure 5.15. These simulated PWV curves compared well with in vivo age dependent aortic PWV measurements reported in the literature as shown in figure 5.15 [3, 54]. This proves that the model is able to accurately predict arterial PWV and that aortic stiffness is the major determinant of aortic PWV which can be estimated from the feature points on the strain contours.

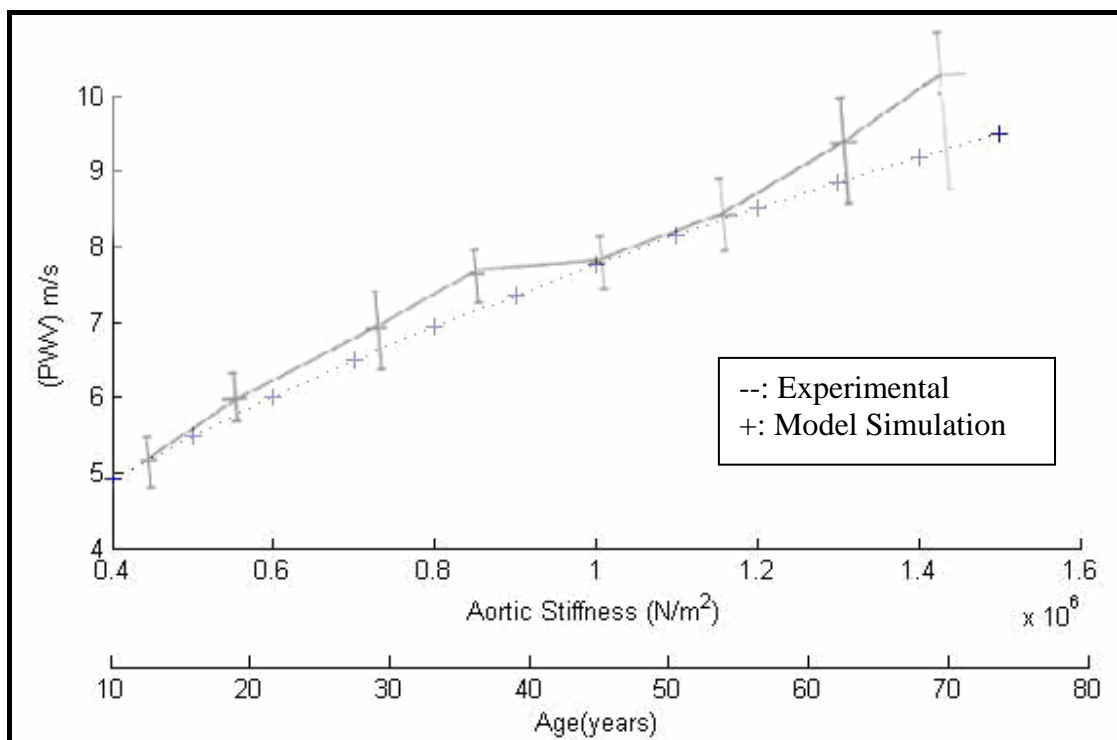


Figure 5.15: A comparison between experimental and model (PWV) vs. Aortic stiffness and patient’s age [3].

The results of the mathematical model also show that heart rate and cuff pressure affect the pressure and the cuff strain augmentation indices. Hence, it is essential to adjust for these two factors when developing any stiffness detection algorithms based on the

augmentation indices. Also from a modelling point of view, it is recommended that the device readings are taken at above systolic cuff pressure. This is to insure the validity of the “no hand reflection” assumption imposed in this model.

The model can be used to develop the stiffness detection algorithm for the Pulsecor WEP monitor to serve two purposes. The device can be used to detect elevated arterial stiffness by using average age and height specific arterial geometry data obtained from the open literature. Otherwise, the exact severity of arterial stiffness can be found by performing an upper body magnetic resonance imaging (MRI) scan on the patient where it can be used to derive the patient’s arterial geometry information required by the model.

The model is also designed in a way that makes it capable of simulating the effect of more parameters such as arm soft tissue and pneumatic cuff material and geometric properties on the contours. This can be done by simply changing the model input parameters in the MATLAB program. This can be very useful in the cuff design process and in investigating the effect of arm soft tissue geometry and material properties on the acquired waveforms. The effect of cuff and soft tissue properties was not simulated in this thesis as it was outside the scope and objectives.

5.4 Conclusions

The main objective of this thesis was to develop and simulate a physiologically based mathematical model of pressure wave propagation and reflection in the human systemic arteries. The aim of the model was to allow for the non-invasive estimation of arterial stiffness using the brachial artery contours. The model developed in this thesis has met the objectives of this work defined in Chapter 1, and has expanded to investigate the effects of a large number of parameters on the acquired waveforms. Specifically, this work has:

1. Developed and simulated a physiologically based mathematical model of the human systemic arteries. The model was able to simulate pressure wave propagation and reflection in the system and adequately reproduce the brachial artery pressure contour.

2. Developed and simulated a Cuff-Soft Tissue- Brachial Artery model that is able to describe the interactions between the three structures and simulate the transmission of brachial artery pressure waves through the arm soft tissue and pneumatic cuff to allow for the estimation of cuff outer wall strain contours from the brachial artery pressure contours.
3. Combined the arterial and the Cuff-Soft Tissue- Brachial Artery models to obtain a complete model that is able to simulate the effect of applying a pneumatic cuff on subjects' arms on the arterial model and is also able to simulate the strain contour on the cuff outer wall.
4. Investigated the effect of elevations in aortic stiffness on the brachial artery pressure contours and pneumatic cuff strain contours. This was done by finding a relationship between aortic stiffness, the brachial pressure and cuff strain augmentation indices and Time Lag.
5. Examined the effect of variations in aortic internal cross-sectional area on the brachial artery pressure contours and pneumatic cuff strain contours.
6. Studied the effect of variations in aortic thickness on the brachial artery pressure contours and pneumatic cuff strain contours.
7. Simulated and analysed the effect of variations in the subject's heart rate on the brachial artery pressure contours and pneumatic cuff strain contours.
8. Investigated the effect of variations in pneumatic cuff pressure on the brachial artery pressure contours and pneumatic cuff strain contours.
9. Preliminarily validated the model by comparing the simulation results with in-vivo experimental results reported in the literature and contours obtained from the Pulsecor device. These validation attempts demonstrated the soundness of using the model to qualitatively assess arterial stiffness and the ability of the model to predict pressure and strain contours.

5.5 Future Work

While this thesis provided a model for the cardiovascular system and demonstrated the feasibility of using the model to detect arterial stiffness, there are many places for improvement. There are a number of areas where the model can be improved, validated and utilised. Future work should include the following:

1. The effect of arterial curvature on pressure wave propagation is still unknown. Hence, the model can be made more realistic by including the effect of curvature of the aorta and the subclavian artery.
2. The use of more realistic assumptions when developing the mathematical model could improve its accuracy but it is important to remember that the more complicated the model is the more computer power is needed. Some of the more important aspects that can be explored are the significance of wave reflections from vascular beds, the effect of arterial external boundary conditions and the effect of arterial wall non-linear viscoelasticity.
3. Use this work to further develop the stiffness detection algorithms to be implemented in the Pulsecor WEP monitor.
4. Further in-vivo validation is extremely crucial to this work but this is not part of the objectives of this thesis. However, preliminary experimental protocols have been designed to further validate the model and will be carried out as part of other work being undertaken by the Biomedical Engineering Centre (BioMEC) at the Auckland University of Technology.

Appendix A MATLAB Program

```
%Acoustic Model-----  
-  
%Clear screen and space variables  
clc  
clear  
  
%initialise variables  
g=1;  
  
% Define the blood density  
roh=1060;  
  
%Ask the user the persons aortic stiffness and the  
E= input('What is the patients stiffness *10^5?')*10^5;  
  
% Ask the user for the desired cuff pressure  
pc=input('What is the cuff pressure?');  
  
%Subclavian + brachial artery Young's Modulus  
E2=4*10^5  
  
% Initialise the thickness of the aorta segments  
h=[0.00180826  
0.001508872  
0.001352578  
0.001250339  
0.00117588  
0.001118095  
0.001071317  
0.001032295  
0.000999  
0.000970088  
0.000944628  
0.000921948  
0.000901551  
0.000883056  
0.000866169  
0.000850658  
0.000836334  
0.000823046  
0.000810666  
0.00079909  
0.000788229  
0.000778008
```

```
0.000768364
0.00056];
```

```
% Initialise the radius of the aorta segments
```

```
r=[0.016785054
0.013319497
0.011582751
0.010476101
0.009685702
0.009081761
0.008599161
0.008201013
0.007864582
0.007574956
0.007321882
0.007098032
0.006898007
0.006717726
0.006554034
0.00640445
0.00626699
0.006140045
0.006022293
0.005912636
0.005810156
0.005714076
0.005623731
0.003100];
```

```
% Ask the user for the percentage of the patients arteries radius compared to healthy
ii=input('What is the Area Percentage?')*0.01;
```

```
% Ask the user for the percentage of the patients arteries thickness compared to healthy
iii=input('What is the Thickness Percentage?')*0.01;
```

```
%Calculate the new Radius
```

```
r=((9+ii)*0.1)*r;
```

```
%Calculate the new thickness
```

```
h=((9+iii)*0.1)*h;
```

```
%calculate the area, wave speed, and impedance at each segment
```

```
for j= 1:24
```

```
Ar(j)=pi*r(j)^2;
```

```
c(j)=sqrt((E(1)*h(j))/(2*roh*r(j)));
```

```
Z(j)=(roh*c(j))/Ar(j);
```

```
end
```

```
%set the length of each segment
```

```

x=0.018;

%calculate the time lag for each segment
t_a=x./c;

%Calculate the time lag for the whole aorta
tt=sum(t_a);
d=(t_a(1)+t_a(2)+t_a(3));

%Initialise brachial artery segment thickness
h_b=[0.000692
0.0006816
0.0006712
0.0006608
0.0006504
0.00064
0.0006296
0.0006192
0.0006088
0.0005984
0.000588
0.0005776
0.0005672
0.0005568
0.0005464
0.000536];

%Initialise brachial artery segment radius
r_b=[0.004298
0.0041654
0.0040328
0.0039002
0.0037676
0.003635
0.0035024
0.0033698
0.0032372
0.0031046
0.002972
0.0028394
0.0027068
0.0025742
0.0024416
0.002309
];

%calculate Area, wave speed and impedance for each element in the brachial
%artery
for j= 1:16
Ar(j)=pi*r_b(j)^2;
c_b(j)=sqrt((E2(1)*h_b(j))/(2*roh*r_b(j)));
Z1(j)=(roh*c(j))/Ar(j);

```



```

c_s=sqrt((E2*h_b(1))/(2*roh*r_b(1)));
Ars=pi*r_b(1)^2;
Zs=(roh*c_s)/Ars;

```

% Calculate the wave reflection at the subclavian/aorta junction.

```
Reff2=(((Za)-(Zs))/((Za)+(Zs)))
```

% Describe heart wave by Fourier Series

% Set a function for one heart period

```

for i=1:66
x(i)=(i-1)/18*0.4;
y(i)=(-3.391234+6*cos(2*pi*(0.8+x(i)))-
2.16*cos(2*pi*2*(0.8+x(i)))+0.335*cos(2*pi*3*(0.8+x(i))))*40/0.8;
    if y(i)<0
        y(i)=0;
    end
end

```

% Initialise variables

```

T=0.8;
N=36;
dt=T/N;
w=(2*pi)/T;
A0=14.7;
j=1;
for i=0:90
    t(j)=i*dt;
    j=j+1;
end

```

% Find the Fourier coefficients

```

j=1;
for n=1:(N/2)
    for i=1:N

        At(i,j)=y(i)*cos(n*w*t(i));
        Bt(i,j)=y(i)*sin(n*w*t(i));
    end
    j=j+1;
end

```

```

A=[zeros((N/2),1)];
B=[zeros((N/2),1)];
for n=1:(N/2)
    for i=1:N
        A(n)= A(n) +At(i,n);
        B(n)= B(n) +Bt(i,n);
    end
end
A=(2*A)/N;

```

```

B=(2*B)/N;

% Calculate the function value for every t we desire
j=1;
for t=0:0.001:8;
    yy=0;
    for i=1:18

        sigma(i)=(sin((i*pi)/18))/((i*pi)/18);
        y_temp(i)=A(i)*sigma(i)*cos(i*w*(t))+B(i)*sigma(i)*sin(i*w*(t));
        yy=yy+y_temp(i);
    end
    yy=yy+A0;
    yyy(j)=yy;
    j=j+1;
end

% Calculate the reflected wave from the iliac
yr=yyy*Ref;

%Calculate The time lags
% Time it take the heart wave to reach the brachial artery
Lag1=(d+tt_b);

%Time it takes the reflection from the subclavian/aortic junction wave to
%reach the brachial artery
Lagneg1=Lag1+2*tt_b;

%Time it takes the reflection from the iliac bifurcation to reach the
%brachial artery
Lag2=(2*tt+tt_b);

%Calculate the waves at the brachial artery.
h=1;

for t=0:0.001:2

    if t<=Lag1
        y_total(h)=0;
        h=h+1;
    elseif t<Lagneg1
        y_total(h)=yyy(1+round((t-Lag1)*1000));
        y_or(h)=yyy(1+round((t-Lag1)*1000));
        h=h+1;
        z=h;
    elseif t<Lag2

```

```

        y_total(h)=yyy(1+round((t-Lag1)*1000))          +(Reff*Reff2)*yyy(1+round((t-
Lagneg1)*1000));
        y_or(h)=yyy(1+round((t-Lag1)*1000));
        y_r(h)=(Reff*Reff2)*yyy(1+round((t-Lagneg1)*1000));

        h=h+1;
    else
        y_total(h)=yyy(1+round((t-Lag1)*1000))          +      (Reff*Reff2)*yyy(1+round((t-
Lagneg1)*1000)) +yr(1+round((t-Lag2)*1000));
        y_or(h)=yyy(1+round((t-Lag1)*1000));
        y_r(h)= (Reff*Reff2)*yyy(1+round((t-Lagneg1)*1000));
        y_oc(h)=yr(1+round((t-Lag2)*1000));
        h=h+1;

    end

end
end

```

%Cuff-Soft Tissue- Brachial Artery Model-----

% Initialise the cuff parameters

```

betae=0.0038;
betai=0.0136;
pe0=1.5832*10^5;
pi0=5.5998;
dpcdt=(pc*1333)/1800;
R0=6.3
R=R0

```

% Initialise Tissue Parameters

```

sig=0;
p0=0;
pb=0;
pc=0;
re10=5.4;
re20=5.4;
re30=5.4;
pe20=0;
ri=1.2;
l10=7;
l20=14;
l30=7;
et0=0.4*10^6;
betat=8;
vt=0.45;
cnt=1;

```

% Initialise the Brachial Artery Parameters

```

pa=80*1333;
ra0=0.23;
a0=0.166;

```

```

n=4*10^3;
h0=0.0575;
ea0=3*10^5;
betaa1=5;
betaa2=21.5;
aa=0.16;
ra=sqrt(aa/pi);
dadt=0;
tt=0.1;
dvdt=0;
raw=1.05;
vis=0.04;
kt=1;

```

```

%CALCULATE THE NEW PARAMETERS AT THE DESIRED CUFF PRESSURE

```

```

%Loop and increase the cuff pressure from 0 to the desired cuff pressure

```

```

for i=1:1800
    for t=1:10

```

```

%Calculate the Coefficients of equations (2.41-2.44)

```

```

et10=et0;
et20=et0+betat*pb;
et30=et0;

```

```

g10=et10/(2*(1+vt));
g20=et20/(2*(1+vt));
g30=et30/(2*(1+vt));

```

```

lamp10=(2*g10*vt)/(1-2*vt);
lamp20=(2*g20*vt)/(1-2*vt);
lamp30=(2*g30*vt)/(1-2*vt);

```

```

d10=(4*g10*lamp10)/(lamp10+2*g10)+2*g10*(1+ri^2/re10^2);
d20=(4*g20*lamp20)/(lamp20+2*g20)+2*g20*(1+ri^2/re20^2);
d30=(4*g30*lamp30)/(lamp30+2*g30)+2*g30*(1+ri^2/re30^2);

```

```

hrp10=(1/d10)*((re10^2-ri^2)/re10);
hrp20=(1/d20)*((re20^2-ri^2)/re20);
hrp30=(1/d30)*((re30^2-ri^2)/re30);

```

```

hrsig10=(lamp10/((lamp10+2*g10)*d10))*((re10^2-ri^2)/re10);
hrsig20=(lamp20/((lamp20+2*g20)*d20))*((re20^2-ri^2)/re20);
hrsig30=(lamp30/((lamp30+2*g30)*d30))*((re30^2-ri^2)/re30);

```

```

hlp10=(2*lamp10*110)/((lamp10+2*g10)*d10);
hlp20=(2*lamp20*120)/((lamp20+2*g20)*d20);
hlp30=(2*lamp30*130)/((lamp30+2*g30)*d30);

```

```

hlsig10=110/(lamp10+2*g10)+(2*110*lamp10^2)/(d10*(lamp10+2*g10)^2);

```

```

hlsig20=l20/(lamp20+2*g20)+(2*l20*lamp20^2)/(d20*(lamp20+2*g20)^2);
hlsig30=l30/(lamp30+2*g30)+(2*l30*lamp30^2)/(d30*(lamp30+2*g30)^2);

```

```

hpp10=2*g10*(3*lamp10+2*g10)/((lamp10+2*g10)*d10);
hpp20=2*g20*(3*lamp20+2*g20)/((lamp20+2*g20)*d20);
hpp30=2*g30*(3*lamp30+2*g30)/((lamp30+2*g30)*d30);

```

```

hpsig10=-
lamp10/(lamp10+2*g10)+(2*g10*(3*lamp10+2*g10)*lamp10)/((lamp10+2*g10)^2*d10);
hpsig20=-
lamp20/(lamp20+2*g20)+(2*g20*(3*lamp20+2*g20)*lamp20)/((lamp20+2*g20)^2*d20);
hpsig30=-
lamp30/(lamp30+2*g30)+(2*g30*(3*lamp30+2*g30)*lamp30)/((lamp30+2*g30)^2*d30);

```

```

hrv10=-(1/(2*pi*re10^2*d10))*(2*g10*((re10^2-ri^2)/re10)+d10*re10);
hrv20=-(1/(2*pi*re20^2*d20))*(2*g20*((re20^2-ri^2)/re20)+d20*re20);
hrv30=-(1/(2*pi*re30^2*d30))*(2*g30*((re30^2-ri^2)/re30)+d30*re30);

```

```

hlv10=-(2*lamp10*g10*110)/((lamp10+2*g10)*pi*re10^2*d10);
hlv20=-(2*lamp20*g20*120)/((lamp20+2*g20)*pi*re20^2*d20);
hlv30=-(2*lamp30*g30*130)/((lamp30+2*g30)*pi*re30^2*d30);

```

```

hvp10=-(2*g10*(3*lamp10+2*g10))/((lamp10+2*g10)*pi*(re10^2)*d10);
hvp20=-(2*g20*(3*lamp20+2*g20))/((lamp20+2*g20)*pi*re20^2*d20);
hvp30=-(2*g30*(3*lamp30+2*g30))/((lamp30+2*g30)*pi*re30^2*d30);

```

%Calculate the Coefficients of equations (2.56)

```

dd=1/(betai*(pc-pb+pi0))+2*pi*re20*120*(hrp20-
((hrsig20*hlp20/(hlsig10+hlsig20+hlsig30))));
hbcv=-((2*pi*re20*120)/dd)*(hrv20-(hlv20*hrsig20)/(hlsig10+hlsig20+hlsig30));

```

```

hbc=1/(dd*betai*(pc-pb+pi0));

```

%Calculate the brachial artery volume change dv/dt if the pressure is more than diastolic.

```

kp=(h0*ea0)/(3*ra0);

```

```

dadt=(2*(pa-pe20)*a0*ra0)/(n*h0) - ((2*kp*a0*ra0)/(n*h0))*(1-(aa/a0)^(-3/2));

```

```

if dadt>0
    dadt=0;
end

```

```

aa=aa+dadt*tt;

```

```

aastr(cnt)=aa;
dvbdt=dadt;

dvdt=0;
g=1;

% Solve for equations (2.41-2.60)
dpbdt=hbc*dpcdt+hbv*dvdt;
dRdt=(1/(2*pi*14*R*betae*(pc+pe0)))*dpcdt;
dsigdt=(-hlp20*dpbdt)/(hlsig10+hlsig20+hlsig30);
dredt10=-hrsig10*dsigdt;
dredt20=-hrp20*dpbdt-hrv20*dvdt-hrsig20*dsigdt;
dredt30=-hrsig30*dsigdt;
dldt10=hlsig10*dsigdt;
dldt20=hlp20*dpbdt+hlv20*dvdt+hlsig20*dsigdt;
dldt30=hlsig30*dsigdt;
dpedt10=hpsig10*dsigdt;
dpedt20=hpp20*dpbdt+hpv20*dvdt+hpsig20*dsigdt;
dpedt30=hpsig30*dsigdt;

% Store the required output variables in separate arrays.
sig=sig+dsigdt*tt;
sigstr(cnt)=sig;

re10=re10+dredt10*tt;
re10str(cnt)=re10;

re20=re20+dredt20*tt;
re20str(cnt)=re20;

re30=re30+dredt30*tt;
re30str(cnt)=re30;

l10=l10+dldt10*tt;
l10str(cnt)=l10;

l20=l20+dldt20*tt;
l20str(cnt)=l20;

l30=l30+dldt30*tt;
l30str(cnt)=l30;

pe20=pe20+dpedt20*tt;
pe20str(cnt)=pe20/1333.33;

pb=pb+dpbdt*tt;
pbstr(cnt)=pb/1333.33;

R=R+dRdt*tt;
Rstr(cnt)=R;
dR(cnt)=(R-R0)/R0;

```

```

end

pc=pc+dpcdt;
pcstr(cnt)=pc/1333.33;
cnt=cnt+1;
end

%FEED IN THE BRACHIAL ARTERY PRESSURE
dpcdt=0

%Set the value for the brachial artery pressure
pa=y_total

%Add the diastolic pressure
pa=pa*1333+80*1333

%Set the time interval for the iteration
tt=0.001

%loop over the pressure data points
for i=1:2000

%Loop over the time iteration
    for t=1:100

%Calculate the Coefficients of equations (2.41-2.44)
et10=et0;
et20=et0+betat*pb;
et30=et0;

g10=et10/(2*(1+vt));
g20=et20/(2*(1+vt));
g30=et30/(2*(1+vt));

lamp10=(2*g10*vt)/(1-2*vt);
lamp20=(2*g20*vt)/(1-2*vt);
lamp30=(2*g30*vt)/(1-2*vt);

d10=(4*g10*lamp10)/(lamp10+2*g10)+2*g10*(1+ri^2/re10^2);
d20=(4*g20*lamp20)/(lamp20+2*g20)+2*g20*(1+ri^2/re20^2);
d30=(4*g30*lamp30)/(lamp30+2*g30)+2*g30*(1+ri^2/re30^2);

hrp10=(1/d10)*((re10^2-ri^2)/re10);
hrp20=(1/d20)*((re20^2-ri^2)/re20);
hrp30=(1/d30)*((re30^2-ri^2)/re30);

hrsig10=(lamp10/((lamp10+2*g10)*d10))*((re10^2-ri^2)/re10);
hrsig20=(lamp20/((lamp20+2*g20)*d20))*((re20^2-ri^2)/re20);
hrsig30=(lamp30/((lamp30+2*g30)*d30))*((re30^2-ri^2)/re30);

hlp10=(2*lamp10*110)/((lamp10+2*g10)*d10);
hlp20=(2*lamp20*120)/((lamp20+2*g20)*d20);

```

$$hlp30=(2*\text{lamp}30*130)/((\text{lamp}30+2*g30)*d30);$$

$$hlsig10=110/(\text{lamp}10+2*g10)+(2*110*\text{lamp}10^2)/(d10*(\text{lamp}10+2*g10)^2);$$

$$hlsig20=120/(\text{lamp}20+2*g20)+(2*120*\text{lamp}20^2)/(d20*(\text{lamp}20+2*g20)^2);$$

$$hlsig30=130/(\text{lamp}30+2*g30)+(2*130*\text{lamp}30^2)/(d30*(\text{lamp}30+2*g30)^2);$$

$$hpp10=2*g10*(3*\text{lamp}10+2*g10)/((\text{lamp}10+2*g10)*d10);$$

$$hpp20=2*g20*(3*\text{lamp}20+2*g20)/((\text{lamp}20+2*g20)*d20);$$

$$hpp30=2*g30*(3*\text{lamp}30+2*g30)/((\text{lamp}30+2*g30)*d30);$$

$$hpsig10=-$$

$$\text{lamp}10/(\text{lamp}10+2*g10)+(2*g10*(3*\text{lamp}10+2*g10)*\text{lamp}10)/((\text{lamp}10+2*g10)^2*d10);$$

$$hpsig20=-$$

$$\text{lamp}20/(\text{lamp}20+2*g20)+(2*g20*(3*\text{lamp}20+2*g20)*\text{lamp}20)/((\text{lamp}20+2*g20)^2*d20);$$

$$hpsig30=-$$

$$\text{lamp}30/(\text{lamp}30+2*g30)+(2*g30*(3*\text{lamp}30+2*g30)*\text{lamp}30)/((\text{lamp}30+2*g30)^2*d30);$$

$$hrv10=-(1/(2*\text{pi}*re10^2*d10))*(2*g10*((re10^2-ri^2)/re10)+d10*re10);$$

$$hrv20=-(1/(2*\text{pi}*re20^2*d20))*(2*g20*((re20^2-ri^2)/re20)+d20*re20);$$

$$hrv30=-(1/(2*\text{pi}*re30^2*d30))*(2*g30*((re30^2-ri^2)/re30)+d30*re30);$$

$$hlv10=-(2*\text{lamp}10*g10*110)/((\text{lamp}10+2*g10)*\text{pi}*re10^2*d10);$$

$$hlv20=-(2*\text{lamp}20*g20*120)/((\text{lamp}20+2*g20)*\text{pi}*re20^2*d20);$$

$$hlv30=-(2*\text{lamp}30*g30*130)/((\text{lamp}30+2*g30)*\text{pi}*re30^2*d30);$$

$$hvp10=-(2*g10*(3*\text{lamp}10+2*g10))/((\text{lamp}10+2*g10)*\text{pi}*(re10^2)*d10);$$

$$hvp20=-(2*g20*(3*\text{lamp}20+2*g20))/((\text{lamp}20+2*g20)*\text{pi}*re20^2*d20);$$

$$hvp30=-(2*g30*(3*\text{lamp}30+2*g30))/((\text{lamp}30+2*g30)*\text{pi}*re30^2*d30);$$

%Calculate the Coefficients of equations (2.56)

$$dd=1/(\text{betai}*(\text{pc}-\text{pb}+\text{pi}0))+2*\text{pi}*re20*120*(\text{hrp}20-((\text{hrs}ig20*\text{hlp}20)/(\text{hls}ig10+\text{hls}ig20+\text{hls}ig30))));$$

$$\text{hbv}=(2*\text{pi}*re20*120)/dd*(\text{hrv}20-(\text{hlv}20*\text{hrs}ig20)/(\text{hls}ig10+\text{hls}ig20+\text{hls}ig30));$$

$$\text{hbc}=1/(dd*\text{betai}*(\text{pc}-\text{pb}+\text{pi}0));$$

%Calculate the Coefficients of equations (2.54)

$$d2=1/(\text{betae}*(\text{pc}+\text{pe}0))+1-\text{hbc}/(\text{betai}*(\text{pc}-\text{pb}+\text{pi}0));$$

$$\text{hcv}=-\text{hbv}/(d2*\text{betai}*(\text{pc}-\text{pb}+\text{pi}0));$$

%Calculate the brachial artery volume change dv/dt if the brachial artery

% area is less than the area at zero transmural pressure

if aa>a0

$$\text{eps}=(\text{sqrt}(\text{aa})-\text{sqrt}(\text{a0}))/\text{sqrt}(\text{a0});$$

$$\text{sige}=(\text{ea}0/(\text{betaa}1))*(\exp(\text{betaa}1*\text{eps})+\exp(\text{betaa}2*\text{eps}^2)-2);$$

$$\text{h}=\text{sqrt}(\text{aa}/\text{pi})+\text{sqrt}(\text{aa}/\text{pi}+2*\text{ra}0*\text{h}0+\text{h}0^2);$$

```

dadt=((2*(pa(i)-pe20)*aa*ra0)/(n*h))-((2*ra0*sqrt(pi*aa)*sige)/n);
aa=aa+dadt*tt;
aastr(cnt)=aa;
pustr(cnt)=pa(i)/1333;
dvdt=dadt;

%Calculate the brachial artery volume change dv/dt if the brachial artery
%area is less than the area at zero transmural pressure
else

kp=(h0*ea0)/(3*ra0);
dadt=(2*(pa(i)-pe20)*a0*ra0)/(n*h0) - ((2*kp*a0*ra0)/(n*h0))*(1-(aa/a0)^(-3/2));
aa=aa+dadt*tt;
aastr(cnt)=aa;
pustr(cnt)=pa(i)/1333;
dvdt=dadt;
end

%Solve for equations (2.41-2.60)
dpbdt=hbc*dpcdt+hbv*dvdt;
dpcdt=hcv*dvdt;
dRdt=(1/(2*pi*14*R*betae*(pc+pe0)))*dpcdt;
dsigdt=(-hlp20*dpbdt)/(hlsig10+hlsig20+hlsig30);
dredt10=-hrsig10*dsigdt;
dredt20=-hrp20*dpbdt-hrv20*dvdt-hrsig20*dsigdt;
dredt30=-hrsig30*dsigdt;
dlldt10=hlsig10*dsigdt;
dlldt20=hlp20*dpbdt+hlv20*dvdt+hlsig20*dsigdt;
dlldt30=hlsig30*dsigdt;
dpedt10=hpsig10*dsigdt;
dpedt20=hpp20*dpbdt+hpv20*dvdt+hpsig20*dsigdt;
dpedt30=hpsig30*dsigdt;

% Store the required output variables in separate arrays.
sig=sig+dsigdt*tt;
sigstr(cnt)=sig;

re10=re10+dredt10*tt;
re10str(cnt)=re10;

re20=re20+dredt20*tt;
re20str(cnt)=re20;

re30=re30+dredt30*tt;
re30str(cnt)=re30;

l10=l10+dlldt10*tt;
l10str(cnt)=l10;

l20=l20+dlldt20*tt;
l20str(cnt)=l20;

```

```
l30=l30+dldt30*tt;  
l30str(cnt)=l30;
```

```
pe20=pe20+dpedt20*tt;  
pe20str(cnt)=pe20/1333.33;
```

```
pb=pb+dpbdt*tt;  
pbstr(cnt)=pb/1333.33;
```

```
pc=pc+dpcdt*tt;  
pcstr(cnt)=pc/1333.33;
```

```
R=R+dRdt*tt;  
Rstr(cnt)=R;  
dR(cnt)=(R-R0)/R0;
```

```
end
```

```
pcstr(cnt)=pc/1333.33;  
cnt=cnt+1;  
end
```

```
%Plot the required output
```

```
pa=pa/1333.33;  
x=0:0.001:2;  
xx=0:0.001:0.8;
```

```
%Plot the soft tissue longitudinal tension
```

```
figure(1)  
plot(xx,sigstr),xlabel('Time (s)'), ylabel('Longitudinal Tension')
```

```
%Plot the soft tissue segment radius
```

```
figure(2)  
subplot(3,1,1) ,plot(xx,re10str),xlabel('Time (s)'), ylabel('radius of segment 1')
```

```
subplot(3,1,2) ,plot(xx,re20str),xlabel('Time (s)'), ylabel('radius of segment 2')  
subplot(3,1,3) ,plot(xx,re30str),xlabel('Time (s)'), ylabel('radius of segment 3')
```

```
%Plot the soft tissue segment length
```

```
figure(3)  
subplot(3,1,1) ,plot(xx,l10str),xlabel('Time (s)'), ylabel('length of segment 1')  
subplot(3,1,2) ,plot(xx,l20str),xlabel('Time (s)'), ylabel('length of segment 2')  
subplot(3,1,3) ,plot(xx,l30str),xlabel('Time (s)'), ylabel('length of segment 3')
```

```
%Plot the extravascular pressure
```

```
figure (4)  
plot(pe20str),xlabel('Time (s)'), ylabel('Extravascular Pressure mmHg')
```

```
%Plot the pressure on segment two outside surface
```

```
figure(5)
```

```
plot(xx,pbstr),xlabel('Time (s)', ylabel('Pressure on the outside surface of the arm (mmHg)')
```

```
%Plot the artery area
```

```
figure(6)
```

```
plot(aastr),xlabel('Time (s)', ylabel('Brachial Artery Area (cm^2) ')
```

```
%Plot the cuff pressure
```

```
figure(7)
```

```
plot(xx,pcstr),xlabel('Time (s)', ylabel('cuff pressure (mmHg) ')
```

```
%Plot the brachial artery pressure
```

```
figure(1)
```

```
plot(xx,pa(800:1600)),xlabel('Time (s)', ylabel('Brachial Artery Pressure (mmHg) ')
```

```
%Plot the soft tissue segment two radius
```

```
figure(10)
```

```
plot(x,Rstr(1800:3800)),xlabel('Time (s)', ylabel('Cuff Radius ')
```

```
%Plot the cuff outer wall strain
```

```
figure(2)
```

```
plot(xx,dR(2600:3400)),xlabel('Time (s)', ylabel('Cuff Strain ')
```

References

1. NZ Guidelines Group, 2003, Assessment and Management of Cardiovascular Risk.
2. 2004 Chartbook on cardiovascular, lung and blood disease, 2004, National Heart, Lung and Blood Institute, USA.
3. Nichols, W.W and O'Rourke, M.F, 1998, McDonald's Blood Flow in Arteries; Theoretical, Experimental and Clinical Principles, Fourth edition, Arnold.
4. Dewood, M.a, Spores, J., Notske, R. et al, 1980, Prevalence of total coronary occlusion during the early hours of transmural myocardial infarction, New England journal of medicine, 303 (16), 897-902.
5. Martin, P., 1978: On abdominal aortic aneurysms, Journal of Cardiovascular Surgery, 19, 597-8.
6. Liu, H., Fukasaku, K., Lwase, H., et al, 2003, Influences of Non-planarity, bifurcation, dynamics, inflow and outflows on blood flow patterns in the aortic arch: A multi-scale computational study. In: Summer Bioengineering Conference. Sonesta Beach Resort in Key Biscayne, Florida, United States.
7. Atherosclerosis, February 27, 2007, Wikipedia the Free Encyclopaedia, retrieved February 27, 2007, <http://en.wikipedia.org/wiki/Atherosclerosis>.
8. TORTORA, G.J. and GRABOWSKI, S.R, 1999, Principles of Anatomy and Physiology, 9th Ed., John Wiley & Sons Canada.
9. Laurent, S., Caviezel, B., Beck, L., et al, 1994, Carotid artery distensibility and distending pressure in hypertensive humans, Hypertension, 23:878–883.
10. Pannier, B., Avolio, AP., Hoeks, A., et al, 2002, Methods and devices for measuring arterial compliance in humans, American Journal of Hypertension, 15:743–753.
11. Verbeke, F., Segers, P., Heireman, S., et al, 2005 Noninvasive assessment of local pulse pressure, Importance of brachial-to-radial pressure amplification. Hypertension, 46:244–248.

12. Latham, RD., Westerhof, N., Sipkema, P., et al, 1985 Regional wave travel and reflections along the human aorta: a study with six simultaneous micromanometric pressures, *Circulation*, 72:1257–1269.
13. Laurent, S., Hayoz, D., Trazzi, S., et al, 1993, Isobaric compliance of the radial artery is increased in patients with essential hypertension. *Journal of Hypertension*, 11:89–98.
14. Blacher, J., Guerin, AP., Pannier, B., et al, 1999, Impact of aortic stiffness on survival in end-stage renal disease. *Circulation*, 99:2434–2439.
15. Willum-Hansen, T., Staessen, JA., Torp-Pedersen, C., et al, 2006, Prognostic value of aortic pulse wave velocity as index of arterial stiffness in the general population. *Circulation*, 113:664–670.
16. Van Bortel, LM., Duprez, D., Starmans-Kool, MJ., et al, 2002, Applications of arterial stiffness, Task Force III: recommendations for user procedures. *American Journal of Hypertension*, 15:445–452.
17. Mackenzie, IS., Wilkinson, IB., Cockcroft, JR., 2002, Assessment of arterial stiffness in clinical practice, *QJM*, 95:67–74.
18. O'Rourke, MF., 1982, *Arterial Function in Health and Disease*. Edinburgh: Churchill.
19. London, G., Guerin, A., Pannier, B., et al, 1992, Increased systolic pressure in chronic uremia, Role of arterial wave reflections, *Hypertension*, 2:10–19.
20. Nichols, W., 2005, Clinical Measurement of Arterial Stiffness obtained from non-invasive pressure waveforms, *American Journal of Hypertension*, 18:S3-S10.
21. Chen, C-H., Nevo, E., Fetics, B., et al, 1997, A. Estimation of central aortic pressure waveform by mathematical transformation of radial tonometry pressure: validation of generalized transfer function, *Circulation*, 95:1827–1836.
22. Pauca, AL., O'Rourke, MF., Kon, ND., 2001, Prospective evaluation of a method for estimating ascending aortic pressure from the radial artery pressure waveform, *Hypertension*, 38:932–937.
23. Takazawa, K., Tanaka, N., Fujita, M., et al, 1998, Assessment of vasoactive agents and vascular ageing by the second derivative of photoplethysmogram waveform, *Hypertension*, 32:365–370.
24. Chowienczyk, PJ., Kelly, RP., MacCallum, H., et al, 1999, Photoplethysmographic assessment of pulse wave reflection: blunted response to

- endothelium-dependent beta2-adrenergic vasodilation in type II diabetes mellitus, *Journal of the American College of Cardiology*, 34:2007–2014.
25. Pontrelli, G., Rossoni, E., Numeric Modelling of the Pressure Wave Propagation in the Arterial Flow, 2003, *International Journal for Numerical Methods in Fluids*, 43:651-671.
 26. Stergiopoulos, N., Westerhof, BE., Westerhof, N., 1999, Total arterial inertance as the fourth element of the Windkessel model, *American Journal of Physiology*, 276:81-88.
 27. Olfusen, M., Nadim, A., 2004, On deriving lumped models for blood flow and pressure in the systemic arteries, *Mathematical Biosciences and Engineering*, 1:61-80.
 28. Formaggia, L., Lamponi, D., Quarteroni, A., 2003, One dimensional models for blood flow in arteries, *Journal of Engineering Mathematics*, 47:251-276.
 29. Olfusen, M., 1999, Structured tree outflow condition for blood flow in larger systemic arteries, *American Journal of Physiology*, 276:H257-H268.
 30. Steele, N., Taylor, C., 2003, Simulation of blood flow in the abdominal aorta at rest and during exercise using a 1-d finite element method with impedance boundary conditions derived from a fractal tree, In: *Summer Bioengineering Conference*, sonesta Beach Resort in Key Biscayne, Florida, United States.
 31. Tang, D., Yang, C., Huang, Y., 1999, Wall stress and strain analysis using a three-dimensional thick-wall model with fluid-structure interactions for blood flow in carotid arteries with stenoses, *Computers and Structures*, 72:341-356.
 32. O'Rourke, MF., 1982, Vascular impedance in studies of arterial and cardiac function, *Physiological Reviews*, 62:570-623.
 33. Hamilton, W., Dow, p., 1939, An experimental study of the standing waves in the pulse propagated through the aorta, *American Journal of Physiology*, 125:48-59.
 34. Alexander, R., 1952, The genesis of the aortic standing waves, *Circulation Research*, 1:145-51.
 35. Remington, J., 1963, The physiology of the aorta and the major arteries, *American Physiological Society Handbook of Physiology*, American Physiology Society, 799-838.
 36. Mauck, GW., Smith, CR., Geddes, LA., et al, 1980, The meaning of the point of maximum oscillations in cuff pressure in the indirect measurement of blood pressure: Part 11, *ASME Journal of Biomechanical. Engineering*, 102:28-33.

37. Forster, FK., Turney, D., 1986, Oscillometric determination of diastolic, mean, and systolic blood pressure. A numerical model, *ASME Journal of Biomechanical Engineering*, 108:359-364.
38. Drzewiecki, G., Bansal, V., Karam, E., et al, 1993, Mechanics of the occlusive arm cuff and its application as a volume sensor, *IEEE Trans. Biomed. Eng.*, 40:704-708.
39. Ursino, M., Cristalli, C., 1995, Mathematical modeling of noninvasive blood pressure estimation techniques – part I- Pressure transmission across the arm tissue, *ASME Journal of Biomechanical Engineering*, 117:107-116.
40. Ursino, M., Cristalli, C., 1995, Mathematical modeling of noninvasive blood pressure estimation techniques – part II- Brachial Hemodynamics, *ASME Journal of Biomechanical Engineering*, 117:117-126.
41. Ursino, M., Cristalli, C., 1996, A Mathematical Study of Some Biomechanical Factors Affecting the Oscillometric Blood Pressure Measurement, *IEEE Transactions on Biomedical Engineering*, 43:761-78.
42. Taylor, M., 1959, The influence of the anomalous viscosity of blood upon its oscillatory flow, *Physics of Medicine and Biology*, 3:273-90.
43. Fung, Y.C., 1997, *Biomechanics circulation*, Second edition, Springer. 3:108-205.
44. Chang, C., Atabek, H., 1961, The inlet length for oscillatory flow and its effects on the determination of the rate of flow in the arteries, *Physics of Medicine and Biology*, 6: 303-17.
45. Learoyd, B. M., Taylor, M.G., 1966, Alterations with age in the viscoelastic properties of human arterial walls, *Circ. Res*, 18:278-292.
46. Westerhof, N., Bosman, F., De Vries CJ., et al , 1969, Analog studies of human systemic arterial tree, *Journal of biomechanics*, 2:121-143.
47. Remington, J., 1965, Quantitative synthesis of head and foreleg arterial pulsed in the dog. *American Journal of Physiology*, 208:968-83.
48. Westerhof, B., Guelen, I., Stok, W., et al, 2006, Arterial pressure transfer characteristics: effects of travel time, *American Journal of Physiology- Heart Circulation Physiology*, 292: 800-807.
49. Linden, R., Drzewiecki, G., 2000, Noninvasive Measurement of Brachial Artery Compliance Variability, *Bioengineering Conference Proceedings of the IEEE 26th Annual Northeast 8-9 April 2000*, 39 – 40.

50. Bank, A., Kaiser, D., Rajala, S., et al, 1999, In Vivo Human Brachial Artery Elastic Mechanics: Effects of Smooth Muscle Relaxation, *Circulation*, 100:41-47.
51. Pearson, A., Guo, R., Orsinellid, A., et al, 1994, Transesophageal echocardiographic assessment of the effects of age, gender, and hypertension on thoracic aortic wall size, thickness, and stiffness, *American Heart Journal*, 128:344-51.
52. Nishime, E., Cole, C., Blackstone, E., et al, 2000, "Heart Rate Recovery and Treadmill Exercise Score as Predictors of Mortality in Patients Referred for Exercise ECG", *JAMA*, 284:1392-1398.
53. Wilkinson, IB., MacCallum, H., Flint, L., et al, 2000, The influence of heart rate on augmentation index and central arterial pressure in humans, *The Journal of Physiology*, 525:263-270.
54. Ho, K., 1982, Effects of aging on arterial distensibility and left ventricular load in an Australian population, Thesis, University of New South Wales, Australia.